



저작자표시-비영리-변경금지 2.0 대한민국

이용자는 아래의 조건을 따르는 경우에 한하여 자유롭게

- 이 저작물을 복제, 배포, 전송, 전시, 공연 및 방송할 수 있습니다.

다음과 같은 조건을 따라야 합니다:



저작자표시. 귀하는 원저작자를 표시하여야 합니다.



비영리. 귀하는 이 저작물을 영리 목적으로 이용할 수 없습니다.



변경금지. 귀하는 이 저작물을 개작, 변형 또는 가공할 수 없습니다.

- 귀하는, 이 저작물의 재이용이나 배포의 경우, 이 저작물에 적용된 이용허락조건을 명확하게 나타내어야 합니다.
- 저작권자로부터 별도의 허가를 받으면 이러한 조건들은 적용되지 않습니다.

저작권법에 따른 이용자의 권리는 위의 내용에 의하여 영향을 받지 않습니다.

이것은 [이용허락규약\(Legal Code\)](#)을 이해하기 쉽게 요약한 것입니다.

[Disclaimer](#)

A DISSERTATION FOR THE DEGREE OF DOCTOR OF PHILOSOPHY

**Nondestructive Evaluation of Wood with
Reconstructed Polychromatic X-ray Image**

재구성된 Polychromatic X선 이미지를 이용한
목재 비파괴 평가

AUGUST, 2016

PROGRAM IN ENVIRONMENTAL MATERIALS SCIENCE
DEPARTMENT OF FOREST SCIENCES
GRADUATE SCHOOL
SEOUL NATIONAL UNIVERSITY

CHUL-KI KIM

Abstract

Nondestructive Evaluation of Wood with Reconstructed Polychromatic X-ray Image

Chul-Ki Kim

Program in Environmental Materials Science

Department of Forest Sciences

The Graduate School

Seoul National University

Nondestructive testing and evaluation methods were studied to investigate wood with X-ray image gained by using portable X-ray tube and detector. An attenuation characteristic of polychromatic X-ray was confirmed when the X-ray penetrated into wood, and then the characteristic was used to evaluate air-dry density by employing reconstructed single X-ray image and computed tomography (CT). Tomosynthesis, meanwhile, was suggested to determine inner state of wood located where CT cannot be applied. Dual X-ray absorptiometry was also developed to evaluate moisture content of wood without oven-dry density information of the wood.

A mass attenuation coefficient of wood was derived for evaluating the attenuation characteristic of polychromatic X-ray. In previous study, the mass attenuation coefficient of wood was not influenced by the change of penetration depth. However, the mass attenuation coefficient of wood decreased as the penetration depth increased in this study. It was considered

that the change of wood occurred due to beam hardening, which is the phenomenon that low energy parts are more severely attenuated than high energy parts in the polychromatic X-ray. From the results, the regression between mass attenuation coefficient of wood and penetration depth was found to quantify amount of polychromatic X-ray attenuation in wood. Using the relation of regression, the air-dry density of wood was evaluated with high accuracy, and the root mean square error (RMSE) of accuracy was 0.0103 g/cm^3 when tube voltage of 35 kV was used.

CT image can be reconstructed with numerous numbers of projections. In field of medical, a phantom is generally used as reference material to evaluate CT image quantitatively. However, the method with phantom is hardly to be applied when CT is going to apply in the field. Therefore, modified CT reconstructed algorithm was proposed to make density CT image considering the attenuation characteristic of polychromatic X-ray. The penetration depths were calculated from the cross sectional shape measured by using laser distance meter, and then each X-ray projection was converted to density profile by using the relation of mass attenuation coefficient of wood with the penetration depth. It was found that more than 180 projections were needed to reconstruct density CT image. When it was applied to deteriorated wood member, the modified method could detect insert damage whose diameter was only 2 mm.

In case of existence of obstacle which could make difficult to rotate X-ray apparatus, the applicability of CT can be low as a number of projections are needed to reconstruct CT image turning the X-ray apparatus through at least 180 degrees. Tomosynthesis was studied to surmount the low applicability of CT and to investigate wood. The quality of reconstructed tomosynthesis image was evaluated by using indices such as contrast-to-noise ratio (CNR) and artifact spread function (ASF) to find optimum condition of radiography for reconstructing tomosynthesis image. The accuracy of in-focus plane image

rose as the angular range of X-ray tube and detector. It also rose as the number of projections increased, than leveled off at certain number of projections. In case of vertical resolution, it was not influenced by the number of projections while the angular range effected on the vertical resolution. The vertical resolution increased as the angular range increased. Under the conditions used in this study, it was confirmed that the optimum condition of radiography was 31 projections and angular range of 60 degrees.

The usage of single X-ray densitometry for estimating moisture content of wood has limitation on application, because it is needed to obtain oven-dry density information of specimen. So, dual X-ray absorptiometry was developed to estimate moisture content of wood without oven-dry density information. With the assumption that wood was regarded as mixture of wood substance and moisture, the equation of dual X-ray absorptiometry was proposed. When two X-ray tube voltages, 35 kV and 55 kV, were used for dual X-ray absorptiometry, the highest accuracy was obtained. The RMSE of accuracy was 3.91%. Considering the attenuation characteristic of polychromatic X-ray in wood, the dual X-ray absorptiometry could measure not only the moisture content under fiber saturate point but the distribution of moisture content in wood.

Keywords : Polychromatic X-ray; Wood; Mass attenuation coefficient; CT image; Tomosynthesis; Dual X-ray absorptiometry

Student Number: 2008-23057

Contents

Abstract	i
Contents	iv
List of Tables	vii
List of Figures	viii
1. Introduction	1
1.1. Background	2
1.2. Objectives	6
2. Literature Review	7
2.1. Application of polychromatic X-ray for quantitative assessment	8
2.2. Attenuation characteristic of X-ray in wood	10
2.3. CT for measurement the internal structure of wood	11
2.4. Measurement of moisture content in wood with radiation	13
3. Attenuation Characteristic of Polychromatic X-ray in Wood	15
3.1. Introduction	16
3.2. Attenuation characteristic of monochromatic X-ray and polychromatic X-ray	17
3.3. Materials and experimental methods	19
3.3.1. Materials	19
3.3.2. X-ray apparatus	21
3.3.3. Evaluation of apparent mass attenuation coefficient of wood for polychromatic X-ray	24
3.4. Results and discussion	33
3.4.1. Influence factors on polychromatic X-ray attenuation in wood	33

3.4.2. Estimation of air-dry density of wood considering attenuation characteristic of polychromatic X-ray	53
3.5. Conclusion	57
4. Computed Tomography (CT) for Measuring Air-dry Density	59
4.1. Introduction	60
4.2. CT image reconstruction algorithm	62
4.3. Materials and experimental methods	69
4.3.1. Materials	69
4.3.2. CT apparatus	71
4.3.3. Modification of CT image reconstruction algorithm	73
4.4. Results and Discussion	84
4.4.1. Accuracy of estimation of air-dry density with modified CT reconstruction algorithm	84
4.4.2. Optimum condition to reconstruct density CT image	91
4.4.3. Evaluation of deteriorated wood with density CT image	96
4.5. Conclusion	101
5. Tomosynthesis for Investigating of Inner State of Wood	103
5.1. Introduction	104
5.2. Tomosynthesis reconstruction algorithm	105
5.3. Materials and methods	111
5.3.1. Materials	111
5.3.2. Tomosynthesis apparatus	114
5.3.3. Condition of radiography for investigating of wood with tomosynthesis	116
5.3.4. Evaluation of quality of tomosynthesis image	118
5.4. Results and discussion	120

5.4.1. Optimum condition of radiography for investigating of wood with tomosynthesis	120
5.4.2. Application of tomosynthesis for detecting inner state of wood ..	138
5.5. Conclusion	142
6. Dual X-ray Absorptiometry for Evaluating Moisture Content of Solid Wood	143
6.1. Introduction	144
6.2. Derivation of equation for dual X-ray absorptiometry	146
6.2.1. Apparent mass attenuation coefficient of wood substance and moisture for polychromatic X-ray	146
6.2.2. Assessment of moisture content in wood with dual X-ray absorptiometry	148
6.3. Materials and experimental methods	150
6.3.1. Materials	150
6.3.2. Experimental methods	151
6.3.3. Application of dual X-ray absorptiometry	157
6.4. Results and discussion	160
6.4.1. Derivation of equations for dual X-ray absorptiometry	160
6.4.2. Assessment of moisture content of wood with dual X-ray absorptiometry	170
6.5. Conclusion	181
7. Concluding Remark	183
Appendix	187
References	193
Abstract (Korean)	209

List of Tables

Table 1-1. Classification of nondestructive methods	4
Table 3-1. Details of specimen for three species	20
Table 3-2. Experimental condition for X-ray tube	30
Table 3-3. Integral value of probability function and apparent mass attenuation coefficient of wood	36
Table 3-4. Coefficient of linear regression	39
Table 3-5. One way analysis of variance for the apparent mass attenuation coefficient for three species	42
Table 3-6. Results of t-test between the apparent mass attenuation coefficient of wood and species	43
Table 3-7. Average of apparent mass attenuation coefficient of wood at three tube voltages	48
Table 3-8. Regression coefficient of apparent mass attenuation coefficient of wood	52
Table 4-1. Air-dry density of small specimens measured dimensional method	82
Table 5-1. Radiography conditions to take projections	117
Table 5-2. The least number of projections with 0.8 normalized CNR criteria	126
Table 5-3. y location of 0.5 ASF in various angular ranges and locations of hole	135
Table 6-1. Two groups for developing dual X-ray absorptiometry	159

List of Figures

Figure 3-1. Structure and actual feature of X-ray tube, K-4	22
Figure 3-2. Digital detector, EVS 4343	23
Figure 3-3. Dosimeter with ionization chamber	26
Figure 3-4. Detector sensitivity	28
Figure 3-5. Test set-up for taking projections	29
Figure 3-6. Natural logarithm of ratio of initial to transmitted X-ray energy at penetration depth	34
Figure 3-7. Experimental integral value of the probability function for the penetration depth and the tube voltage	38
Figure 3-8. Apparent mass attenuation coefficients of wood for three species	41
Figure 3-9. Apparent mass attenuation coefficient of wood at three tube voltages	45
Figure 3-10. Average of apparent mass attenuation coefficient of wood at various wood quantities	47
Figure 3-11. Change of apparent mass attenuation coefficient of wood at various penetration depth	51
Figure 3-12. Estimation of air-dry density of wood with apparent mass attenuation coefficient of wood at 35 kV tube voltage	55
Figure 4-1. Fan beam projection	63
Figure 4-2. Geometry of detector plane in fan beam CT system	64
Figure 4-3. Geometry for derivation of the fan beam CT algorithm	66
Figure 4-4. Specimen for the test	70
Figure 4-5. Schematic drawing and picture of CT apparatus	72
Figure 4-6. Flow chart of CT image reconstruction	74

Figure 4-7. Modified flow chart for reconstructing CT image	75
Figure 4-8. Measurement of cross section of specimen with larger distance meter	77
Figure 4-9. Penetration depth according to location of pixel in detector	79
Figure 4-10. Location of small specimens to measure air dry density	81
Figure 4-11. Apparent mass attenuation coefficient at various penetration depths	85
Figure 4-12. Cross section of irregular shape specimen and measured penetration depth	86
Figure 4-13. Three kinds of reconstructed CT image	88
Figure 4-14. Comparison of air-dry density between dimensional method and CT image	90
Figure 4-15. CT images according to number of projection and actual picture of specimen	92
Figure 4-16. Change of air-dry density in CT image with number of projections	94
Figure 4-17. Profile along with line as shown in Figure 4-15f	95
Figure 4-18. Reconstructed CT image with various number of projections	97
Figure 4-19. Density profile for solid line in Figure 4-18	98
Figure 4-20. Binary CT image	100
Figure 5-1. Coronal cross section in tomosynthesis	106
Figure 5-2. Complete isocentric motion for tomosynthesis	107
Figure 5-3. Cone beam geometry of complete isocentric motion	109
Figure 5-4. Two pine wood	112
Figure 5-5. Schematic drawing for tomosynthesis test	115
Figure 5-6. CNR of hole A, B and C according to angular range in various numbers of projections	121

Figure 5-7. Normalized CNR according to location of hole and angular range	123
Figure 5-8. Reconstructed tomosynthesis image according to angular range and number of projection	128
Figure 5-9. Results of single radiograph and reconstructed image	130
Figure 5-10. ASF according to angular range and location of hole	132
Figure 5-11. Reconstructed tomosynthesis image with angular range 60 degrees and 31 projections	137
Figure 5-12. Specimen applied tomosynthesis	139
Figure 5-13. Result of reconstructed tomosynthesis image about stem	140
Figure 5-14. Result of reconstructed tomosynthesis image about wood member	141
Figure 6-1. Picture of decompression chamber	152
Figure 6-2. Test set-up for dual X-ray absorptiometry	154
Figure 6-3. Cracks and cups occurred during oven drying	156
Figure 6-4. Outlier among projections at three tube voltage	161
Figure 6-5. Regression equation with the apparent mass attenuation coefficient of wood substance and	164
Figure 6-6. Apparent mass attenuation coefficient of wood substance and moisture	167
Figure 6-7. Three r values in moisture content	169
Figure 6-8. r value according to moisture content	171
Figure 6-9. Theoretical and experimental result in various moisture content	174
Figure 6-10. Comparison of moisture content with estimated moisture content	176
Figure 6-11. Projection of specimen and estimated distribution of moisture content	180

Chapter 1

Introduction

1.1. Background

Wood is one of valuable materials because it is renewable, wide dispersed, and required relatively small amount of energy to be converted into useful products. Therefore, wood has been widely used through centuries for various purposes such as building, furniture and tool materials. It has been used for their purpose properly with the experience of ancestors.

With the scientific development, people want to use wood as structural member required high mechanical properties. Because wood is a porosity and fibrous material, it has advantage to carry the load efficiently for the direction of alignment of fibers. Because of that, a method began to develop to evaluate mechanical properties of wood. The method is so-called nondestructive evaluation. By definition, nondestructive evaluation is science of identifying the physical and mechanical properties of wood without damaging or altering to its end-use capabilities. The information from nondestructive evaluation enables people to make decision regarding appropriate application. It can provide the properties, performance, or condition of the material in question.

Meanwhile, there are lots of old historic buildings made of wood in Northeast Asia. With their architectural characteristic, wood have an important role to convey a heavy load. Therefore, it has been considered that wood plays an important role in the maintenance of a stability of historic wooden building. To maintain the stability, it is important not to lose their physical and mechanical properties. However, some deterioration could occur by fungi, insect and so on. And they could decrease the properties of wood. Most of deterioration could be found by visual inspection, but some of them do not have external indicators. Therefore, nondestructive evaluation is also needed to determine internal condition of wood in field of conservation.

Since 1960s, nondestructive evaluation has been developed consistently.

Various sources were used according to what they want to evaluate, as shown in Table 1-1. Among those methods, X-ray is a powerful tool to evaluate physical and mechanical properties of wood or to detect decay in wood. X-ray has high resolution results, and it can determine density information. X-ray can also provide the size or location of defect when computed tomography (CT) is used in conjunction. The X-ray CT image can be reconstructed using numerous projections obtained with a rotating X-ray apparatus.

Table 1-1. Classification of nondestructive methods (Bucur, 2013)

Parameter	Properties measured	Techniques
Moisture content	Dielectric properties	Impedance DC and high frequency, microwave, infrared,
	Thermal properties	NMR
	Ionizing ray absorption	Infrared
	Elastic properties	X-ray, gamma-ray Frequency resonance method, ultrasonic method
Density	Weight	Gravimetric method
	Ionizing ray	X-ray micro densitometry; attenuation of X, beta and gamma rays
	Dielectric properties	Microwave technique
	Mechanical properties	Pilodyn
Fiber direction	Elastic properties	Ultrasonic velocity
	Dielectric properties	Microwaves
	Light scattering	Laser, visible light
	Thermal properties	Infrared
Knots detection	Optical properties	CCD camera, colorimetry
	Elastic properties	Ultrasonic CT
	Ionizing radiation	X-ray, gamma ray CT
	Thermal properties	Infrared thermography, laser thermography
Decay detection	Electrical properties	Microwave, NMR
	Elastic properties	Vibration, ultrasonic
	Mechanical properties	Penetration of pilodyn
	Dielectric properties	Microwave
Mechanical capacity	Ionizing radiation	X-ray CT
	Static properties	Bending stress grading, proof-loader
	Dynamic properties	Vibration and ultrasonic methods
	Acoustic properties	Acoustic emission

Despite the advantages of X-ray techniques, X-ray and CT are difficult to use in the field. The equipment is more suitable for laboratory testing, and the radiation shields have to be installed to prevent inspector from hazardous radiation. The general level of radiation intensity is too dangerous to use without a radiation shield. Moreover, it is difficult to install the shield where X-ray test were done. Thus, the first step in solving the field applicability problem was using low X-ray energy from a portable X-ray apparatus. The risk of radiation exposure can be reduced by positioning oneself a sufficient distance from the X-ray tube when low X-ray energy was used. Low energy X-ray has another advantage that it can be generated by a portable X-ray tube which is commercially produced for nondestructive evaluation or security inspections.

In this study, therefore, the attenuation behavior of X-ray from a portable X-ray tube was studied firstly. This is because the attenuation behavior of X-ray from a portable X-ray tube is different when it was compared with the X-ray used in previous studies (Macedo et al., 2002; Olson et al., 1988a; Tiitta et al., 1993). The X-ray generated from portable X-ray tube is polychromatic X-ray, which has a broad spectrum of X-ray energies. Based on the study about polychromatic X-ray attenuation behavior in wood, various reconstruction methods were developed and employed to evaluate wood properties or deterioration in wood. Lastly, the method for improving field applicability was also suggested.

1.2. Objective

The main objective of this study was to develop nondestructive evaluation technique for wood by using polychromatic X-ray. To achieve the objective, the four sub-objective were studies as follows,

1) Firstly, attenuation characteristic of polychromatic X-ray was studied by determining an apparent mass attenuation coefficient of wood. Influence factors on the apparent mass attenuation coefficient of wood were also studied.

2) Modified CT reconstruction algorithm was suggested to reconstruct quantified CT image. Projections gained from portable X-ray apparatus were converted into density profile even though the specimen had irregular shape. Post process of quantified CT image was also conducted to find low density parts in wood.

3) Tomosynthesis, which is method to reconstruct coronal cross section of wood by using projections gained from limited rotation of portable X-ray apparatus, was conducted to investigate wood, and the wood is expected to be located where CT could not be conducted. Various conditions of radiography were found how the quality of reconstructed images was influenced.

4) New method to measure moisture content of wood was developed with two different polychromatic X-ray energies. Based on the assumption that wood consists of wood substance and moisture, the apparent mass attenuation coefficient of those were determined and used to calculate moisture content of wood without oven-dry density information.

Chapter 2

Literature Review

2.1. Application of polychromatic X-ray for quantitative assessment

Since Röntgen discovered X-ray in 1895, X-ray has been a powerful tool in the medical field or the nondestructive evaluation of materials. Either monochromatic or polychromatic X-ray can be produced by each X-ray sources. Monochromatic X-ray having single photon energy is emitted by isotopic source with ^{55}Fe (Woods and Lawhon, 1974) while polychromatic X-ray having broad spectrum of X-ray energies is produced by X-ray tube. Among the sources, Kaelble (1967) suggested that X-ray tube is a simple and reliable equipment which is lower in cost than monochromatic X-ray source. Therefore, X-ray tube emitting polychromatic X-ray is usually used for quantitative assessment.

The X-ray attenuation method has been appreciated as precise method of atomic composition and density (Zou et al., 2011). When X-ray penetrates through a material, the photons in X-ray are either transmitted, scattered (Compton scattering) or absorbed (photoelectric effect) according to its atomic number and density. As a results, the initial intensity of X-ray decreases exponentially as described in Lambert-Beer's law. However, the attenuation of polychromatic X-ray cannot be evaluated by Lambert-Beer's Law. Since all substance attenuate low energy X-rays more strongly than high energy one, primarily because of photoelectric absorption, polychromatic X-ray traversing an absorbing medium becomes proportionately richer in high energy photons, and hence more penetrating, or 'harder' (Brooks and Di Chiro, 1976). It is beam hardening.

Beam hardening in polychromatic X-ray is assuredly the most problematic issue for accurate mineral density determination in medical field (Burghardt et al., 2008). Lately, several researches in the field were reported

to establish to correct beam hardening artifacts to ensure accurate mineral density measurement. One is filtering performed to convert polychromatic X-ray into monochromatic X-ray (Bonse and Busch, 1996; Tucker et al., 1991). However, the intensity of X-ray after filtering is rather impractical because the intensity is reduced by several orders of magnitude by using filtration. So, other studies have been conducted to correct beam hardening artifacts by linearization procedures using wedge calibration or polynomial expansion as correction function (Bonse and Busch, 1996; Burghardt et al., 2008; Luu et al., 2011).

The field of nondestructive evaluation of materials with polychromatic X-ray also considered attenuation characteristic of the X-ray to evaluate material properties correctly. Kotwaliwale et al. (2006) reported that regression equations to predict attenuation coefficient were modelled as a function of penetration depth of X-ray and X-ray tube voltage. The quality of pecan features could be determined by using the regression equations. Influence factors (material type, thickness and X-ray energy) on the attenuation coefficient of water were also studied to monitor moisture movements in building materials (Pease et al., 2012). Nishihata et al. (2012) introduced the probability function of the polychromatic X-ray spectrum with photon energy E to do procedure of linearization base on a characteristic curve. Considering the linearization procedure, quantitative evaluation of aluminum part was conducted.

2.2. Attenuation characteristic of X-ray in wood

A transmitted X-ray intensity arrived the detector is related to the wood density. Therefore, relative wood density can be quantified by considering attenuation characteristic with mass attenuation coefficient and thickness of wood. Since Laufenberg (1986) had described the calculation of mass attenuation coefficient of wood as a summation of the coefficient of each elemental components and proportional to elemental mass fractions, numerous studies about mass attenuation coefficient of wood have been conducted to measure wood density (Liu et al., 1988; Macedo et al., 2002; Olson et al., 1988b; Tiitta et al., 1993).

However, it is still necessary to study of the attenuation characteristic of polychromatic X-ray in wood. The studies about the mass attenuation coefficient of wood were done without considering the attenuation characteristic of polychromatic X-ray. Hoag and Krahmer (1991) approximately evaluated the mass attenuation coefficient of wood with the fundamental exponential relationship (Lambert-Beer's law). Using polychromatic X-ray with 30 keV, the mass attenuation coefficient of 0.638 cm²/g was determined for Douglas-fir at 9% equilibrium moisture content. Kim et al. (2006a) and Kim et al. (2014) also measured the mass attenuation coefficient of wood with Lambert-Beer's law although polychromatic X-ray from portable X-ray tube was used in their studies. Those studies found that the mass attenuation coefficient of wood decreased as the thickness of specimens increased. Meanwhile, Solbrig et al. (2015) insisted that the accuracy and capability of X-ray measuring devices seems questionable so, while X-ray densitometry are widely spread in wood-based composite industry, the attenuation characteristic of polychromatic X-ray in wood should be studied.

2.3. CT for measurement the internal structure of wood

CT image reconstructed with X-ray projections is obtained from rotation of X-ray tube and detector around the specimen. CT image can show the internal information like the location and size of defects. In wood science, CT has been usually used to measure the internal structure of wood for assessing wood quality (Houllier et al., 1995; Kershaw et al., 2009; Longuetaud et al., 2004; Oja, 2000; Wei et al., 2009).

It is important to know geometry and location of knot in a sawmill for optimizing cutting decisions or improving the grading of logs or lumber (Longuetaud et al., 2012). Funt and Bryant (1987) used threshold of the gray level in CT image to classify the pixels into four classes, where knots indicated the highest density. Oja and Temnerud (1999) provided reconstructed CT image to detect sound knot and dead knot border for Norway spruce. With the reconstructed CT image, the knots larger than 7 mm were detected with 94% in average accuracy.

To detect another defect in log, several studies also conducted. Espinoza et al. (2005) used X-ray scanner to identify and locate main internal characteristics for sugar maple. The green density, basic density and moisture content of each location were also measured to assess within-tree variations between logs. A novel approach using Kalman filter-based tracking algorithms was also introduced to simultaneously detect, classify, and localize defects in 3-dimensional CT image (Bhandarkar et al., 2006). Wei et al. (2009) tested both back-propagation artificial neural network (ANN) and maximum likelihood classifier (MLC) to confirm the feasibility of identifying internal wood characteristics in CT image.

Few studies also conducted to develop the portable equipment designed

to be used for in situ inspection of tree or wood member of historic building. Gamma ray, which is monochromatic radiation, were used for imaging the transversal section of tree (Bucur, 2013). Kim et al. (2006b) carried out for development of a portable X-ray CT system with portable X-ray tube and X-ray film to detect deterioration of wood members in buildings. It was shown that the system developed in the study could be used not only to determine the shape, size and position of defects but also to find the density distribution in cross section of wood member. Kim et al. (2014) also developed portable X-ray CT system consisted of portable X-ray tube and digital detector. Using the relationship between the mass attenuation coefficient of wood and penetration depth, density profile was determined in CT image.

2.4. Measurement of moisture content in wood with radiation

Studies of X-ray densitometry conducted to measure not only moisture content but also moisture distribution in wood. It has advantage to investigate average moisture content in thick wood with a higher resolution than other nondestructive evaluation (Tiitta et al., 1993). Tiitta et al. (1993) used gamma ray to determine the moisture distribution of wood. They reported that the gamma ray could be applied to measure the moisture content of fiber saturation point and above. Watanabe et al. (2008) and Tanaka et al. (2009) calculated distribution of moisture by using the digital X-ray microscope for Japanese cedar during drying process. From the results of those studies, X-ray densitometry could be used to calculate the progressive change in moisture content and moisture distribution in wood. However, the information of the oven-dry density should be needed for the calculations. It means that the calculations cannot be started unless the specimens are oven-dried (Kim et al., 2015). Therefore, these methods are not applicable to specimens which cannot be dried out like living tree or engineering wood.

Dual-energy X-ray absorptiometry (DXA), which is a method using two X-ray energies to measure moisture content in wood without an information of oven-dry density, has been introduced recently. Hultnäs and Fernandez-Cano (2012) conducted DXA to measure moisture content of wood chip with errors of 1.39–2.57% for mixed species. Tanaka and Kawai (2013) reported that DXA showed the possibility to evaluate moisture content of solid wood with 15 mm thickness for Japanese cedar. They also reported that the error in measuring moisture content was approximately 20% for the range of moisture content of 0–120%. There is another study for measuring moisture content in

solid wood with DXA (Kim et al., 2015). A digital detector was used to improve the accuracy of moisture content measurement, and the error of 3.15% was obtained in the 28.68–172.81% moisture content range. However, the dissimilarity between theoretical equation and experimental result was occurred in DXA for solid wood.

Chapter 3

Attenuation Characteristic of Polychromatic
X-ray in Wood

3.1. Introduction

Since Phillips (1960) first conducted the radiation method to measure wood density, various studies have been reported how it could be used to estimate the wood density (Bergsten et al., 2001; Cown and Clement, 1983; Hoag and Krahmer, 1991; Olson et al., 1988a). If the radiation amount absorbed in wood is evaluated, the wood density can be estimated indirectly. A characteristic of X-ray absorption in wood is represented as a mass attenuation coefficient of wood. The mass attenuation coefficient characterizes how easily the wood can be penetrated, and it is related to the attenuating material and the X-ray energy (Kaelble, 1967).

In wood science, monochromatic sources were usually used to measure wood density. The monochromatic radiation from the sources involves single photon energy, and it is easy to measure the amount of absorption as described by the Lambert-Beer's law. Instead of monochromatic sources, however, polychromatic sources, which are X-ray tubes, are mainly used in the wood industry. The polychromatic sources are not only lower in cost than monochromatic radiation equipment but also a simple reliable tools (Kaelble, 1967). Although an usage of polychromatic X-ray increased in wood science, few studies have been conducted to evaluate the characteristic of X-ray absorption in wood.

In this chapter, the mass attenuation coefficients of wood were determined at polychromatic X-ray energies, three species (larch, pine and Korean pine) and various penetration depths of X-rays. And equations of the mass attenuation coefficient according to influential factor were introduced. Air-dry density of wood was measured by using the equations and the accuracy of measurement was also validated.

3.2. Attenuation characteristic of monochromatic X-ray and polychromatic X-ray

For monochromatic X-ray in homogeneous material, the Lambert-Beer's law describes the relation between the initial X-ray intensity (I_0) and the transmitted X-ray intensity (I_{mono}) after penetrating the material,

$$I_{mono} = I_0 e^{-\mu \rho t} \quad (3-1)$$

where, I_{mono} is the transmitted X-ray intensity (μGy), I_0 is the initial X-ray intensity (μGy), μ is the mass attenuation coefficient (cm^2/g), ρ is the air-dry density (g/cm^3), and t is the penetration depth in wood (cm). Only in case of monochromatic X-ray, Equation 3-1 is valid (Krumm et al., 2008). In case of polychromatic X-ray, the mass attenuation coefficient is energy dependent. Furthermore the detector system also has energy dependent efficiency. These energy dependencies can be regarded as weighting factors which are associated with X-ray energy in the broad spectrum of wavelength. The relation between the initial polychromatic X-ray intensity (I_0) and the transmitted X-ray intensity (I_{poly}) can be expressed by the following expression (Lifton et al., 2013; Nishihata et al., 2012),

$$I_{poly} = I_0 \int_E S(E) D(E) \exp\left(-\int_t \mu(E) \rho dt\right) dE \quad (3-2)$$

$$\text{with } \int_E S(E) D(E) dE = \int_E W(E) dE = \alpha \quad (3-3)$$

where, I_{poly} is the transmitted X-ray intensity (μGy), $S(E)$ is the X-ray beam spectrum, $D(E)$ is the energy dependent detection efficiency, $\mu(E)$ is an mass attenuation coefficient of wood for energy E (cm^2/g), and $W(E)$ is the probability function of the polychromatic X-ray according to the energy E .

3.3. Materials and experimental methods

3.3.1. Materials

Specimens from the three species – Korean pine (*Pinus koraiensis*), pine (*Pinus densiflora*) and larch (*Larix leptolepis*) – were prepared in this study, and the number of specimens was ten per each species. Table 3-1 shows the information of specimens. The direction of X-ray penetration in wood can be described as radial, tangential and mixed direction. The term of ‘radial’ direction was used when the annual ring was perpendicular to the direction of X-ray penetration, and ‘tangential’ direction was used when tangential line of annual ring was parallel to that. When a direction do not matched the radial nor tangential direction, the ‘mixed’ direction was used. A longitudinal direction was not considered in this study. The average air-dry density of Korean pine, pine and larch were $0.40 \text{ g/cm}^3 \pm 0.01 \text{ g/cm}^3$, $0.52 \text{ g/cm}^3 \pm 0.02 \text{ g/cm}^3$ and $0.58 \text{ g/cm}^3 \pm 0.05 \text{ g/cm}^3$, while the average moisture contents were $8.32\% \pm 0.26\%$, $9.44\% \pm 0.20\%$ and $9.44\% \pm 0.27\%$, respectively. Moisture content of the specimens was measured by using the oven-dry method.

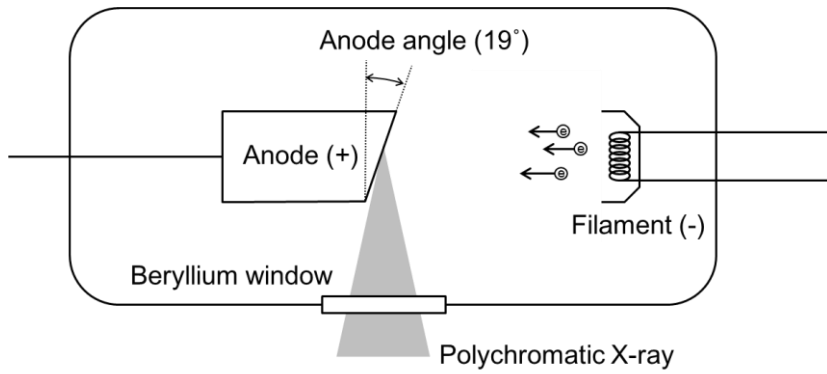
Table 3-1. Details of specimen for three species

Species	Weight (g)	Size (mm)			Density (g/cm ³)	MC (%)	Penetration direction	
		W	T	L				
Korean Pine	1	81.03	49.38	20.00	199.13	0.41	8.56	Mix.
	2	77.32	49.62	20.08	199.41	0.39	8.47	Mix.
	3	81.61	49.46	20.12	199.86	0.41	8.26	Mix.
	4	77.63	49.77	20.15	198.05	0.39	8.44	Tan.
	5	80.07	49.66	20.23	199.31	0.40	8.16	Mix.
	6	77.26	49.68	19.84	198.91	0.39	8.21	Tan.
	7	80.69	49.57	20.12	199.51	0.41	8.32	Mix.
	8	79.66	49.53	20.09	199.03	0.40	8.68	Mix.
	9	80.27	49.10	20.13	199.68	0.41	7.74	Mix.
	10	78.92	49.46	20.23	199.77	0.39	8.38	Tan.
Pine	1	98.70	49.58	20.27	199.28	0.49	9.44	Mix.
	2	106.73	49.8	20.36	199.49	0.53	9.69	Rad.
	3	105.74	49.41	20.03	199.6	0.54	9.76	Rad.
	4	108.33	49.68	20.27	199.54	0.54	9.26	Mix.
	5	105.13	49.63	19.89	199.45	0.53	9.08	Mix.
	6	109.50	49.64	20.02	199.64	0.55	9.31	Tan.
	7	102.12	49.68	20.24	198.29	0.51	9.50	Rad.
	8	108.04	50.01	20.02	199.11	0.54	9.36	Mix.
	9	98.08	49.75	20.07	199.37	0.49	9.60	Mix.
	10	100.83	49.45	20.15	199.38	0.51	9.39	Mix.
Larch	1	130.37	50.13	20.24	200.03	0.64	9.67	Mix.
	2	102.75	49.92	20.08	199.87	0.51	10.02	Mix.
	3	117.82	49.88	20.20	199.67	0.59	9.17	Mix.
	4	132.95	49.89	20.10	199.98	0.66	9.27	Mix.
	5	108.35	49.85	20.30	199.49	0.54	9.42	Mix.
	6	120.08	49.76	20.17	200.11	0.60	9.27	Mix.
	7	102.88	49.86	20.30	199.96	0.51	9.35	Mix.
	8	116.20	49.71	20.16	201.03	0.58	9.68	Mix.
	9	115.78	49.87	20.18	200.19	0.57	9.39	Mix.
	10	116.71	49.63	20.12	200.14	0.58	9.15	Mix.

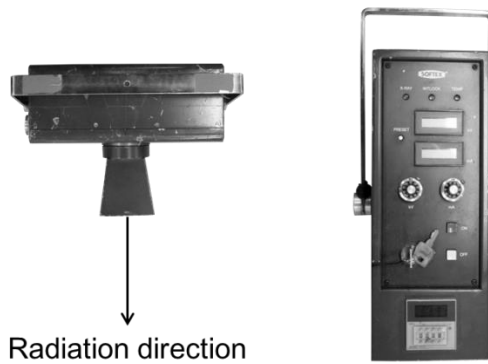
3.3.2. X-ray apparatus

The K-4 (Softex, Japan) was used as an X-ray tube, and it generates polychromatic X-ray by colliding high velocity electrons with target metal. The maximum tube voltage to accelerate the electrons is 64 kV, and the maximum tube current is 5 mA. This X-ray tube can be used in situ testing in conformity to Korean Nuclear Safety Act. The target metal of the K-4 is tungsten with 19° anode angle. Figure 3-1 shows the internal structure and actual feature of K-4.

Figure 3-2 shows the digital detector EVS 4343 (DRtech., Korea) used to take projections in this study. The scintillator of detector is made of Cesium. The active area of detector and pixel pitch of the projections were 430 mm × 430 mm and 140 μm, respectively. The projections were directly saved in a laptop as DICOM files.



(a) Structure of X-ray tube



(b) Actual feature of X-ray tube

Figure 3-1. Structure and actual feature of X-ray tube, K-4

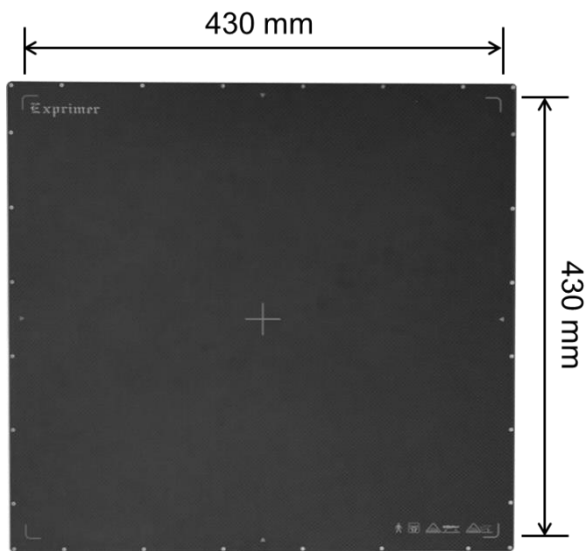


Figure 3-2. Digital detector, EVS 4343

3.3.3. Evaluation of apparent mass attenuation coefficient of wood for polychromatic X-ray

As shown in Equation 3-2 and 3-3, the probability function of the polychromatic X-ray is related with X-ray beam spectrum and X-ray energy dependent detection efficiency. Various studies to calculate the probability function have been reported (Engelhardt et al., 2008; Nik et al., 2011; Schlomka et al., 2008; Taguchi et al., 2010), but the alternative experimental method was used in this study. From Equation 3-2 and 3-3, Equations from 3-4 to 3-7 were derived,

$$I_{poly}/I_0 = \int_E W(E) \exp\left(-\int_t \mu(E) \rho dt\right) dE = \int_E W(E) \exp(-\mu(E) \rho t) dE \quad (3-4)$$

Equation 3-5 and 3-6 were obtained from integration by parts of Equation 3-4,

$$I_{poly}/I_0 = \alpha \exp(-\mu(E) \rho t) - \alpha \int_E \left(-\frac{d(\mu(E) \rho t)}{dE}\right) \exp(-\mu(E) \rho t) dE \quad (3-5)$$

$$I_{poly}/I_0 = 2\alpha \exp(-\mu(E) \rho t) \quad (3-6)$$

Equation 3-7 is natural logarithm of Equation 3-6,

$$\ln(I_0/I_{poly}) = \mu(E) \rho t - \ln(2\alpha) \quad (3-7)$$

Equation 3-7 was the regression model to calculate the integral value of probability function and mass attenuation coefficient. The least square method

was used to calculate those values. The mass attenuation coefficient of wood was designated as the apparent mass attenuation coefficient of wood because it was derived from the experimental method.

For finding the integral value of probability function and apparent mass attenuation coefficient of wood, intensities of X-ray needed to be measured. A dosimeter with the flat shadow free diagnostic ionization chamber (SFD chamber), whose sensitive volume was 6 cm^3 , was used to measure the average initial X-ray energy reached the detector (Figure 3-3).



(a) UNIDOSE E Universal Dosimeter



(b) SFD chamber of 6 cm³

Figure 3-3. Dosimeter with ionization chamber
(source: <http://www.ptw.de>)

On the other hand, the transmitted X-ray intensity was calculated by using a linear relationship between gray scale and quantity of ionizing radiation. Figure 3-4 shows the linear relationship, which was offered by the manufacturing company (DRtech, Korea).

Figure 3-5 shows the schematic drawing for taking projections, and the distance between the tube and detector was set to 1209.2 mm. According to ASTM E 1742/1742 M-12, an image quality indicator (IQI) was attached at the upper-right corner of the detector to check whether the quality of projection was consistent or not. It was considered as an outlier of radiographs when the gray scale value of IQI was not included within a 1.5-fold interquartile range of the lower quartile or that of upper quartile.

Three kinds of tube voltages of 35 kV, 45 kV and 55 kV were chosen to calculate the integral value of probability function and apparent mass attenuation coefficients of wood. The tube current of 5 mA was maintained during the experiment. Table 3-2 shows the initial X-ray energies according to the test conditions.

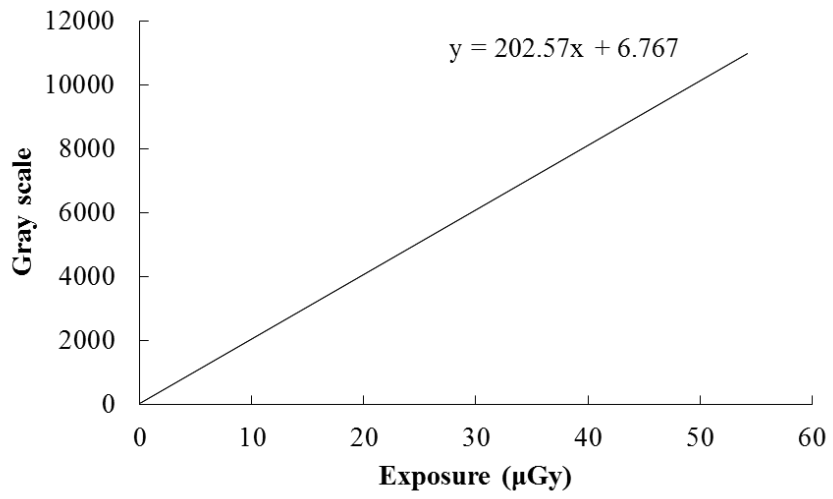


Figure 3-4. Detector sensitivity
(information provided by DRtech.)

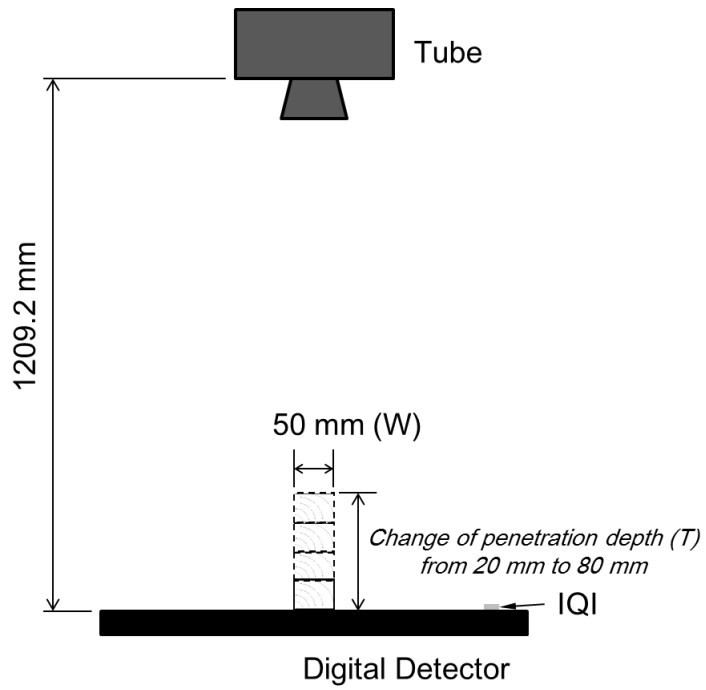


Figure 3-5. Test set-up for taking projections

Table 3-2. Experimental condition for X-ray tube

Classification			Radiation dose (μ Gy)
Tube voltage (kV)	Tube current (mA)	Radiation time (sec)	
35	5	2.0	3012
45	5	1.2	2554
55	5	0.7	1904

The penetration depths were altered by changing the number of wood blocks of the specimens from one to four as shown the Figure 3-5. The range of penetration depth was from 20 mm to 80 mm. Projections with the various penetration depth were taken by exposing the detector to X-ray for different exposing time as listed in Table 3-2. The total number of projections according to the penetration depths of 20 mm, 40 mm, 60 mm and 80 mm was 10, 25, 25 and 25 per each species. The average air-dry density of the wood blocks according to the penetration depth was also calculated. Equation of 3-8 shows how to calculate the air-dry density of wood,

$$D_{air-dry} = \frac{\sum_{k=1}^n m_k}{\sum_{k=1}^n V_k} \quad (3-8)$$

where, n is the total number of wood block to calculate apparent mass attenuation coefficient, $D_{air-dry}$ is the air-dry density of the wood blocks (g/cm^3), m_k is the mass of k th wood block in the equilibrium with the atmospheric condition (g) and V_k is the volume of k th wood block in the equilibrium with the atmospheric condition (cm^3).

Air-dry density also estimated by using the values determined from Equation 3-7 with the least squared method as follows,

$$\rho = \frac{\ln\left(\left(I_0/I_{poly}\right)2\alpha\right)}{\mu(E)t} \quad (3-9)$$

All the results of radiographs from the specimens were divided into two groups; group 1 and group 2. Firstly, the results in group in 1 were used to calculate the integral value of the probability function and apparent mass

attenuation coefficient of wood. The number of analyzed results in group 1 at penetration depth of 20 mm, 40 mm, 60 mm and 80 mm was 5, 15, 15 and 15, respectively. Secondly, the results in group 2 were used to validate the accuracy of the estimated air-dry density. The number of tested results according to the penetration depth of 20 mm, 40 mm, 60 mm and 80 mm was 5, 10, 10 and 10. The root mean squared error (RMSE) was used to evaluate the difference between estimated air-dry densities and measured air-dry densities as shown in Equation 3-10,

$$RMSE = \sqrt{\sum_{j=1}^n (M_{j,e} - M_{j,a})^2 / n} \quad (3-10)$$

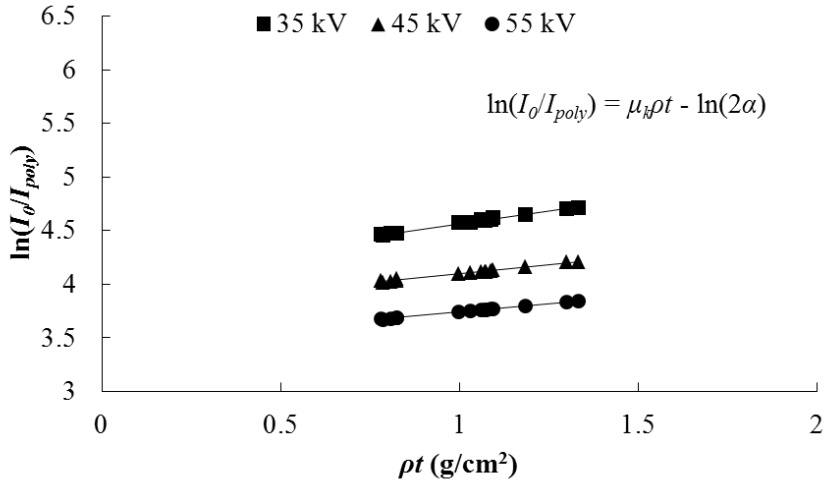
where, n is total number of data for validation of the accuracy of estimated air-dry density, $M_{j,e}$ and $M_{j,a}$ are the estimated air-dry density by using projection and the measured air-dry density by using dimensional method.

The projections used to calculate apparent mass attenuation coefficient and to confirm the value of IQI were analyzed via MATLAB R2015b (MathWorks, USA) and ImageJ (Rasband, 2008) programs.

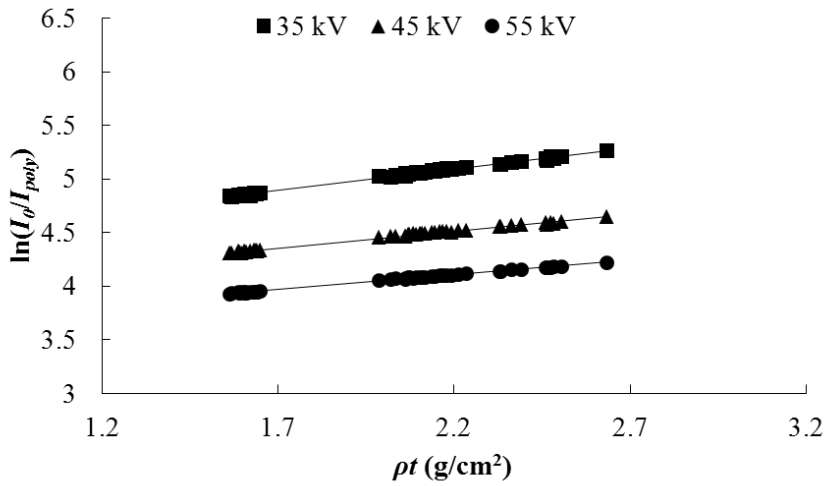
3.4. Results and discussion

3.4.1. Influence factors on polychromatic X-ray attenuation in wood

The 150 projections in group 1 were analyzed to calculate the integral value of probability function and apparent mass attenuation coefficient in Equation 3-7. It has been reported that the probability function of polychromatic X-ray could be estimated via X-ray transmission measurement (Lifton et al., 2013; Nishihata et al., 2012; Sidky et al., 2005). Lifton et al. (2013) estimated the function by using the X-ray transmission measurement with linear attenuation coefficients of homogeneous material, which is product of mass attenuation coefficients and density of homogeneous material and various penetration depth. Therefore natural logarithm of ratio of initial to transmitted X-ray energy was calculated according to wood quantity, which was product of air-dry density and penetration depth, and tube voltage. The integral values of probability function were y-intercept in Figure 3-6 as shown in Equation 3-7. On the other hand, apparent mass attenuation coefficients of wood were gradients of wood quantities. Figure 3-6 and Table 3-3 shows the integral values of probability function and the apparent mass attenuation coefficient of wood.

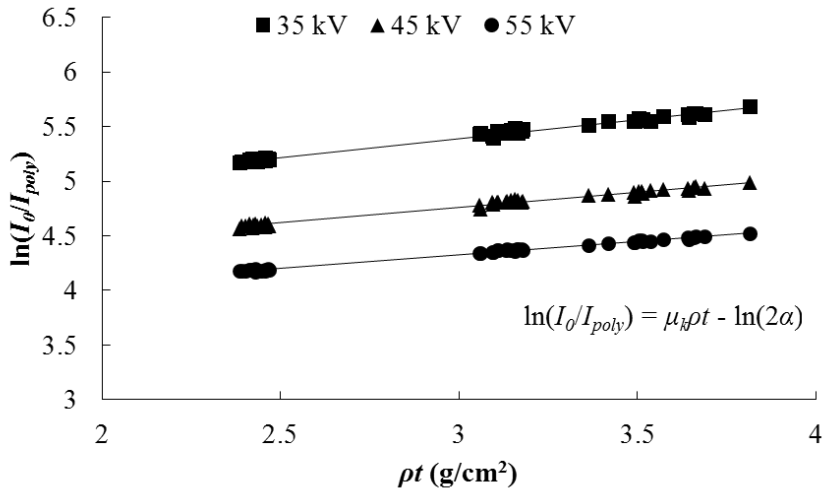


(a) Pentation depth: 2 cm

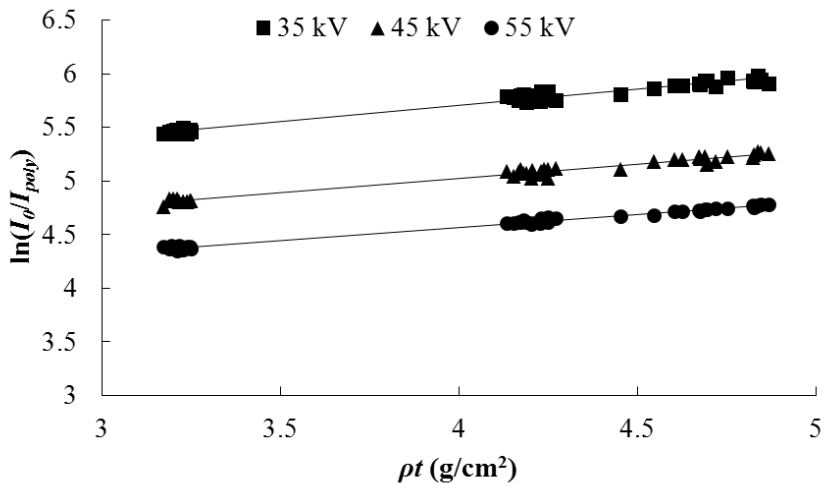


(b) Pentation depth: 4 cm

Figure 3-6. Natural logarithm of ratio of initial to transmitted X-ray energy at penetration depth (continue)



(c) Penetration depth: 6 cm



(d) Penetration depth: 8 cm

Figure 3-6. Natural logarithm of ratio of initial to transmitted X-ray energy at penetration depth

Table 3-3. Integral value of probability function (α) and apparent mass attenuation coefficient of wood (μ_k)

Tube voltage (kV)	Penetration depth (mm)	μ_k (cm ² /g)	α	R ²
35	20	0.4716	0.0083	0.99
	40	0.3999	0.0074	0.99
	60	0.3472	0.0065	0.99
	80	0.3034	0.0056	0.98
45	20	0.3451	0.0117	0.99
	40	0.3178	0.0110	0.99
	60	0.2814	0.0100	0.99
	80	0.2673	0.0096	0.98
55	20	0.3038	0.0161	0.99
	40	0.2740	0.0151	0.99
	60	0.2467	0.0139	0.99
	80	0.2420	0.0137	0.99

Figure 3-7 shows the integral value of the probability function with the penetration depth of wood. The integral value of the probability function decreased as the penetration depth of wood increased. At the same tube voltage, the probability that transmitted X-ray activates the detector could decrease as the penetration depth increased. This is because the penetration depth of wood affects the intensity of X-ray. More reduced X-ray intensity has less probability to excite the detector, which is related with the energy dependent detection efficiency. On the other hand, the integral values were positively correlated with the changes in the tube voltage. The penetration ability of X-ray depends on the energy of photon. For polychromatic X-ray, the effective energy, which designates the energy having the same penetration ability as monochromatic X-ray, is used to evaluate the penetration ability. Waggener et al. (1972) reported X-ray spectra according to tube voltages from 25 to 110 kVp and the effective energies for the X-ray spectra. It was found that the positive correspondence between the tube voltages and the effective energies. Therefore, there is a high possibility that detector reacts easily to X-ray with high tube voltage.

Table 3-4 shows the coefficient of the linear regression for the integral value of the probability function according to the penetration depth and the tube voltage. These linear regressions were used to calculate the apparent mass attenuation coefficients of wood and to validate the accuracy of air-dry density estimation in this chapter.

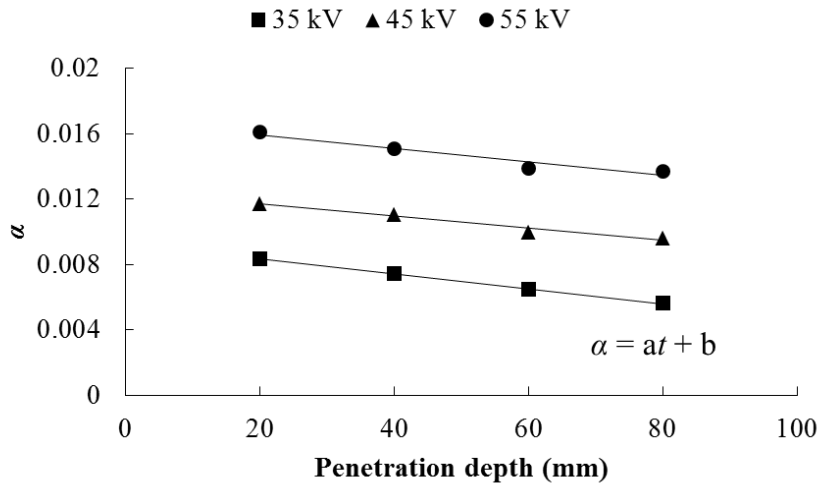


Figure 3-7. Experimental integral value of the probability function (α) for the penetration depth and the tube voltage

Table 3-4. Coefficient of linear regression, $\alpha = at + b$, where, α is the experimental integral value of the probability function, t is the penetration depth and a, b are the coefficients of the linear regression

Tube voltage (kV)	a	b	R ²
35	-0.00046	0.0092	0.99
45	-0.00037	0.0124	0.97
55	-0.00041	0.0168	0.94

Figure 3-8 shows the apparent mass attenuation coefficients of wood according to species at the tube voltage of 35 kV, and the penetration depth was 20 mm. It seemed that the species have no effect on the apparent mass attenuation coefficient of wood. The statistical results of the one way analysis of variance and the t-test between two species, Larch–Pine, Pine–Korean pine and Larch–Korean pine also indicated that there is no significant effect of species on the apparent mass attenuation coefficient of wood with 95% confidence interval. Table 3-5 and Table 3-6 show those results.

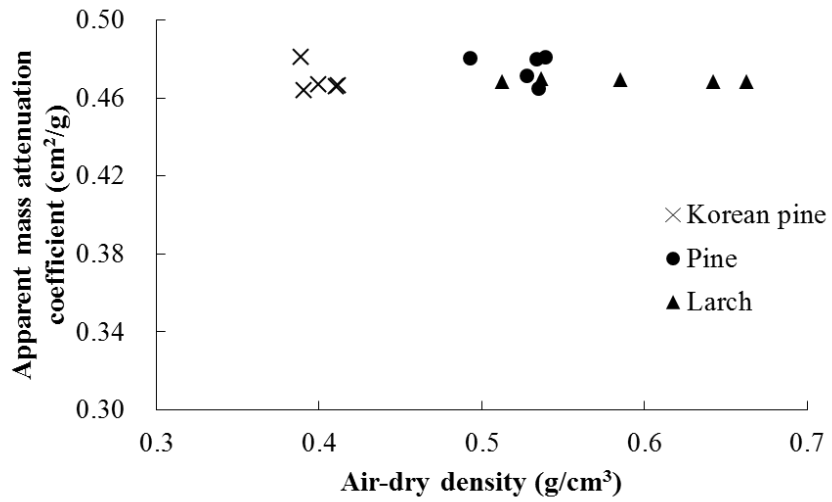


Figure 3-8. Apparent mass attenuation coefficients for three species

Table 3-5. One way analysis of variance for the apparent mass attenuation coefficient for three species

Source	Sum of squares	df	Variance estimate	<i>F</i> ratio	P value
Between groups	0.00015	2	0.0000731	2.177	0.156
Within groups	0.00040	12	0.0000336		
Total	0.00055	14			

Table 3-6. Results of t-test between the apparent mass attenuation coefficient of wood and species

	Larch	Pine	Korean pine
Larch	-	-	-
Pine	0.075* (-2.044**, 8***)	-	-
Korean Pine	0.981 (0.025, 8)	0.175 (1.487, 8)	-

* P value of two-tail

** t-test

*** df, degree of freedom

The mass attenuation coefficient of wood has been determined by many authors with several methods using X-ray and gamma-ray. However, the results of the mass attenuation coefficients for different species were inconsistent. Malan and Marais (1992) reported that variation in the mass attenuation coefficients between and within wood was explained by the difference in chemical composition. Meanwhile, changes in volume percentage of cellulose, hemicellulose and lignin did not have significant effect on the changes of absorption coefficient (Lindgren, 1991), which was related with the mass attenuation coefficient. Moreover, Olson et al. (1988b) reported that the ash element in wood did not have influence on the wood density calculations because Carbon and Oxygen content, which have large elemental weight fractions, have a dominant role in calculation of wood density. The apparent mass attenuation coefficients of wood were not influenced by the species as well in this study.

Figure 3-9 shows the apparent mass attenuation coefficient of wood at three different tube voltages. As the tube voltage increased, the apparent mass attenuation coefficient of wood decreased. This result agreed with the previous study about the mass attenuation coefficient of wood (Hoag and Krahmer, 1991). At increased tube voltage, more accelerated electrons can be produced, and the intensity of effective energy in polychromatic X-ray also increases. Therefore, more transmitted X-ray energy reached when the high intensity of effective energy was developed. Then, the ratio of initial to transmitted X-ray energy is closer to 1, and the apparent mass attenuation coefficient is also closer to 0.

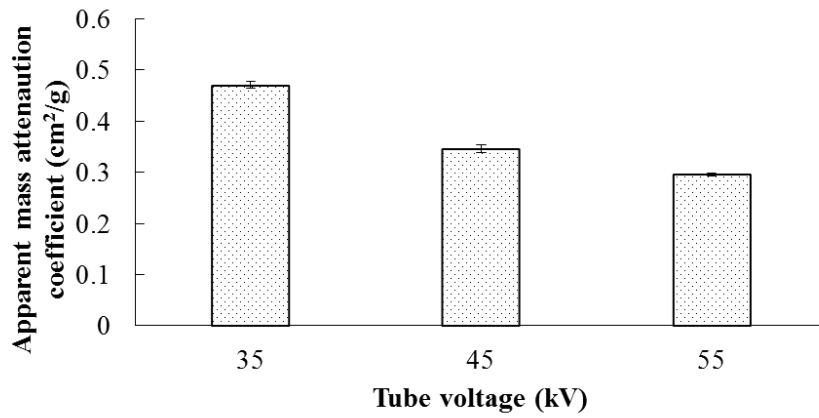


Figure 3-9. Apparent mass attenuation coefficient at three tube voltages

The total number of specimens in group 1 was 150, and the penetration depth was 20 mm, 40 mm, 60 mm and 8 mm. Figure 3-10 presents the ratio of initial X-ray energy to transmitted X-ray energy versus wood quantity for all results in group 1. The species was not considered as an influential factor on the apparent mass attenuation coefficient in this analysis because it was verified that the apparent mass attenuation coefficient was not affected by changing the species in the previous section. For all results disregarding penetration depths, the gradient of linear regression was calculated by Equation 3-7. The gradient refers to an average of apparent mass attenuation coefficients. Table 3-7 presents the average of the apparent mass attenuation coefficients at three tube voltages, 35 kV, 45 kV and 55 kV, and it shows the average of apparent mass attenuation coefficient of wood decreased as the tube voltage increased. However, the instantaneous gradient of linear regression, which was mass attenuation coefficient of wood at certain wood quantity, decreased constantly as the wood quantities increased as shown in Table 3-3.

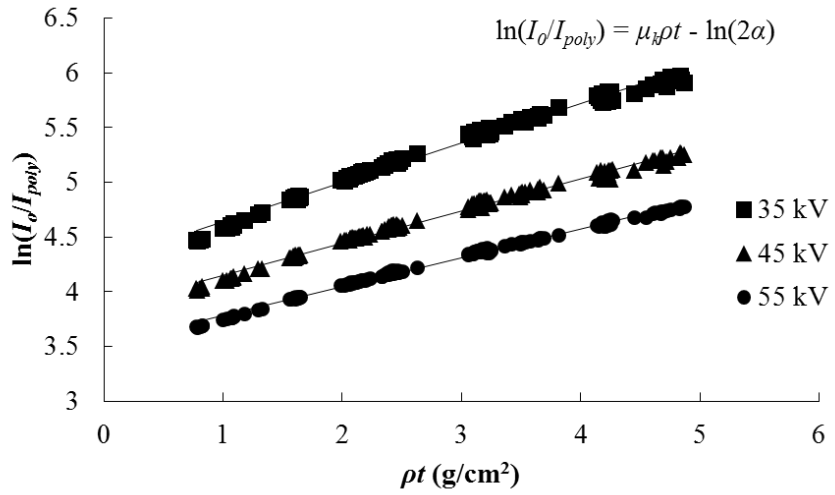


Figure 3-10. Average of apparent mass attenuation coefficient of wood (μ_k) at various wood quantities

Table 3-7. Average of apparent mass attenuation coefficient of wood (μ_k) at three tube voltages

Tube voltage (kV)	μ_k (cm ² /g)	α	R ²
35	0.3590	0.0069	0.99
45	0.2953	0.0106	0.99
55	0.2642	0.0148	0.99

The apparent mass attenuation coefficient of wood varies with changing of the penetration depth. Table 3-3 shows how the penetration depth affects the apparent mass attenuation coefficient of wood. They present the apparent mass attenuation coefficient of wood at four penetration depth, 20 mm, 40 mm, 60 mm and 80 mm. The apparent mass attenuation coefficient of wood decreased as the penetration depth increased.

It was considered that main factor caused the change of mass attenuation coefficient of wood according to the penetration depth was beam hardening of polychromatic X-ray. When polychromatic X-ray propagates through a material, low energy parts are more severely attenuated than high energy parts in the polychromatic X-ray (Brooks and Di Chiro, 1976; Burghardt et al., 2008; Lifton et al., 2013; Pease et al., 2012). After penetrating material, as a result, the proportion of high energy parts in the polychromatic X-ray increased as the penetration depth of polychromatic X-ray increased. It means that more penetrating polychromatic X-ray became harder. Therefore the attenuation shown as Equation 3-7, the natural logarithm of the ratio of initial to transmitted X-ray including the experimental integral value of the probability function, was not exactly proportional to the penetration depth of wood.

The function of apparent mass attenuation coefficient of wood with the penetration depth was induced to reflect the beam hardening in wood. From the results in group 1, the relationships between the apparent mass attenuation coefficient and penetration depth were shown in Figure 3-11. Table 3-8 summarizes the regression coefficients and the coefficients of determination of the relationships. The variation of apparent mass attenuation coefficient of wood according to penetration depth was greater at low tube voltage condition, 35 kV. Poludniowski et al. (2009) reported that the fraction of low energy radiation in polychromatic X-ray

was higher at low tube voltage condition than at higher tube voltage condition. Therefore, the change of the apparent mass attenuation coefficient of wood according to the penetration depth increased as tube voltage decreased.

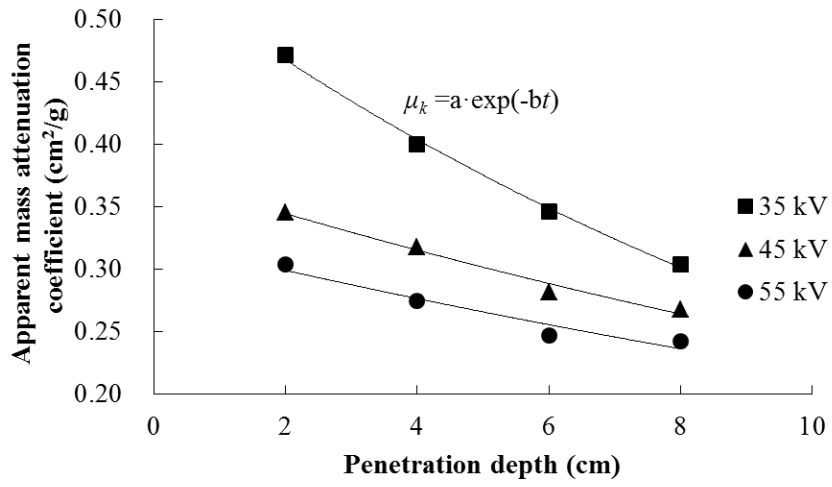


Figure 3-11. Change of apparent mass attenuation coefficient of wood at various penetration depths

Table 3-8. Regression coefficient of apparent mass attenuation coefficient of wood, $\mu_k = a \times \exp(-bt)$

Tube voltage (kV)	a	b	R ²
35	0.5414	0.073	0.99
45	0.3763	0.044	0.98
55	0.3233	0.039	0.94

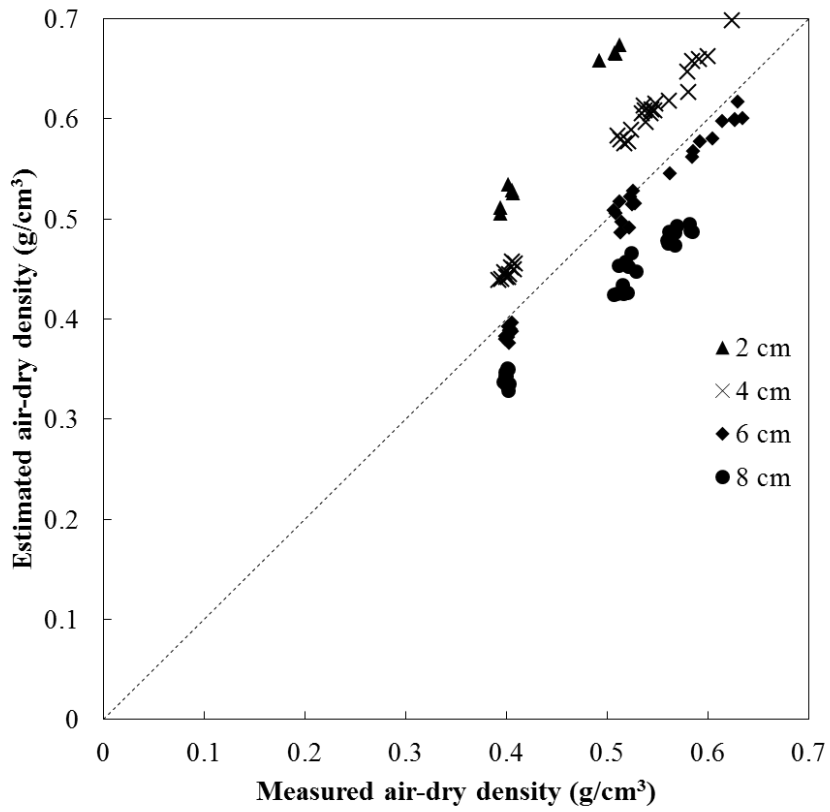
3.4.2. Estimation of air-dry density of wood considering attenuation characteristic of polychromatic X-ray

In the previous discussion, it was shown that the apparent mass attenuation coefficient of wood was influenced by the penetration depth in wood while species did not affect the change of the apparent mass attenuation coefficient. And the integral value of probability function had to be considered when polychromatic X-ray was used to investigate wood properties. Based on these results, estimation of air-dry density of wood in group 2 was conducted by using the relationship of the apparent mass attenuation coefficient with the penetration depth.

The densities of the specimens in group 2 were calculated by using the Equation 3-8, and two different values of apparent mass attenuation coefficients were used to estimate air-dry density. One is the average of apparent mass attenuation coefficients, and the other is variable apparent mass attenuation coefficients with penetration depth. The average of apparent mass attenuation coefficients of wood was obtained from the gradient of linear regression of natural logarithm of ratio of initial to transmitted X-ray energy versus wood quantity (Table 3-7). At tube voltage of 35 kV, the average of apparent mass attenuation coefficients was 0.3590 and the density can be calculated by the equation: $\rho = \ln((I_0/I) - (0.0009t + 0.0185)) / (0.3590t)$. The variable apparent mass attenuation coefficients were calculated by using the values in Table 3-8, and apparent mass attenuation coefficients at 35 kV were expressed as $0.5414t \times \exp(-0.073t)$, and the density can be calculated by the equation: $\rho = \ln((I_0/I) - (0.0009t + 0.0185)) / (0.5414t \times \exp(-0.073t))$.

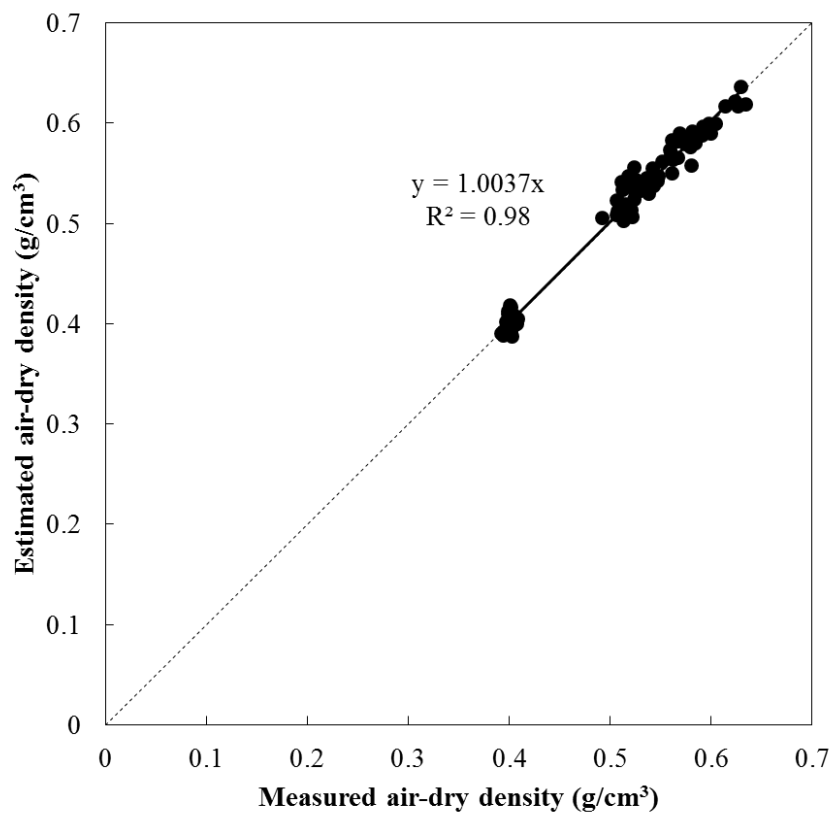
Figure 3-12 shows the comparison result between the measured air-dry density and the estimated air-dry density by using two different values of

apparent mass attenuation coefficients. Meanwhile, the accuracy of estimation of the air-dry density was high for all penetration depths. RMSEs for the accuracy of estimation of air-dry density of wood at 35 kV, 45 kV and 55 kV tube voltages were 0.0103 g/cm³, 0.0122 g/cm³, and 0.0075 g/cm³, respectively. In Appendix A, total results of air-dry density estimation using the function of apparent mass attenuation coefficient are presented.



(a) Using average of apparent mass attenuation coefficient; 0.3590

Figure 3-12. Estimation of air-dry density of wood with apparent mass attenuation coefficient of wood at 35 kV tube voltage (continue)



(b) Using variable apparent mass attenuation coefficients of wood according to penetration depth

Figure 3-12. Estimation of air-dry density of wood with apparent mass attenuation coefficient of wood at 35 kV tube voltage

3.5. Conclusion

Although X-ray tube radiates polychromatic X-ray, the attenuation characteristic of wood for the polychromatic X-ray was rarely studied. In this research, the effects of the species and penetration depth on the attenuation of polychromatic X-ray were investigated. The species did not have influence on the change of apparent mass attenuation coefficient. The values of the probability function of the polychromatic X-ray according to X-ray energy and the apparent mass attenuation coefficients were calculated by using the experimental values of initial and transmitted X-ray energy and Equation 3-8. The integral values and the apparent mass attenuation coefficients were not constant values, but varied with the penetration depth. The apparent mass attenuation coefficients decreased as the penetration depth increased. This phenomenon was thought to be caused by the beam hardening effect of the radiation, that is, the low energy part is more severely attenuated than the high energy part in polychromatic X-ray. Regression coefficients for the relations between those values and the penetration depth were determined at three tube voltages (35 kV, 45 kV and 55 kV), and used to estimate the air-dry densities of the wood specimens. The accuracy estimation was pretty good. The RMSEs of 35 kV, 45 kV and 55 kV for evaluating the estimation accuracy of air-dry density were 0.0103 g/cm^3 , 0.0122 g/cm^3 , and 0.0075 g/cm^3 , respectively.

Chapter 4

Computed Tomography (CT) for Measuring
Air-dry Density

4.1. Introduction

In previous chapter, a projection from single X-ray energy was used to estimate measure an air-dry density of wood, and the accuracy of those methods was high. If the method is employed to investigate the density of clear wood or engineered wood, it might be of help to the field of wood science or wood industry. However, it should be remembered that the results from the method was averaged value of air-dry density along X-ray penetration path. Therefore, it is difficult to provide the location of defect or deterioration in wood by using single projection, in which a superposition must be observed due to overlapping structure.

Computed tomography (CT) is a method to reconstruct the cross sectional image of an object from either transmission or reflection data collected by illuminating the object from many different directions (Kak and Slaney, 1988). Eliminating the superposition, the information what you want to investigate can be easily found in the reconstructed image. Numerous researches about CT have been studies in various fields including wood science (Fredriksson, 2015; Lindgren et al., 1992; Rojas et al., 2007; Sepúlveda et al., 2002). The results of CT in wood science were used to determine the physical properties in radial, tangential and longitudinal direction or to increase the projection yield of engineering wood.

Despite the advantages of CT, it is difficult to be used in the field where structures or trees are located. The equipment of CT is more suitable for laboratory tests, and radiation shields have to be installed to prevent an inspector from hazardous radiation. Thus, the first step in solving the field applicability problem was using low X-ray energy with portable X-ray apparatus (Kim et al., 2014). The X-ray energy is having lower energy compared with industrial and medical purpose and it has broad wavelength. In

previous chapter, low polychromatic X-ray energy was also used. If low energy X-ray were used, the risk of radiation exposure can be reduced as the inspector positions with sufficient distance from the X-ray source. In this study, therefore, the method of reconstructing CT image for applying in the field was developed considering the characteristic of polychromatic X-ray with low energy. Post processing to detect deterioration in wood was also studied.

4.2. CT image reconstruction algorithm

In this study, fan beam shape source and flat panel detector were used to take projections. The fan beam indicates a point source of radiation with fan-shape beam. The system having the fan beam and flat panel detector is much faster way to generate the line integrals as shown in Figure 4-1 (Kak and Slaney, 1988). The line integrals were denoted by using $R_{\beta}(s)$. With the system, numerous projections can be collected from many different directions to reconstruct CT image. The cross section information of absorber can be obtained by using the result of reconstructed CT image. The cross section information was shown in Figure 4-3 as $f(r, \phi)$.

Feldkamp et al. (1984) studied about fan-beam CT algorithm by using the Radon transform for two dimensions in the form of a convolution and back projection. As follow, the algorithm used in this study is introduced shortly. $R_{\beta}(s)$ is projection in Figure 4-2, where s is the distance along the straight line corresponding to the detector plane. The detector plane (D_1D_2), for theoretical purpose, is assumed the existence of an imaginary detector plane ($D'_1D'_2$). Thus, the projection $R_{\beta}(s)$ is associated with point A on $D'_1D'_2$.

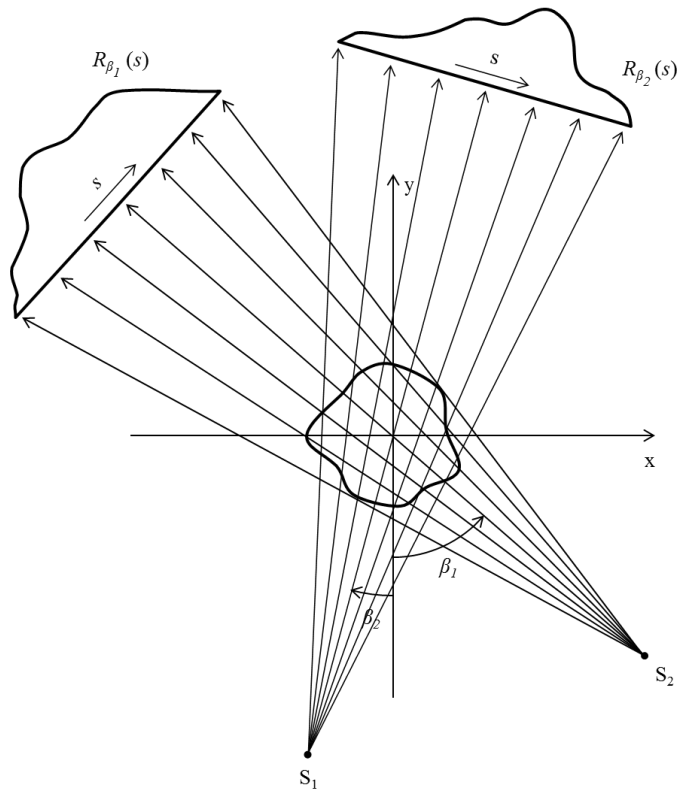


Figure 4-1. Fan beam projection
(Revised image from Rosenfeld and Kak, 2014)

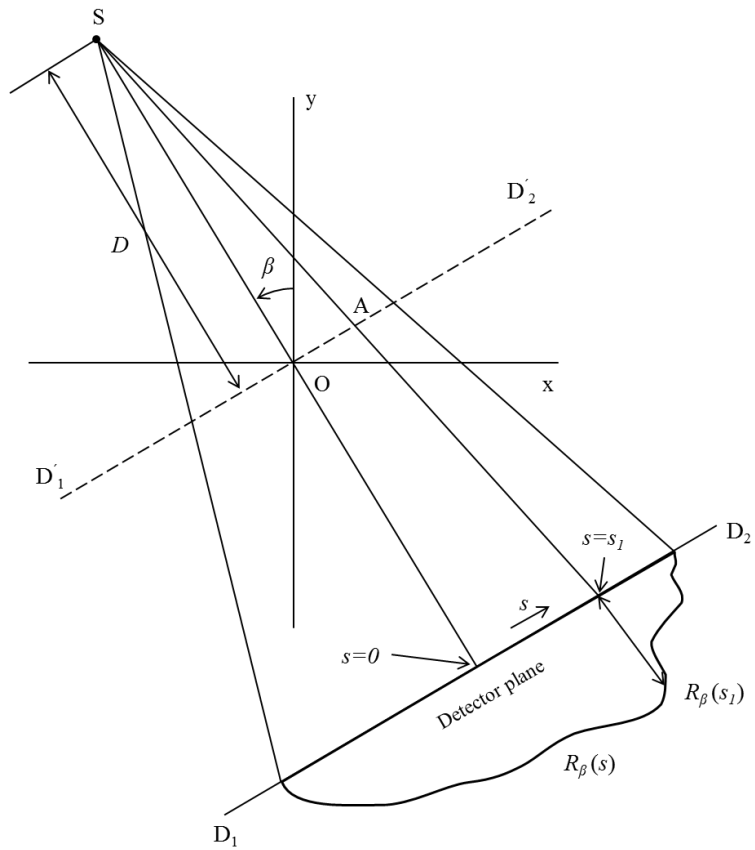


Figure 4-2. Geometry of detector plane in fan beam CT system
(Revised image from Rosenfeld and Kak, 2014)

If parallel projection data was under consideration, the ray SA would contain a parallel projection $p(t, \theta)$ with t and θ as shown in Figure 4-3. The distance t from the origin O to the ray SA is related to s . And the angle θ from x axis is given by,

$$t = sD / \sqrt{D^2 + S^2} = s \cos \gamma \quad (4-1)$$

$$\theta = \beta + \gamma \quad (4-2)$$

where, $\gamma = \tan^{-1}(s/D)$.

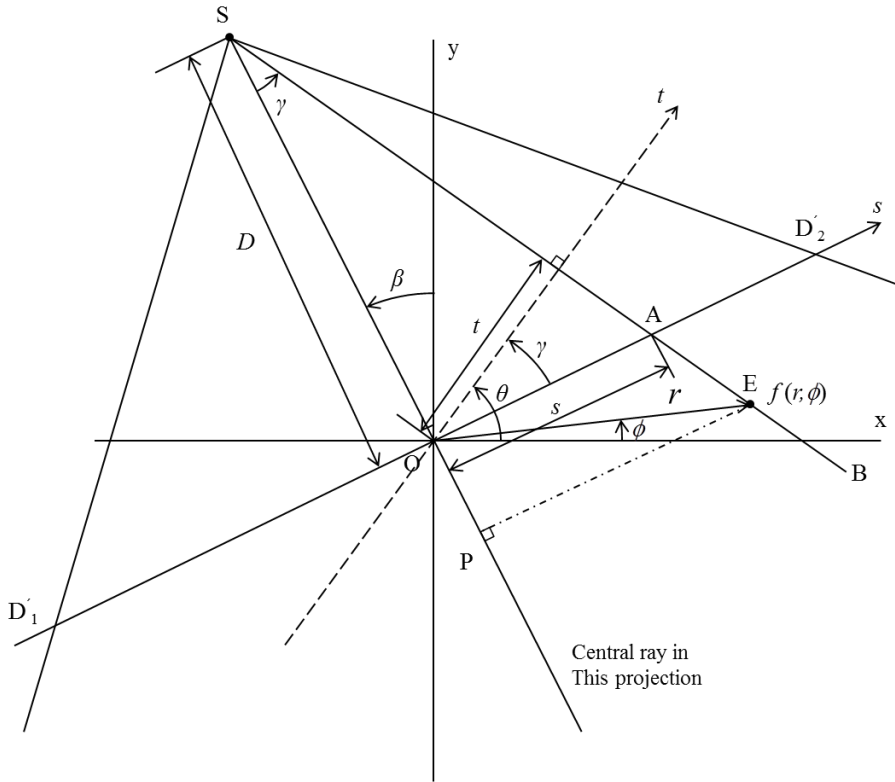


Figure 4-3. Geometry for derivation of the fan beam CT algorithm
(Revised image from Rosenfeld and Kak, 2014)

The value of projection $f(r, \phi)$ can be expressed in terms of the parallel projection data as follows,

$$f(r, \phi) = \frac{1}{2} \int_0^{2\pi} \int_{-t_m}^{t_m} p(t, \theta) h(r \cos(\theta - \phi) - t) dt d\theta \quad (4-3)$$

With the delta function, $f(r, \phi)$ vanishes if r is larger than D ,

$$p(t, \theta) = \begin{cases} R_\beta(s), & |t| < D \\ 0, & |t| > D \end{cases} \quad (4-4)$$

Using Equation 4-1 and 4-2, the transform is applied to change from parallel beam data $p(t, \theta)$ to fan beam data $R_\beta(s)$ as follows,

$$f(r, \phi) = \frac{1}{2} \int_{-\gamma}^{2\pi-\gamma} \int_{-s_m}^{s_m} P_{\beta+\gamma}(s \cos \gamma) h\left(r \cos(\beta + \gamma - \phi) - \frac{D^3}{\sqrt{D^2 + s^2}}\right) \frac{D^3}{(D^2 + s^2)^{3/2}} ds d\beta \quad (4-5)$$

where, $dt d\theta = \frac{D^3}{(D^2 + s^2)^{3/2}} ds d\beta$.

$P_{\beta+\gamma}(s \cos \gamma)$, which is the ray integral along SA in the parallel projection data, is simply $R_\beta(s)$. Thus,

$$f(r, \phi) = \frac{1}{2} \int_0^{2\pi} \int_{-s_m}^{s_m} R_\beta h\left(r \cos(\beta + \gamma - \phi) - \frac{D^3}{\sqrt{D^2 + s^2}}\right) \frac{D^3}{(D^2 + s^2)^{3/2}} ds d\beta \quad (4-6)$$

A reconstruction formula (4-6) was obtained, and the formula can be rewritten considering the geometry of CT and convolving kernel h as follows,

$$f(r, \phi) = \frac{1}{2} \int_0^{2\pi} \frac{1}{U^2} \left(\int_{-\infty}^{\infty} R_{\beta}(s) g(s' - s) \frac{D}{\sqrt{D^2 + S^2}} ds \right) d\beta \quad (4-7)$$

where, $U = \frac{\overline{SO} + \overline{OP}}{D}$ and $g(s) = \frac{1}{2} h(s)$. This filtered back projection reconstruction equation was used to reconstruct CT image in this study.

4.3. Materials and experimental methods

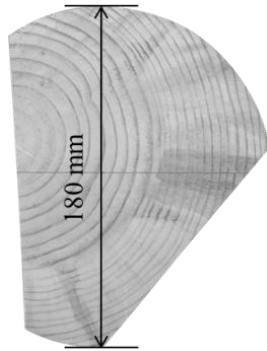
4.3.1. Materials

Two sets of specimens were prepared in this study; the first set was prepared for determining the apparent mass attenuation coefficient according to penetration depth, and the second set was used to validate the accuracy of CT reconstruction.

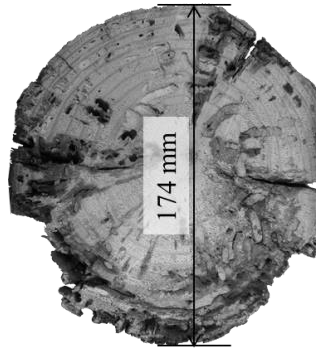
For determining the apparent mass attenuation coefficient according to penetration depth, ten clear woods for three different wood species were prepared; Korean pine (*Pinus koraiensis*), pine (*Pinus densiflora*) and larch (*Larix leptolepis*). The thickness of specimen, which is same size of penetration depth, was 20 mm. All of the specimens were air dried condition, and the average of moisture content was 9.07%.

For the second test setup, wood having irregular shape and wood member dismantled from traditional wood building were used as specimens to validate the accuracy of reconstructed CT image. The condition of those specimens was also air dried, and the species of that was pine. The dismantled wood member had been deteriorated by insect when it was investigated by visual inspection.

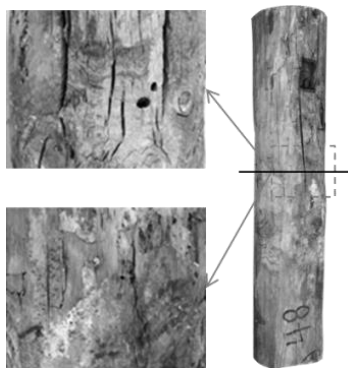
Figure 4-4 shows information of specimens for the test. The longest diameter of irregular shaped wood and wood member was 180 mm and 174 mm, respectively. At surface of wood member, some traces of deterioration by insect were found. The black solid line in Figure 4-4c indicates the location where CT image was reconstructed.



(a) Irregular cross section



(b) Cross section of wood member



(c) Trace of insect deterioration

Figure 4-4. Specimen for the test

4.3.2. CT apparatus

The CT apparatus used in this study consists of X-ray tube, digital detector and CT gantry. The X-ray tube K-4 (Softex, Japan) with the maximum tube voltage and current of 64 kV was used to radiate X-ray in condition of 35 kV tube voltage and 5 mA tube current. The detector EVS 4343 (DRtech., Korea) composed of Cesium scintillator was also applied to obtain projections by exposing it X-ray during 2 seconds. The CT gantry, which is equipment to rotate the X-ray tube and detector at a rotation angle per one projection, was used to gain projections for reconstructing CT image. It was self-development equipment, and the minimum angular interval is 0.1 degrees.

With the same method in chapter 3, projections of clear woods were taken according to the number of wood blocks. The longest penetration depth was 200 mm. Equation 3-7 was also used to calculate the apparent mass attenuation coefficient, and then the relationship between the apparent mass attenuation coefficient of wood and penetration depth was also investigated.

Figure 4-5 shows schematic drawing and picture of CT apparatus to gain projections for reconstructing CT image. The distance between X-ray tube and detector was maintained as 1197.92 mm. While, the distance between X-ray tube and center of rotation of X-ray tube and detector was 950 mm. The 360 projections were taken as the X-ray tube and detector were rotated 1 degree at a time for the irregular shaped wood and dismantled wood member. Those projections were used to reconstruct CT image.

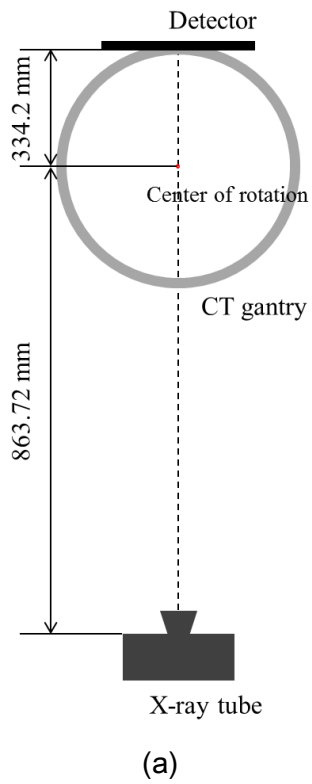


Figure 4-5. Schematic drawing and picture of CT apparatus

4.3.3. Modification of CT image reconstruction algorithm

The filtered back projection introduced in previous section was used to reconstruct CT image with fan X-ray beam and flat panel detector. Figure 4-6 shows the flow chart of the filtered back projection algorithm for reconstructing CT image. Reconstructed CT image was quantitatively evaluated by using the Hounsfield scale. The scale is defined in Hounsfield units (HU), running from air at -1000 HU, through water at 0 HU, and up to dense material at +1000 HU (Gunderman, 2006). However, Boris et al. (1987) reported that it is difficult to correlate CT Hounsfield unit numbers from one CT investigation to another and from one CT scanner to another. To solve the problem, the phantom was used for performance evaluation and quality assurance (Judy et al., 1977).

Despite the effort, there is still problem when CT was applied at the field. Because the geometry of CT apparatus for field application could be changed frequently, while the geometry of CT scanner in laboratory is fixed for the expected life span of the scanner. Therefore, alternative method for evaluating of CT image was developed. Based on the change of apparent mass attenuation coefficient according to penetration depth, the projections generated before reconstruction processing were converted to density profiles. And then, the density profiles were used to reconstruct quantified density CT image. Figure 4-7 shows the flow chart for the modified method to reconstruct CT image. As mentioned above, projections were converted to density profile just before doing reconstruction processing. There was no employment of Hounsfield scale. From the procedure, 512×512 pixel quantified CT images were obtained.

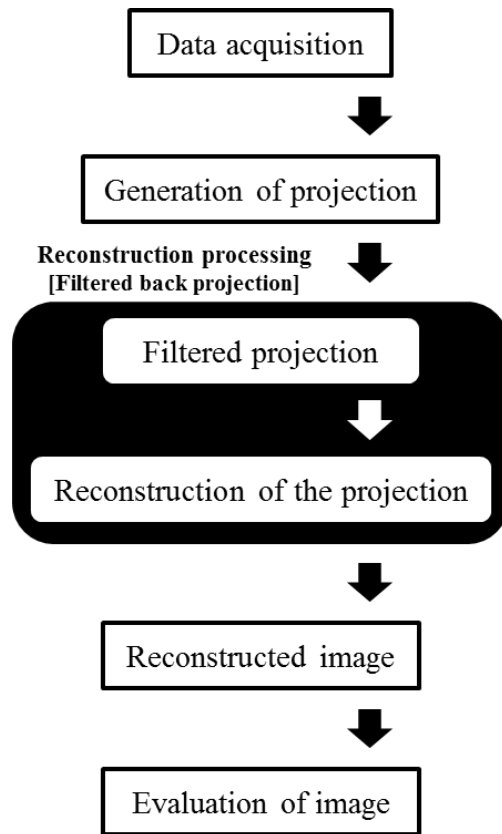


Figure 4-6. Flow chart of CT image reconstruction

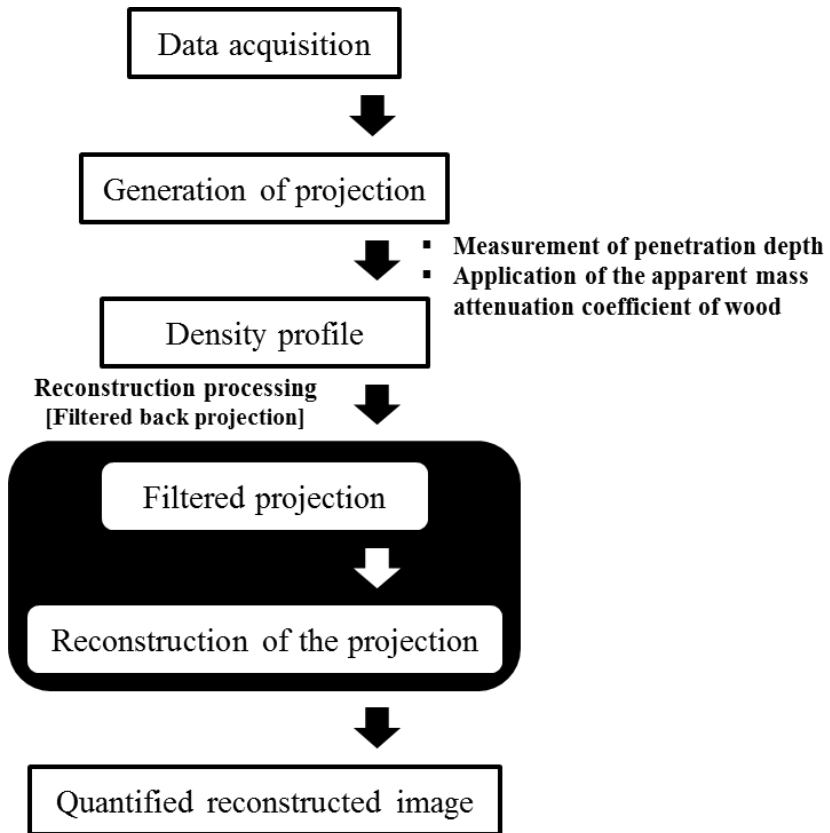
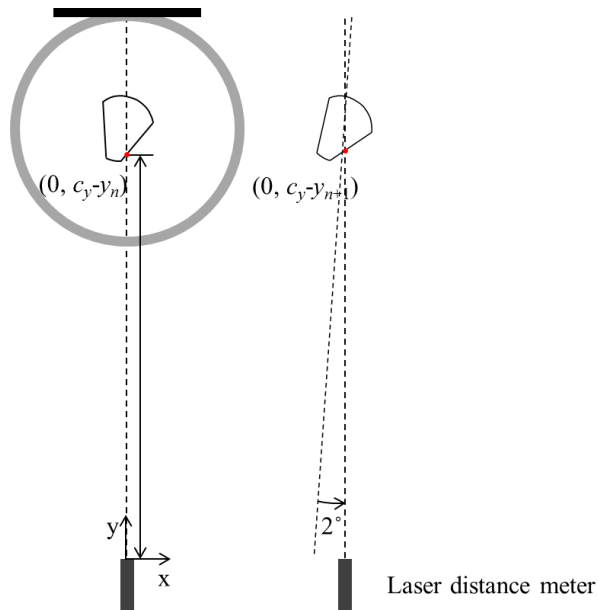


Figure 4-7. Modified flow chart for reconstructing CT image

To convert projections to density profiles, the absorber shape should be measured for calculating penetration depths. Simple method by using the laser distance meter was imposed on the measurement of the cross sectional shape. The laser distance meter was Disto D3aBT (Leica, USA) having the error of measurement of ± 1 mm. Figure 4-8 shows the procedure of the measurement: firstly, the least distance between the X-ray tube and the surface of specimen rotating the laser distance meter every 2 degrees were measured (a); secondly, the 180 distances were placed as 180 points in the geometry of CT by using rotational transform (b); lastly, the cross sectional shape could be made of liner interpolation between n th and $(n+1)$ th point (c). From the procedure, the coordinates of cross section of specimen were obtained in x-y plane. Using the coordinates and geometry of CT apparatus, penetration depths were calculated at pixel of detector as shown in Figure 4-9.



$n = n^{\text{th}}$ rotation (from 1 to 180)

$$\begin{pmatrix} 0 & c_y - y_1 \\ 0 & c_y - y_2 \\ \vdots & \vdots \\ 0 & c_y - y_{180} \end{pmatrix} \cdot \begin{pmatrix} \cos\left(-\frac{2n}{180}\right) & -\sin\left(-\frac{2n}{180}\right) \\ \sin\left(-\frac{2n}{180}\right) & \cos\left(-\frac{2n}{180}\right) \end{pmatrix} = \begin{pmatrix} x'_1 & y'_1 \\ x'_2 & y'_2 \\ \vdots & \vdots \\ x'_{180} & y'_{180} \end{pmatrix}$$

Rotation transform

(b)

Figure 4-8. Measurement of cross section of specimen with lager distance meter, c_y is the distance between x-ray tube and center of rotation (continue)

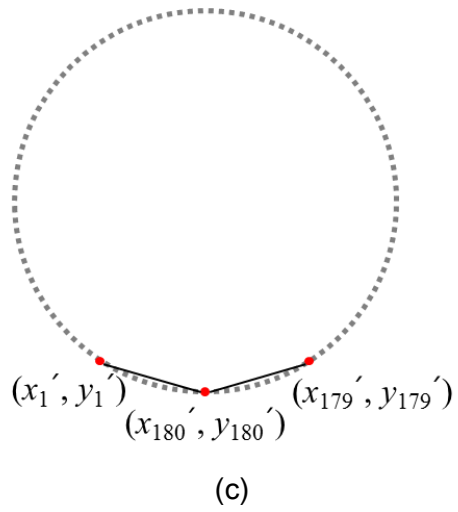


Figure 4-8. Measurement of cross section of specimen with lager distance meter, c_y is the distance between x-ray tube and center of rotation

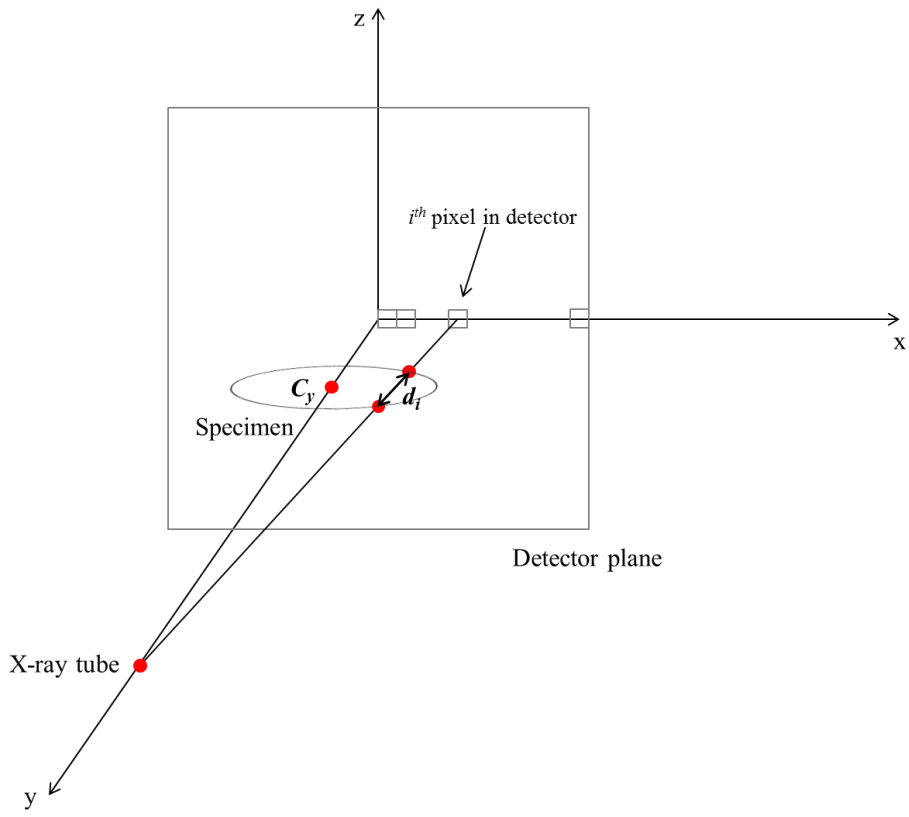


Figure 4-9. Penetration depth according to location of pixel in detector. d_i indicates the penetration depth in specimen when X-ray arrives at i th pixel of detector

To find the factor influenced on the accuracy of modified method, the 360 projections were converted into three sets of density profiles by using a constant apparent mass attenuation coefficient and relationship between apparent mass attenuation coefficient and penetration depth. Also, two kinds of penetration depth were used when the constant apparent mass attenuation coefficient was used: one was the measured penetration depth with laser distance meter; other was the estimated penetration depth from assumption that the specimen was round wood.

The optimum CT condition related with the number of projection was also found. In this study, the optimum CT condition means the least number of projections to reconstruct quantified CT image. If the number of projection decreased, it takes less time to reconstruct CT image. The 360 projections of irregular shaped wood and wood member were used to find the optimum CT condition. Because the 360 projections were taken by using 1 degree angular interval, various angular intervals can be chosen from 1 degree to 360 degrees. Among the various angular intervals, five angular intervals from 1 degree to 5 degrees were used.

To verify the results, the irregular shaped wood was cut into small specimen as shown in Figure 4-10. The air-dry density of small specimens was evaluated by using the dimensional method. They were compared with values in each CT image value. Table 4-1 shows the air-dry density.

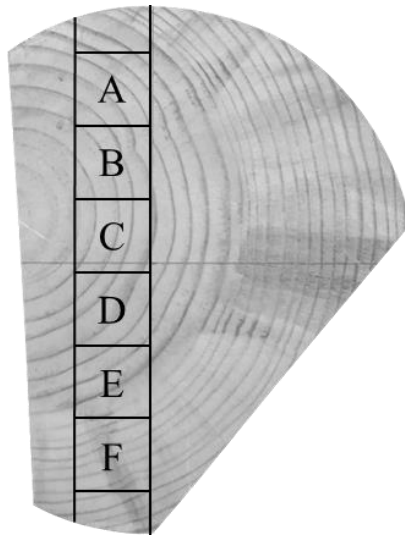


Figure 4-10. Location of small specimens to measure air dry density

Table 4-1. Air-dry density of small specimens measured dimensional method

Location	Air-dry density (g/cm ³)
A	0.455
B	0.459
C	0.420
D	0.467
E	0.445
F	0.470

Post processing for CT image help to remove artifact occurred during scanning (Tuy, 1993) or to find defects more clearly. In this study, binary imaging was made an attempt to detect deterioration as post processing. It is converting CT image into a digital image having only two colors (black and white) using a threshold value as follows,

$$f(x,y) = \begin{cases} f(x,y) = 1 & \text{if } f(x,y) > t \\ f(x,y) = 0 & \text{if } f(x,y) < t \end{cases} \quad (4-8)$$

where, $f(x,y)$ is the gray scale value at (x, y) and t is threshold value of gray scale. The threshold value was established from the results of CT image.

4.4. Results and discussion

4.4.1. Accuracy of estimation of air-dry density with modified CT image reconstruction algorithm,

Figure 4-11 shows change of apparent mass attenuation coefficient of wood according to penetration depth. In previous study, the relationship between mass attenuation coefficient of wood and penetration depth was revealed in 20 mm, 40 mm, 60 mm and 80 mm penetration depths. As a results with 35 kV tube voltage, the equation of the relationship obtained was $\mu=0.5414\exp(-0.073t)$, where μ is the apparent mass attenuation coefficient of wood, and t is penetration depth. Estimated value by using the relationship is presented as solid line in Figure 4-11. The measured values were gained from the experiment by using clear woods having thickness from 20 mm to 200 mm. Although the some estimated values were determined by extrapolation from the relationship, the measured value coincided with the estimated valued. The RMSE between two values was $0.00062 \text{ cm}^2/\text{g}$, so the equation of the relationship was used once again.

Figure 4-12 shows measurement result of cross section of irregular shape specimen. When the X-ray arrives at 1536th and 2813th pixel from the left of detector, penetration depths (d_1 and d_2) are also presented in Figure 4-12. The actual length of d_1 and d_2 were 16.55 cm and 6.35 cm, respectively. Compared with actual measurement for each penetration depth, the accuracy of estimated penetration depth was high.

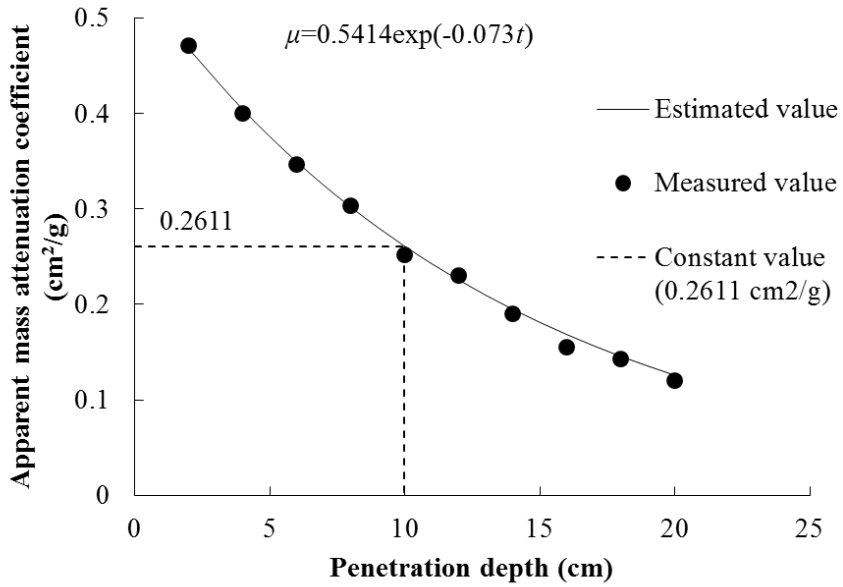


Figure 4-11. Apparent mass attenuation coefficient at various penetration depths

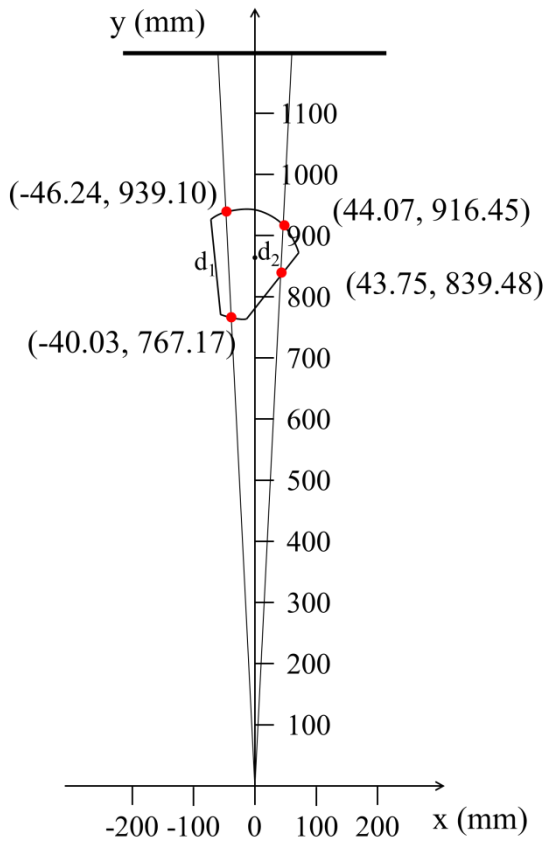
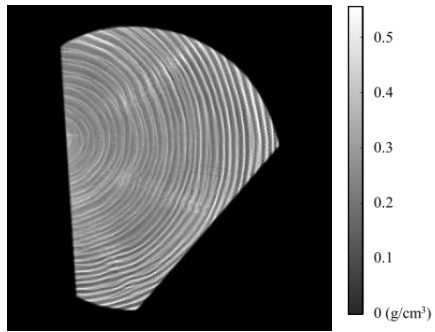


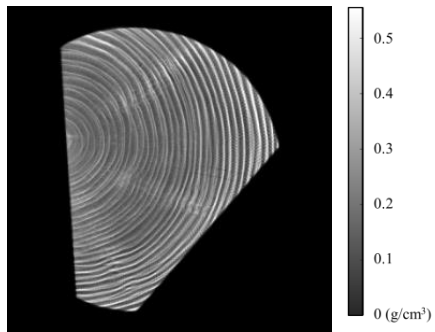
Figure 4-12. Cross section of irregular shape specimen and measured penetration depth

Three kinds of reconstructed CT image were presented to confirm the accuracy of modified CT image in Figure 4-13; (a) the reconstructed CT image by using relationship between apparent mass attenuation coefficient and measured penetration depth, (b) the reconstructed CT image by using the constant mass attenuation coefficient ($0.2611 \text{ cm}^2/\text{g}$) and measured penetration depth, and (c) the CT image with the constant mass attenuation coefficient and penetration depth estimated from the assumption that the specimen was round wood. Here, measured penetration depth indicated the depth measured with laser distance meter as shown Figure 4-12.

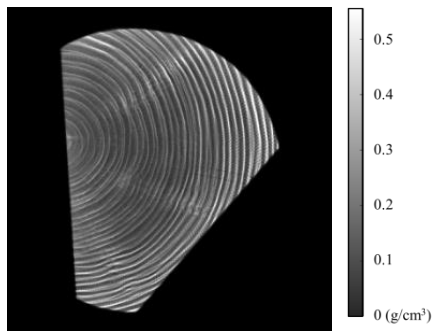
Excepting the reconstructed CT image of Figure 4-13a, the results for center of specimen was lower than edge of that. Results of Figure 4-13b and 4-13c were not considered the change of mass attenuation coefficient according to penetration depth. Therefore, the center of specimen seemed to be underestimated because the penetration depth passing the center of specimen usually has longer penetration depth. On the other hand, the CT image in Figure 4-13c indicated that the difference of results in CT image was the largest between center and edge of specimen. It was considered that that phenomenon occurred due to beam hardening.



(a)



(b)



(c)

Figure 4-13. Three kinds of reconstructed CT image; (a) relationship between apparent mass attenuation coefficient and measured penetration depth, (b) average apparent mass attenuation coefficient and measured penetration depth, (c) average apparent mass attenuation coefficient and estimated penetration depth

The air-dry density of small specimens was compared with the average value of each CT image. Those average values correlated with the air-dry density because density profiles were used to reconstruct CT image with modified method. Figure 4-14 shows comparison of air-dry density between dimension method and CT image. When the constant apparent mass attenuation coefficient of wood was used, it could be found that relative center parts of specimen were underestimated. The constant apparent mass attenuation coefficient of wood, $0.2611 \text{ cm}^2/\text{g}$, was similar when X-ray penetrates wood with 100 mm thickness as shown in Figure 4-11. Therefore, it was expected that underestimated part would be found when the penetration depth in wood longer than 100 mm.

In reconstructed CT image with modified method, the error of air-dry density was lowest when density profiles were converted by using the relationship between apparent mass attenuation coefficient and measured penetration depth. The lowest RMSE of air-dry density for small specimens was 0.009 g/cm^3 . It was considered that beam hardening of polychromatic X-ray reduced as the change of apparent mass attenuation coefficient of wood was contemplated at various penetration depths.

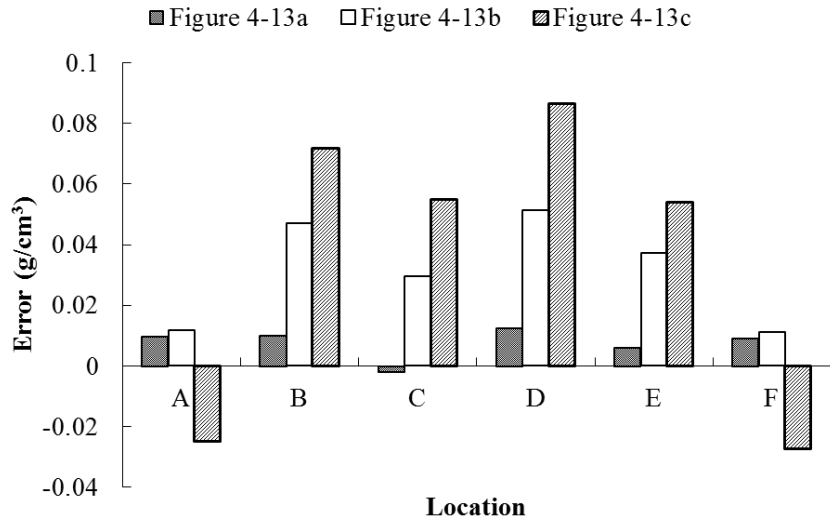
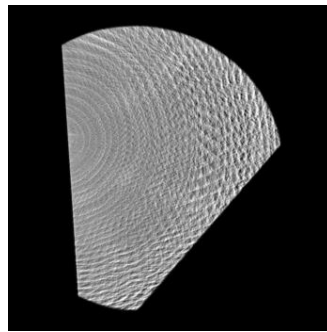


Figure 4-14. Comparison of air-dry density between dimensional method and CT image. Error of air-dry density is difference between dimension method and CT image

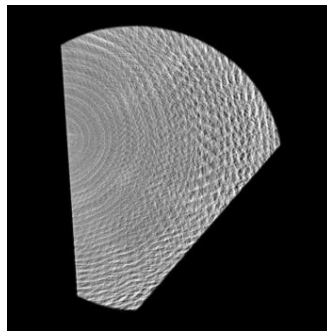
4.4.2. Optimum condition to reconstruct density CT image

Figure 4-15 shows the results of CT image according to number of projections. There is no doubt the quality of CT image increased as more projections were used. Especially, the number of projection was more influence on the image quality in edge of specimen than in center of that. An elapsed time to finish inspection by using CT correlated with time to obtain whole number of projections. For inspection of artificial hole in wood, required number of radiographs for reconstructing CT image was studied (Kim et al., 2013; Kim et al., 2006b). Kim et al. (2006b) reported that the artificial hole in wood could be detected by using only 9 projections with 20 degrees rotation angular from 0 degrees to 160 degrees. On the other hand, 72 projections gained from digital detector were required to detect artificial hole, which was located in the edge of specimen (Kim et al., 2013).

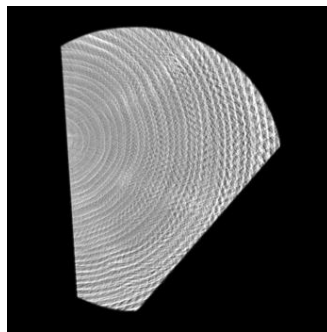
In this study, rotation angular from 1 degree to 5 degrees was used to gain projections. At that time, the number of projections was 360, 180, 120, 90, and 72, respectively. It was considered that more projections would be needed to reveal density distribution of wood by using reconstruct CT image when compared with detecting artificial hole. Moreover, the insect damage such as termite damage is occurred in early wood (Oh et al., 2015). Therefore, reconstructed CT image have to obtain high resolution to distinguish early wood from cross sectional image. In view of the facts, the least number of projections were found. At least 180 projections were needed to reconstruct CT image compared to actual cross section image.



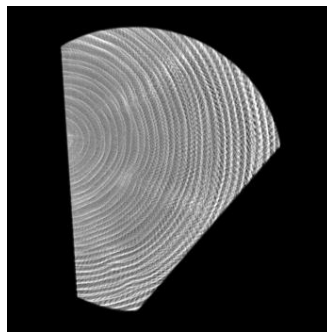
(a) 72 projections



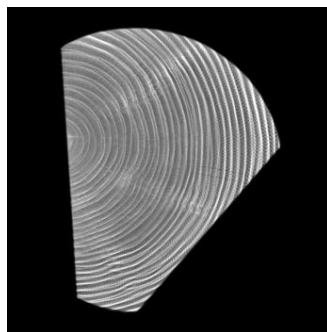
(b) 90 projections



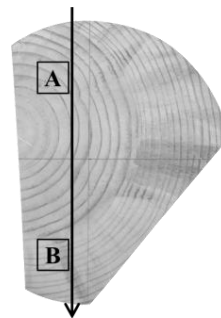
(c) 120 projections



(d) 180 projections



(e) 360 projections



(f) Specimen

Figure 4-15. CT image according to the number of projection and actual picture of specimen

Figure 4-16 shows the average air-dry density according to the number of projection to reconstruct CT image. A and B indicates the location for calculating the average air-dry density, and they are shown in Figure 4-15f. As the number of projections increased, the average air-dry density decreased. And then, the air-dry density leveled off after 180 projections. Compared with actual air-dry density of small specimens, the error between results of CT image and actual air-dry density was quite small when 180 projection or 360 projections was used to reconstruct CT image.

Figure 4-17 presents the profile correlated with the line, which is shown in Figure 4-15f. Figure 4-17 includes three different lines; dashed line, solid line and dotted line. The dashed line indicates the profile calculated from the result of CT image using 360 projections, while the solid line is the profile came from the results of CT image using 180 projections. And the error profile, dotted line, is the different between the results of CT image using 360 projections and 180 projections. When 180 projections were used to reconstruct CT image, the CT image overestimated air-dry density of specimens. However, the average error between two CT images was only 0.035 g/cm^3 . Moreover, it was a coincidence of profile shape between dashed line and solid line for whole location. In this study, CT apparatus take 12 seconds to gain a projection. Therefore, acquirement of 360 projections to reconstruct CT image takes approximately 30 additional minutes compared with the time to take 180 projections. Considering the results of CT image and time, it was reasonable to choose 180 projections for reconstructing CT image for this modified method.

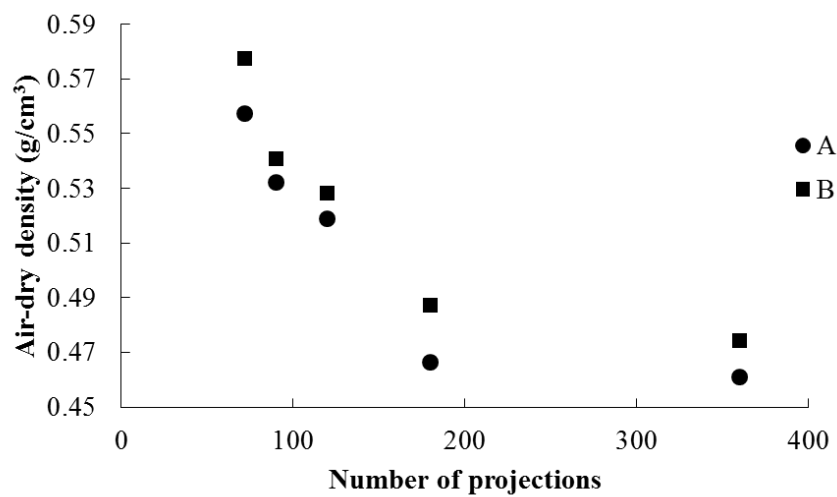


Figure 4-16. Change of air-dry density in CT image with number of projections

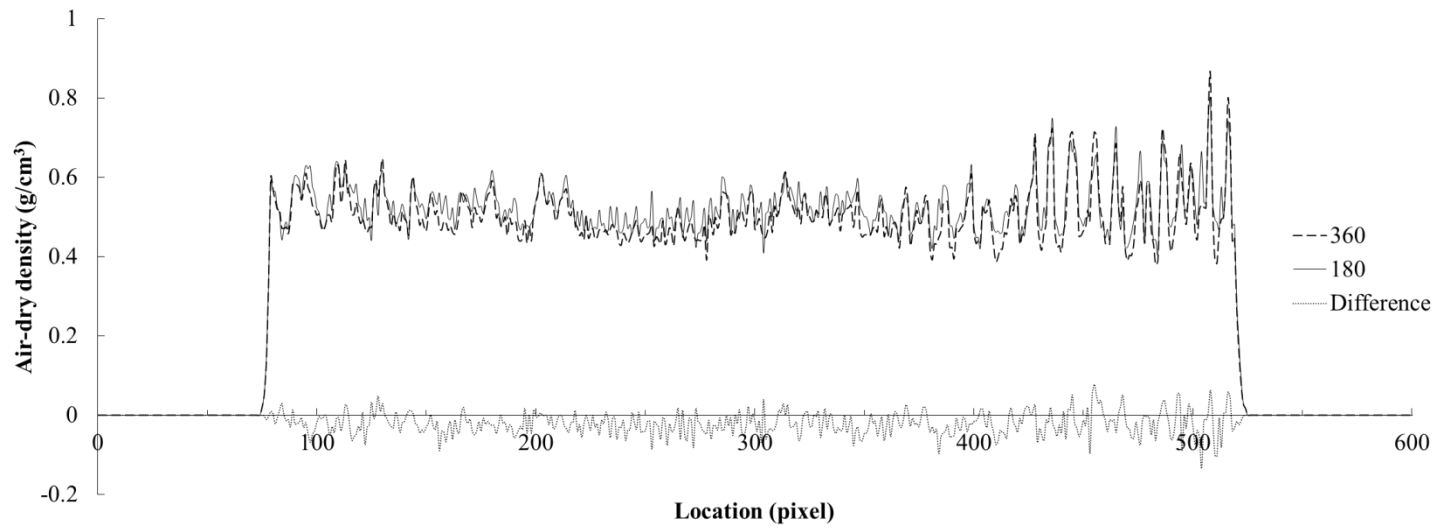
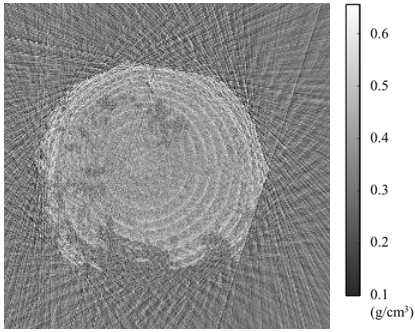


Figure 4-17. Profile along with line as shown in Figure 4-15f

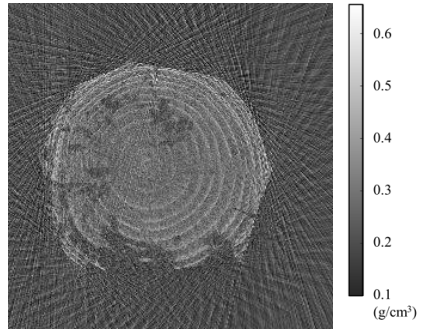
4.4.3. Evaluation of deteriorated wood with density CT image

Figure 4-18 shows the reconstructed CT images with 72, 90, 120, 180 and 360 projections for wood member. When the number of 72 and 90 projections were used to reconstructed CT image, overall shape of specimen and hardly deteriorated part could be detected. However, the location of pith cannot be determined. Moreover, air-dry density in all cross section was overestimated even though there was deterioration. This is because of filtered back projection algorithm for reconstructing CT image. The results of irregular shape wood and wood member coincided.

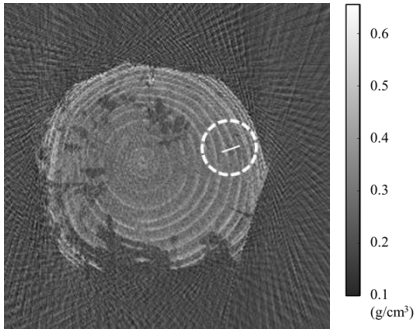
Figure 4-19 shows the density profile of the reconstructed CT images with 120, 180 and 360 projection. The location of the density profile was white solid line in dotted circle as shown in Figure 4-18. It seemed that there was no difference between the reconstructed CT images with 120 and 180 projections when they were visually checked. However, distinction of air-dry density measured in CT image was occurred. CT image reconstructed by using 120 projections still overestimated air-dry density. From those results, it was confirmed that the optimum number of projection was 180 to investigate wood by using modified CT image. The diameter of the smallest hole detected by using CT image was 1.5 mm. The resolution of CT image was higher than other nondestructive testing method. Acoustic tomography, which is usually used to investigate inner state of wood, has 25 mm (Divos and Divos, 2005).



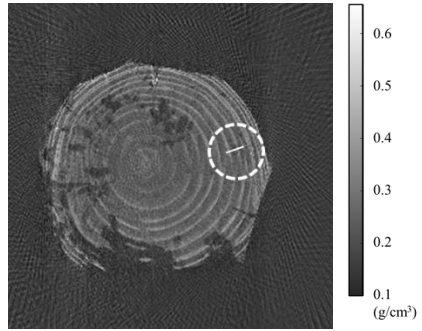
(a) 72 projections



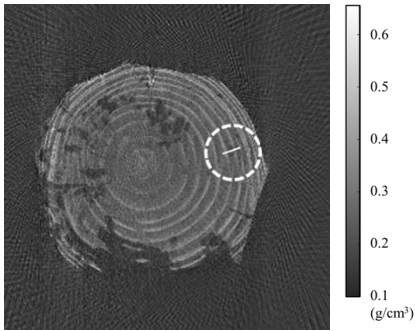
(b) 90 projections



(c) 120 projections



(d) 180 projections



(e) 360 projections



(f) Actual cross section

Figure 4-18. Reconstructed CT image with various number of projections

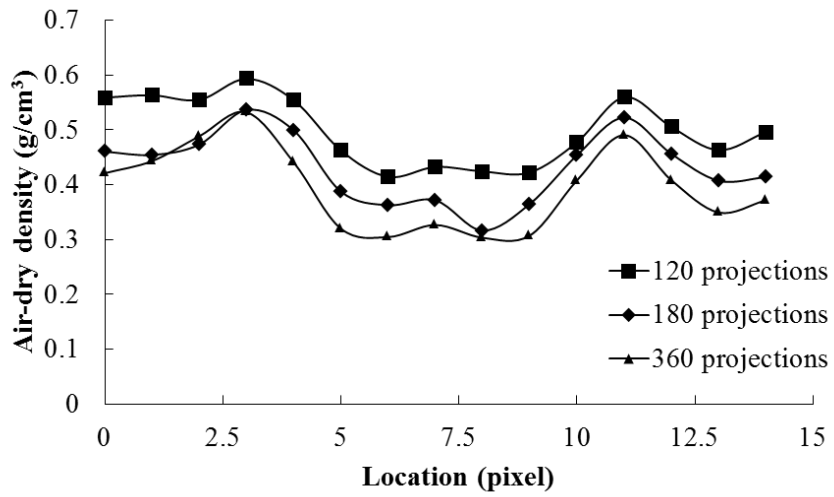
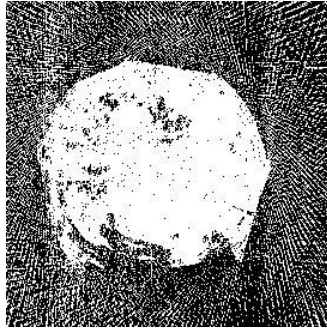


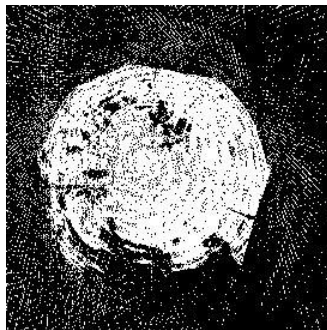
Figure 4-19. Density profile for solid line in Figure 4-18

It was considered that the deteriorations caused by the Beetle. The reason is as follows; the borings were found in surface of wood member and some deterioration occurred crossing from early wood to late wood. Blanchette (1998) insisted that the boring in wood surface was evidence of deterioration by the Beetle. Moreover, woody powders were found in the deteriorations when the wood member had been cut. In CT image, some deterioration filled with woody powder could not be detected. It seemed that woody powder has same attenuation characteristic or similar density with air-dry density of sound wood. However, we can conjecture about the existence of the deterioration where discontinuous of annual ring with the knowledge of trace of insect damage at surface and ankertrass of each insect.

Figure 4-20 shows the binary CT image after applying post processing. The possibility of binary CT image was suggested for separating low density part and high density part. The threshold for binary post processing was 0.420 g/cm^3 , 0.388 g/cm^3 and 0.341 g/cm^3 . Compared with the actual cross section of wood member, the binary CT image with threshold of 0.388 g/cm^3 had high accuracy. The threshold was 80.7% of air-dry density of sound wood measured in CT image. However, the criteria to establish threshold or other method to find early stage of deterioration should be studied in further study. It is important to find early stage of deterioration because 10% weight loss of sound wood reduced mechanical properties of wood rapidly (Lee et al., 2005).



(a) Threshold: 0.420 g/cm³



(b) Threshold: 0.388 g/cm³



(b) Threshold: 0.341 g/cm³

Figure 4-20. Binary CT image

4.5. Conclusion

To find density distribution or location of deterioration, numerous projections were collected by using CT apparatus and were used to reconstruct CT image. Those projections were used to reconstruct density CT image. To gain quantified CT image, the projections were converted to density profiles with the relationship between apparent mass attenuation coefficient and penetration depth. The equation of the relationship was $\mu=0.5414\exp(-0.073t)$ in condition of 35 kV tube voltage. And the penetration depth was measured by using the laser meter with high accuracy. From the results of CT images with various numbers of projections, it was determined that 180 projections were needed to make density CT image at least. To verify the accuracy of the modified reconstruction method, deteriorated wood member was investigated by using the method. Compared with the actual cross section of the wood member, the CT image could detect location of pith, annual ring, crack and hole made by insect successfully. Moreover, binary imaging processing for CT image made it easy to detect insect damage and low density part. The threshold of 80.7% of air-dry density of sound wood indicated high accuracy to find inset damage and low density part. However, the deterioration with wood powders was hard to detect by using CT image. Therefore, the research considering the trace of insect damage at surface of wood and ankertrass of each insect is needed to detect that deterioration.

Chapter 5

Tomosynthesis for Investigating of Inner State
of Wood

5.1. Introduction

In previous study, reconstructed method to make CT image was introduced. When the reconstruction method is applied to historic properties, its result can provide density profile or existence of deterioration without demolishing wood structure. In terms of conserving the historic building, reconstructed CT image is the best way if CT could be applied. However, if historic building has wall between columns, it is difficult to secure the space to rotate CT apparatus for acquiring projections. Therefore, different nondestructive testing and evaluation is needed to overcome the limitations of CT.

With the development of radiation measurement technology, the tomosynthesis has been recently introduced in medical field (Andersson et al., 2008; Ciatto et al., 2013; Dobbins III and Godfrey, 2003). It can reconstruct an arbitrary cross section using few numbers of projections from the limited angle along single-acquisition sequence (Dobbins III and Godfrey, 2003). Because the method can reconstruct the arbitrary cross section (coronal section) by using the limited rotation angle, it was considered that the tomosynthesis could be alternative method to investigate wood which have an obstacle to apply CT apparatus. However, the tomosynthesis is never studied in wood science to the best of authors' knowledge.

In this chapter, the feasibility of tomosynthesis was discussed to conduct it at wood. And the optimum condition of radiography was found by evaluating the reconstructed image quality in-focus plane and the quality of the vertical resolution. Lastly, the results applied to deteriorated wood member were presented.

5.2. Tomosynthesis reconstruction algorithm

CT reconstruction method was done to calculate cross sectional image, which is perpendicular to the rotation axis. On the other hand, tomosynthesis is a method to reconstruct an arbitrary cross section. The arbitrary cross section is referred as coronal cross section, which is parallel to the rotation axis as shown in Figure 5-1.

Dobbins III and Godfrey (2003) summarized tomosynthesis geometries which involve having either the X-ray tube or the X-ray tube and detector move in certain rotation angular about center of motion. There are three kinds of the geometries; completed isocentric motion, partial isocentric motion, and partial isocentric motion of Niklason et al. (1997). Among the geometries, completed isocentric motion was used in this study. As shown in Figure 5-2, it was easy to be applied by using CT apparatus. Moreover, the tomosynthesis algorithm to reconstruct the tomosynthesis image from the motion is similar to the filtered back projection algorithm for CT image (Badea et al., 2001).

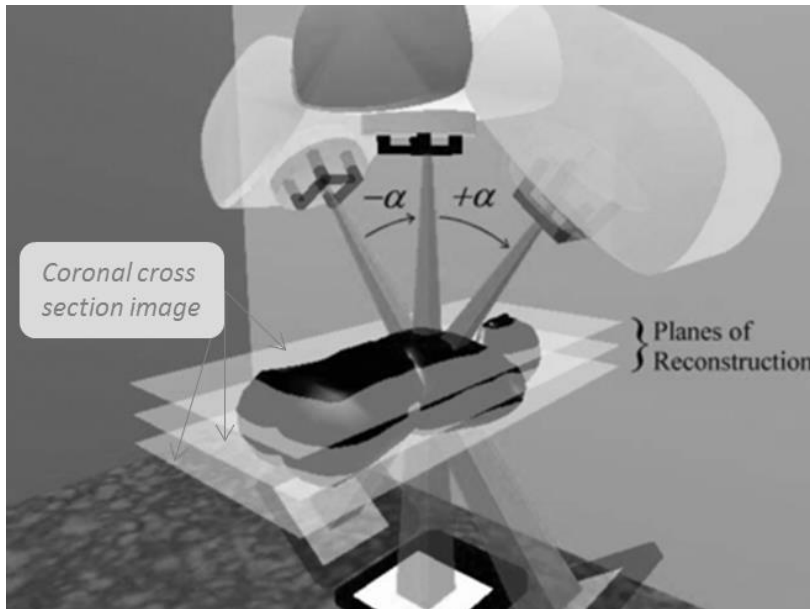


Figure 5-1. Coronal cross section in tomosynthesis
(Revised image from Pang et al., 2008)

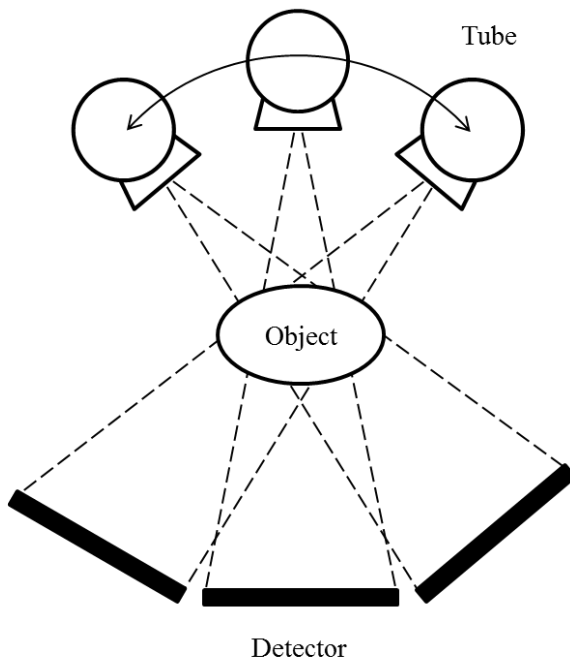


Figure 5-2. Complete isocentric motion for tomosynthesis

Based on the filtered back projection introduced in chapter 4, the pixel value of cone beam ($f(x, y, z)$) is given as follow (Badea, 2000),

$$f(x, y, z) = \frac{1}{2} \int_0^{2\pi} \left(\frac{a}{b}\right)^2 (R(s, t, \beta) \cos(\gamma) * h(t)) d\beta \quad (5-1)$$

where, $R(s, t, \beta)$ is the projection value at (s, t) on the projection $R(\beta)$, β is gantry rotation angle, γ is the angular between normal vector of detector and X-ray reached on detector, b is the projection of tube to point distance on the central X-ray SO, and D is the distance between X-ray tube and center of rotation (isocentric point) (Figure 5-3).

It can be confirmed that the projection is weighted by $\cos(\gamma)$ and convolved with filter $h(t)$ and the pixel value are back projected by using the projection and weighted by $(D/a)^2$. If the rotation angle of CT apparatus is limited between α and β , the reconstruction becomes a limited angle problem, which is tomosynthesis. In this case, Equation 5-1 was changed as,

$$f(x, y, z) = \frac{1}{2} \int_{\beta}^{\alpha} \left(\frac{a}{b}\right)^2 (R(s, t, \beta) \cos(\gamma) * h(t)) d\beta \quad (5-2)$$

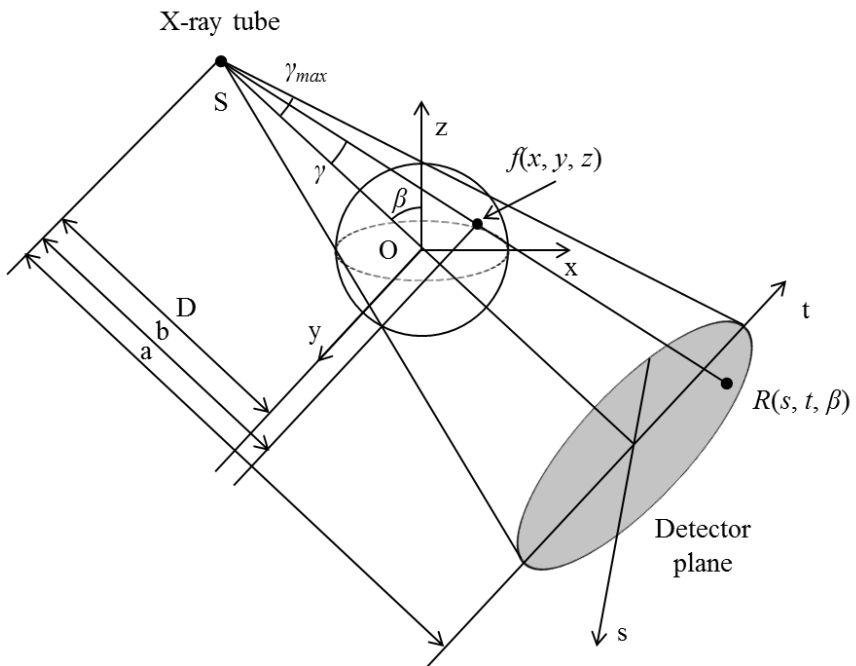


Figure 5-3. Cone beam geometry of complete isocentric motion

If the range of angle between ω_1 and ω_2 is small, $\cos(\gamma)$ becomes constant. When discrete numbers of N projections were taken, the angular interval will be $\Delta\beta = (\omega_2 - \omega_1)/N$. Then Equation 5-3 can be gained,

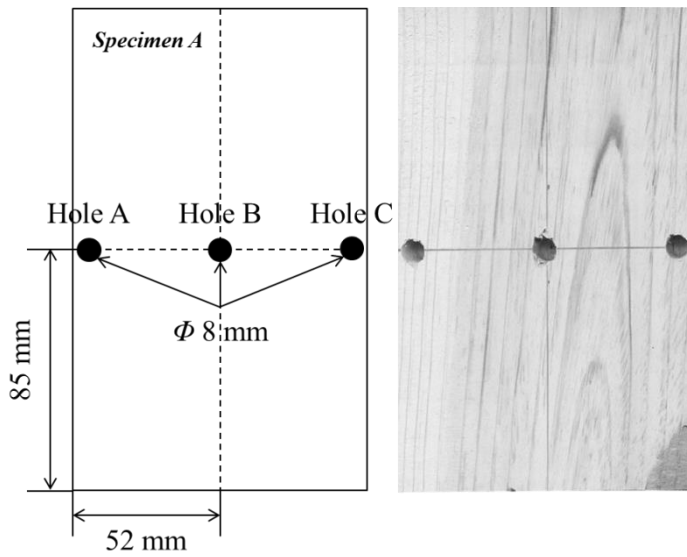
$$f(x, y, z) = \frac{1}{N} \sum_{i=1}^N \frac{1}{2} \left(\left(\frac{a}{b} \right)^2 \left((\omega_2 - \omega_1) R(s, t, \beta) * h(t) \right) \right) \quad (5-3)$$

This equation indicates filtered digital tomosynthesis reconstruction process considering based on weighted averaging of filtered projection corresponding to angle β . This equation was used to reconstruct tomosynthesis image.

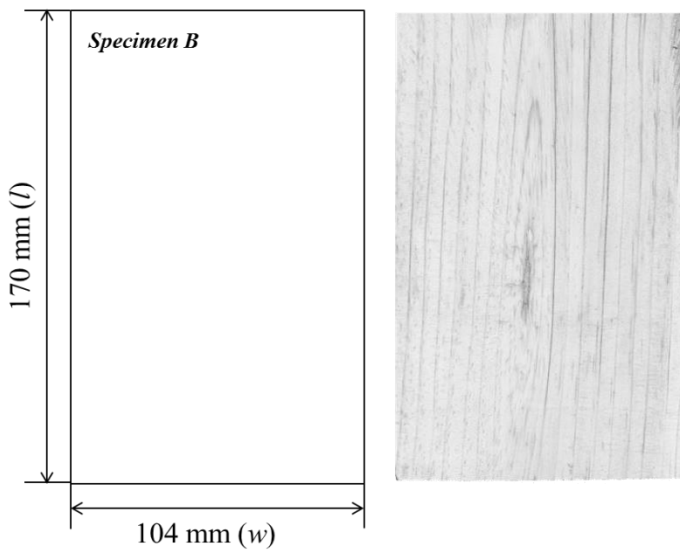
5.3. Materials and experimental method

5.3.1. Materials

Two sets of specimen were prepared. One was consisting of two pine wood. Pine (*Pinus densiflora*) is commonly used as the historic building member in Korea, and it is easily deteriorated by insect including termite (Kim et al., 2012). The average air-dry density, size and moisture content of two pine wood were 0.41 g/cm^3 , $104 \text{ mm (}w\text{)} \times 77.5 \text{ mm (}t\text{)} \times 170 \text{ mm (}l\text{)}$ and 15%, respectively. To find optimized condition of projection acquisition geometry for reconstructing tomosynthesis image, three artificial holes were made at surface of one specimen (specimen A). The diameter of artificial holes was 8 mm, whose diameter was as same as the average width of early wood of the specimen. The depth of each artificial hole was 10 mm. Figure 5-4 shows the detail of the specimens. Three holes from left to right shown in Figure 5-4a were designated as hole A, B and C, respectively. Other was stem having heart rot and deteriorated wood member. Wood member had been used to verify the accuracy of CT image in chapter 4.

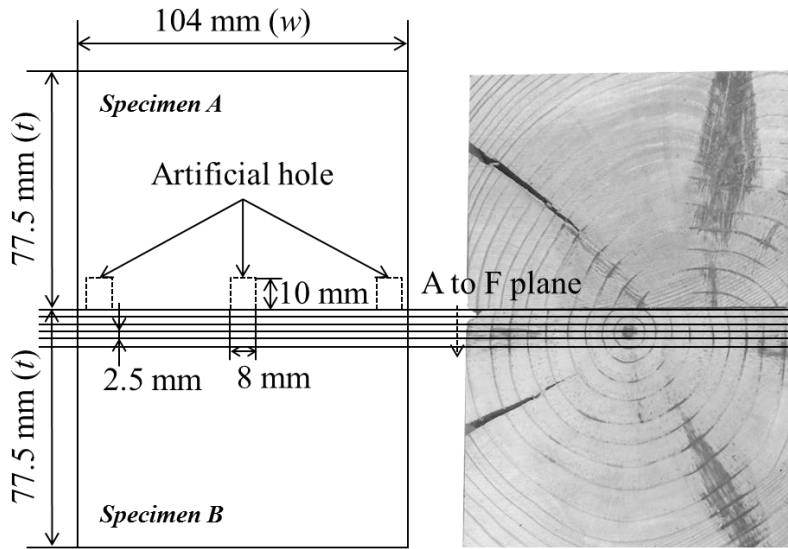


(a) Specimen A among two pine wood



(b) Specimen B among two pine wood

Figure 5-4. Two pine wood (continue)



(c) Top view of two pine wood

Figure 5-4. Two pine wood

5.3.2. Tomosynthesis apparatus

K-4 (Softex, Japan) was used to emit X-ray. The maximum tube voltage and current were 64 kV and 5 mA. From the results of a preliminary test, the tube voltage of 45 kV and current of 5 mA were determined to radiate X-rays. EVS 4343 (DRtech., Korea) was employed to take projections, and its spatial resolution was 3.5 line pair/mm. One projection was taken by exposing the detector to X-ray during 1.2 seconds.

The complete isocentric motion shown in Figure 5-2 was used to take projections for reconstructing tomosynthesis image. In the complete isocentric motion, the tube and detector were concurrently rotated a certain angular interval. The CT gantry shown in Figure 4-5b was also employed to rotate the tube and detector. Figure 5-5 shows the schematic drawing for tomosynthesis test. During the tomosynthesis test, the distance of 1054.37 mm between the tube and detector was fixed, and the length of 863.72 mm between the tube and center of rotation was also maintained. The two pine wood were placed as one surface of specimen A including the artificial hole meet another surface of specimen B as shown in Figure 5-4c, and the boundary where the surface meets each specimen was located at the center of rotation during the test.

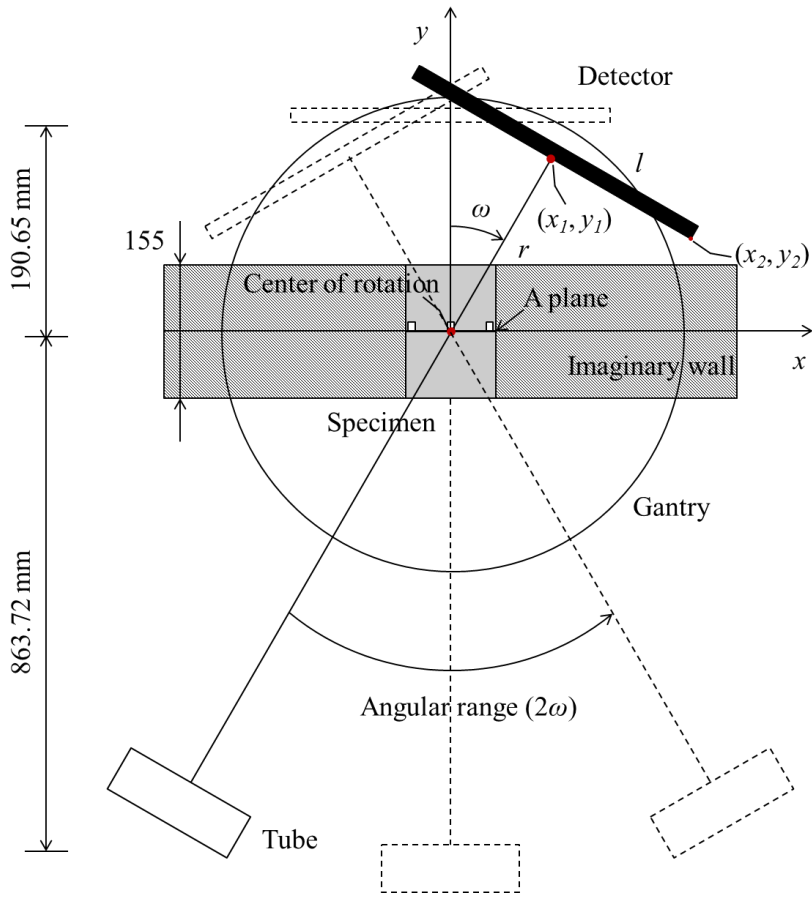


Figure 5-5. Schematic drawing for tomosynthesis test

5.3.3. Condition of radiography for investigating of wood with tomosynthesis

To reproduce how tomosynthesis apply at wood column having walls, an imaginary wall was assumed as shown in Figure 5-5. The thickness of the imaginary wall was 155 mm, which was same length of sum of two pine wood thickness. Using the geometry of tomosynthesis and the thickness of imaginary wall, the maximum angular range (2ω in Figure 5-5) of complete isocentric motion was determined. If the edge of detector, y_2 in the Figure 5-5, is located above a half of thickness of the imaginary wall, the tomosynthesis apparatus can be rotated sufficiently. The maximum angular range can be calculated by using Equation 5-4,

$$2\omega = r \cos(\omega) - l \sin(\omega) \quad (5-4)$$

where, ω is the half angle of the maximum rotation angle ($^\circ$), r is the distance between the detector and center of rotation (here, 190.65 mm), and l is a half of width of detector (215 mm). A half of maximum angular range (ω) calculated was 34.07 degrees, therefore, the maximum angular range of 60 degrees was chosen. Using the information, the radiography conditions to take projections for reconstructing tomosynthesis were established. Table 5-1 shows the radiography conditions.

The filtered back projection algorithm for tomosynthesis considering cone-beam and flat panel detector (Badea, 2000) was used to reconstruct tomosynthesis image for every radiography conditions. Whole projections gained from tomosynthesis testing were filtered by using the ram-lak filter to remove blur in reconstructed image. The reconstructed voxel size of image was 0.64 mm \times 0.64 mm \times 0.64 mm.

Table 5-1. Radiography conditions to take projections

Section	Radiography condition		
	Angular range (°)	Angular interval (°)	Projections (EA)
1	20	4	6
2	20	2.5	9
3	20	2	11
4	20	1	21
5	20	0.5	41
6	40	8	6
7	40	5	9
8	40	4	11
9	40	2.5	17
10	40	2	21
11	40	1	41
12	40	0.5	81
13	60	7.5	9
14	60	6	11
15	60	5	13
16	60	4	16
17	60	3	21
18	60	2.5	25
19	60	2	31
20	60	1.5	41
21	60	1	61
22	60	0.5	121

5.3.4. Evaluation of quality of tomosynthesis image

To evaluate quality of reconstructed tomosynthesis image of in-focus plane, the contrast-to-noise ratios (CNRs) between the each artificial hole and wood surrounded the hole in reconstructed tomosynthesis image were computed. In-focus plane is the location where the inspector wants to reconstruct. Figure 5-4c shows the in-focus plane as “A plane”, which was located at the center of rotation. The CNR value could be calculated by using Equation 5-5 (Zhang et al., 2006),

$$CNR = \frac{|\bar{I}_{signal} - \bar{I}_{BG}|}{\sigma} \quad (5-5)$$

where, \bar{I}_{signal} and \bar{I}_{BG} are the average pixel gray scale of the signal region of interest (ROI) and background ROI, and σ is the standard deviation of the signal or background ROI. Here, the signal and background region indicate the location of artificial hole and wood round the hole in reconstructed image, respectively. The signal and background ROI were defined as 3×3 voxel square at each location. The number of signal ROI measured was 20, while the number of background ROI was 25. This was because the size of background ROI was larger than that of signal ROI. The CNR is quantitative metric for detection, and it is common practice to measure the standard deviation of background in medical field (Hendrick, 2007). In this study, however, the standard deviation of signal was used to calculate CNR because the difference between earlywood and late wood in background can cause high standard deviation. To analysis how the different radiography conditions affect CNR, each CNR value was returned to be normalized CNR dividing by the maximum CNR in same angular range.

To measure image blur in the vertical direction (minus y direction in Figure 5-5) and the quality of vertical resolution of the reconstructed tomosynthesis images, Wu et al. (2004) introduced the artifact spread function (ASF), which is defined as the ratio of the CNR values between the off-focus plane and the in-focus plane,

$$ASF = \frac{CNR(y)}{CNR(y_0)} = \frac{\bar{I}_{signal}(y) - \bar{I}_{BC}(y)}{\bar{I}_{signal}(y_0) - \bar{I}_{BC}(y_0)} \quad (5-6)$$

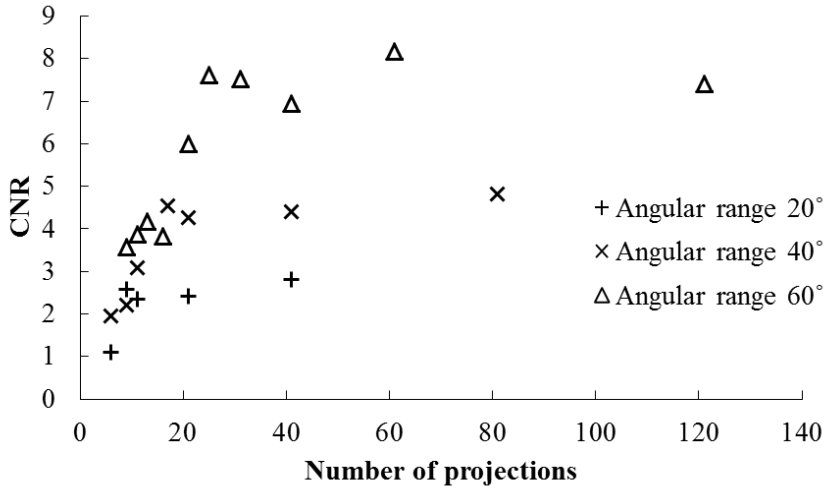
where, y_0 is the slice location of the in-focus plane (A plane) and y is the location of out-focus planes (B to F plane). The five out-focus planes were determined to calculate ASF for the each reconstructed tomosynthesis image, and the location of that is illustrated in Figure 5-4c. The distance between adjacent planes including the in-focus plane was 2.5 mm. Each calculated ASF was fitted to a polynomial function according to the y direction, and the width of the y location where the maximum ASF equals to half was determined to evaluate the quality of vertical resolution (Judy et al., 1977; Lu et al., 2011; Oh et al., 2012; Pang et al., 2008; Wu et al., 2004; Zhang et al., 2006; Zou et al., 2011).

5.4. Results and discussion

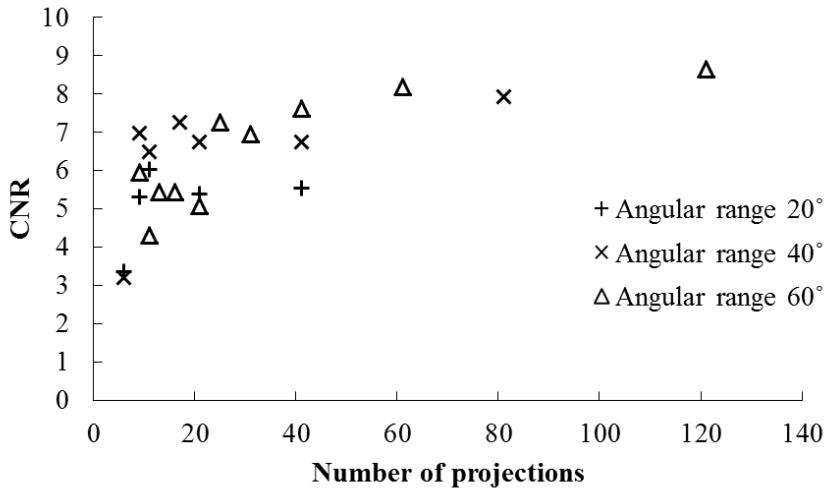
5.4.1. Optimum condition of radiography for investigating of wood with tomosynthesis

Figure 5-6 shows CNR of in-focus plane (A plane) according to the location of hole in various numbers of projections. In case of angular range of 20 degrees, the CNRs for all hole location were lower when they were compared with the results came from other angular ranges for all hole location. Moreover, the angular range dissimilarly affected the results of CNR according to the location of hole. The CNRs of hole A and C which were located in edge of specimen were more influenced according to angular range. In case of hole B, angular ranges did not affect the results of CNR significantly. The maximum CNRs of each hole were confirmed at angular range of 60 degrees, and the numbers of projection for the maximum CNRs of hole A, B and C were 61, 121 and 61, respectively.

Normalized CNRs were also calculated by using the maximum CNRs for each angular range and hole location. Figure 5-7 shows the normalized CNRs for determining the maximum angular interval. In other words, the least number of projections required to reconstruct available tomosynthesis image in in-focus plane was investigated with the criteria as 0.8 normalized CNR. When the reconstructed tomosynthesis image were compared with each other, there was no significant different above 0.8 normalized CNR. Table 5-2 summarized the least number of projections according to location of hole and angular range with the criteria. The least numbers of projections for angular range of 20 degrees and 40 degrees were 21 and 31 when the normalized CNRs for whole three holes indicated above 0.8 normalize CNR.

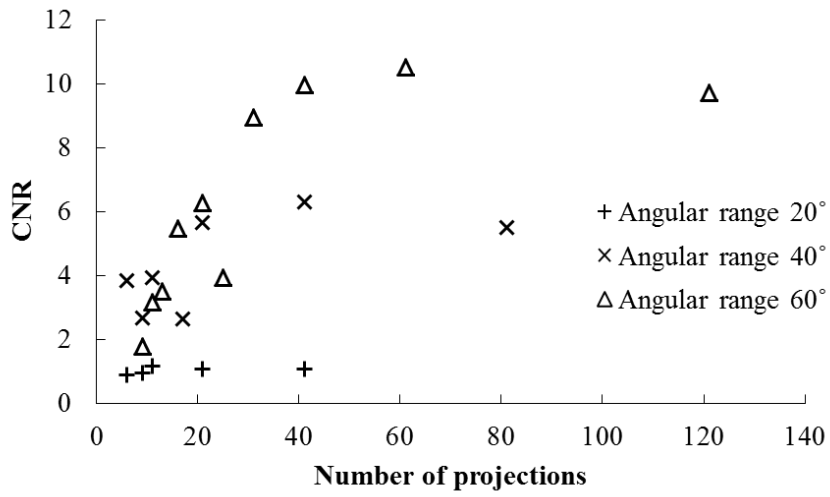


(a) Hole A



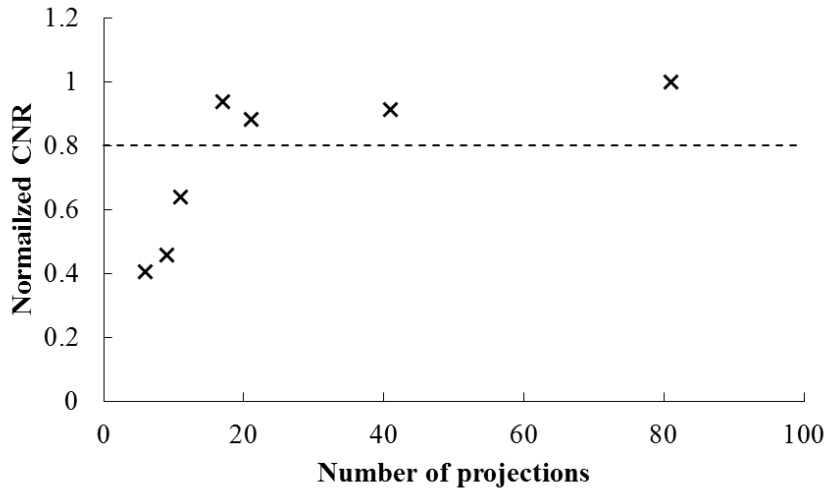
(b) Hole B

Figure 5-6. CNR of hole A, B and C according to angular range in various numbers of projections (continue)

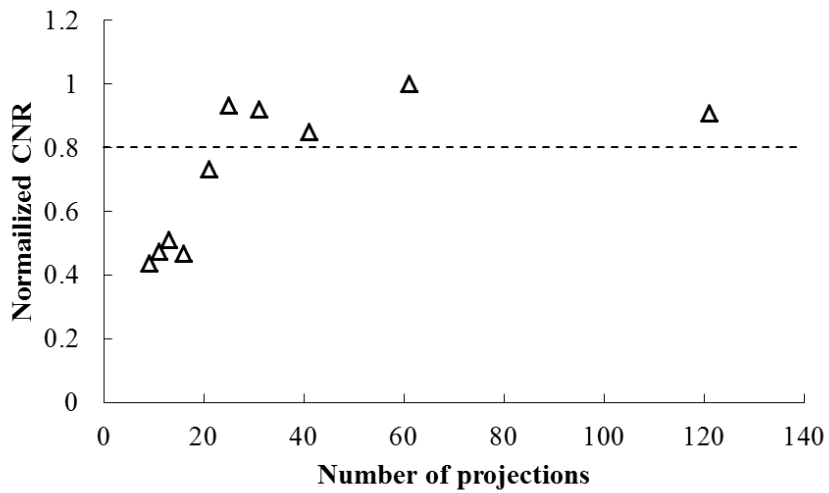


(c) Hole C

Figure 5-6. CNR of hole A, B and C according to angular range in various numbers of projections

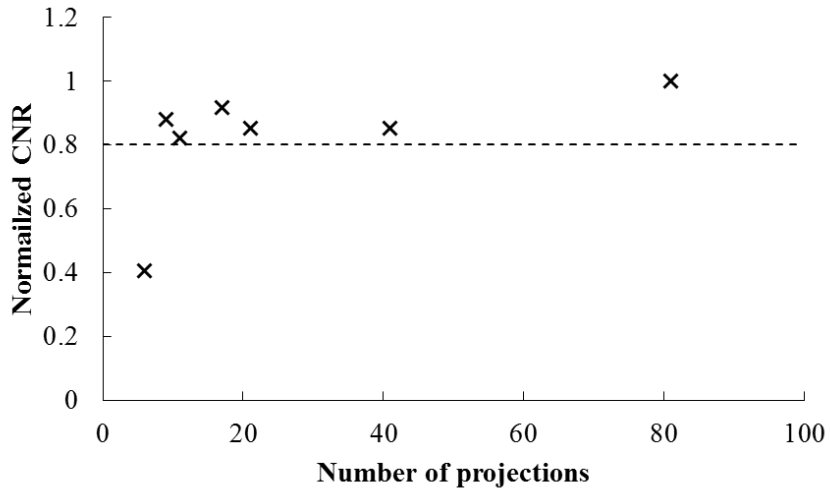


(a) Hole A and angular range of 40 degrees

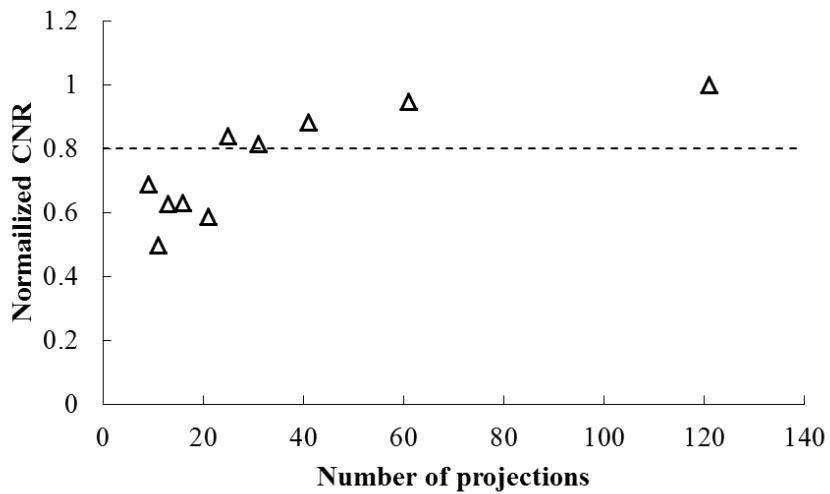


(b) Hole A and angular range of 60 degrees

Figure 5-7. Normalized CNR according to location of hole A and angular range (continue)

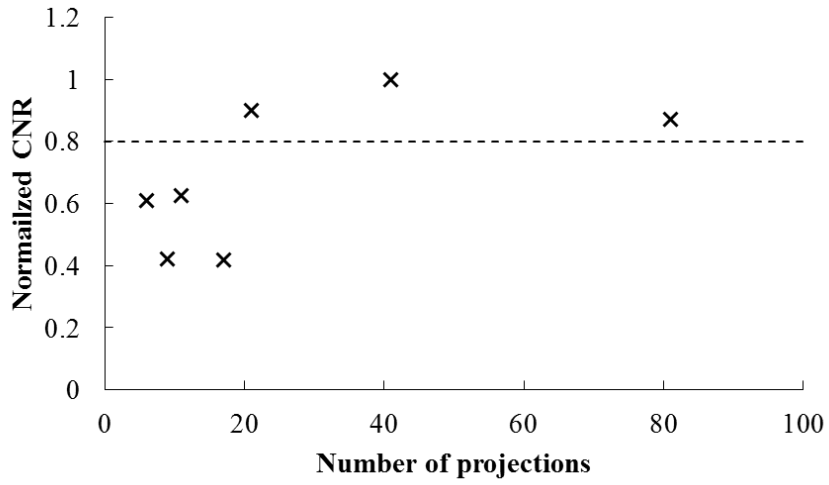


(c) Hole B and angular range of 40 degrees

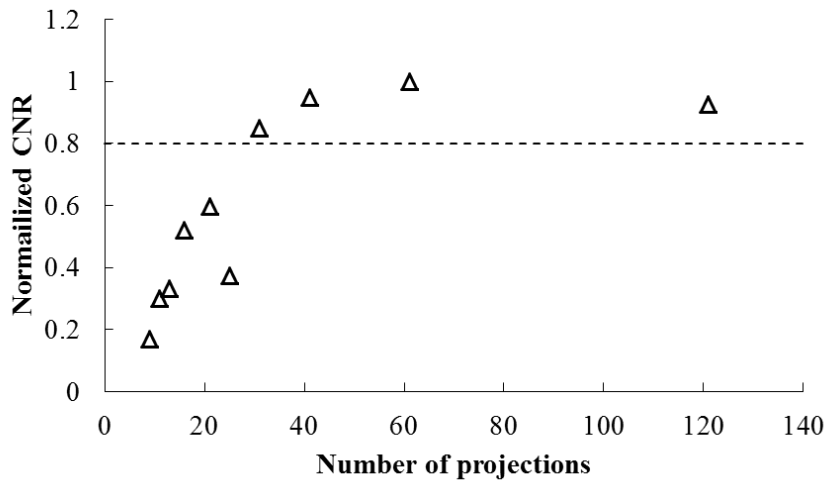


(d) Hole B and angular range of 60 degrees

Figure 5-7. Normalized CNR according to location of hole and angular range (continue)



(e) Hole C and angular range of 40 degrees



(f) Hole C and angular range of 60 degrees

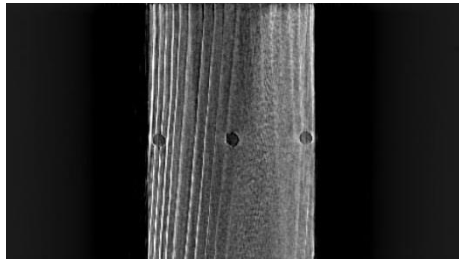
Figure 5-7. Normalized CNR according to location of hole and angular range

Table 5-2. The least number of projections with 0.8 normalized CNR criteria

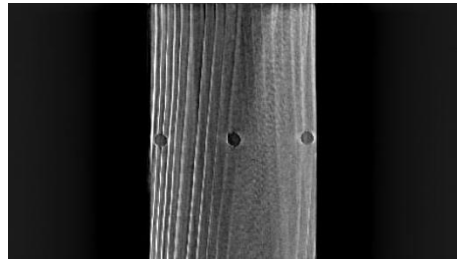
Angular range (°)	The least number of projections		
	Hole A	Hole B	Hole C
40	17	9	21
60	25	25	31

Figure 5-8 shows the results of reconstructed image with tomosynthesis. It was confirmed that state of in-focus plane was successfully investigated with previous radiography condition for angular range of 40 degrees and 60 degrees. Holes located in edge of specimen were needed more radiographs to reconstruct tomosynthesis image for both angular range. And more radiographs were needed to reconstruct tomosynthesis image when larger angular range was used. In wooden building, the deterioration could occur frequently in edge of members. Therefore, it was reasonable to determine the optimum radiography condition for in-focus plane based on the result of CNRs of hole A or C.

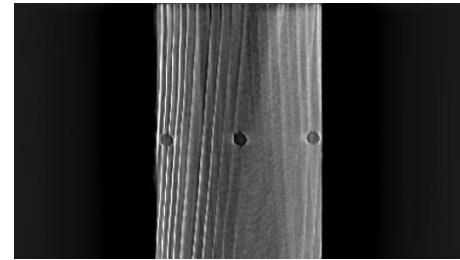
Sechopoulos (2013) summarized that characteristics of tomosynthesis systems in medical used or under development. General angular range of tomosynthesis system in medical field was smaller than 30 degrees, and the number of projection was less than 25. Compared with results in this study, they could investigate patient with tempered radiography conditions. This is because difference of resolution of detector and complexity of inspection object. Zhao et al. (2015) reported that the spatial resolution and pixel size of detector were highly influenced on the reconstructed tomosynthesis image quality. Typical spatial resolution of detector for investigating microcalcifications with tomosynthesis in medical field was 5 lp/mm, and it is higher than that of detector used in this study. Moreover, wood is more complex than human body. Thus, more projection and larger angular range could be needed to investigate inner state of wood with reconstructed tomosynthesis image.



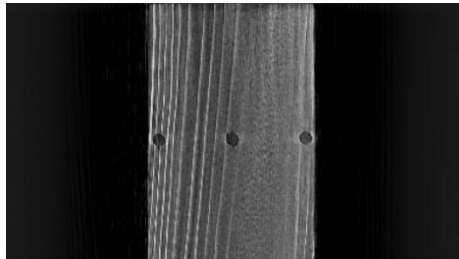
(a) A. R.* 40 and N. P.** 21



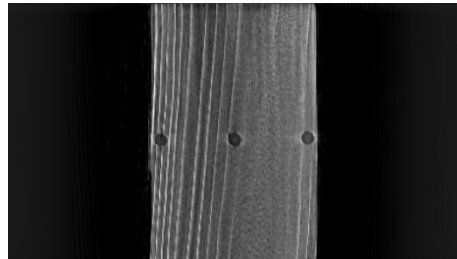
(b) A. R. 40 and N. P. 41



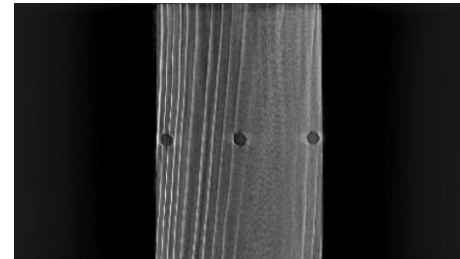
(c) A. R. 40 and N. P. 81



(d) A. R. 60 and N. P. 31



(e) A. R. 60 and N. P. 41

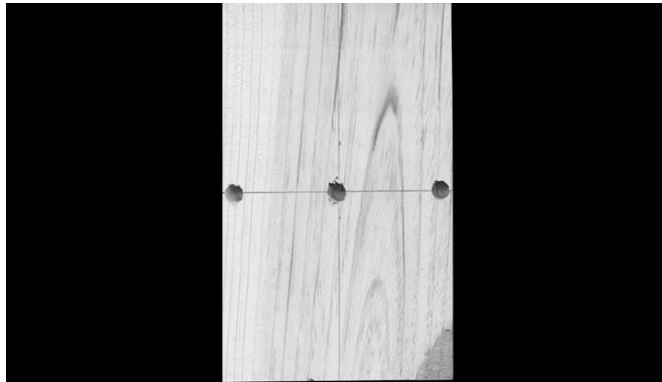


(f) A. R. 60 and N. P. 61

* A. R.: Angular Range, **N.P.: Number of projection

Figure 5-8. Reconstructed tomosynthesis image according to angular range and number of projection

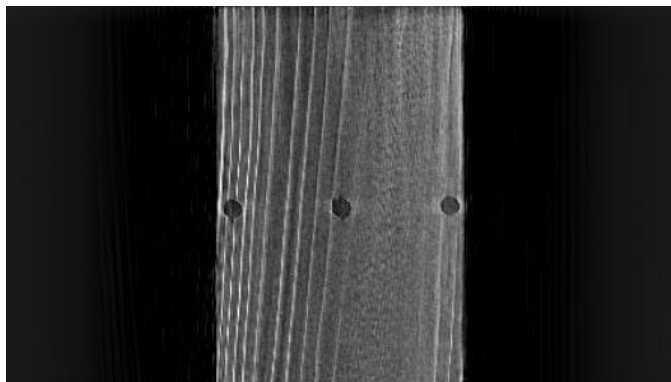
The result of tomosynthesis must have blurring in reconstructed image, and thus it cannot be used to investigate inner state of wood, quantitatively. However, it has advantage to examine wood compared with single radiograph. Figure 5-9 shows actual picture of in-focus plane, single radiograph and tomosynthesis image which was reconstructed by using 31 radiographs from 60 degrees angular range. Single radiograph must have superposition of structure due to overlapping results along with X-ray path. Therefore, it is difficult to detect inner state of wood with single radiographs as shown in Figure 5-9b. However, the tomosynthesis image with optimum radiography condition (60 degrees angular range and 31 radiographs) could determine in-focus plane state compared with actual picture of that. From the results of tomosynthesis image, it was confirmed that not only location of holes but also shape of grain could be detected.



(a) Actual picture of in-focus plane



(b) Single radiograph

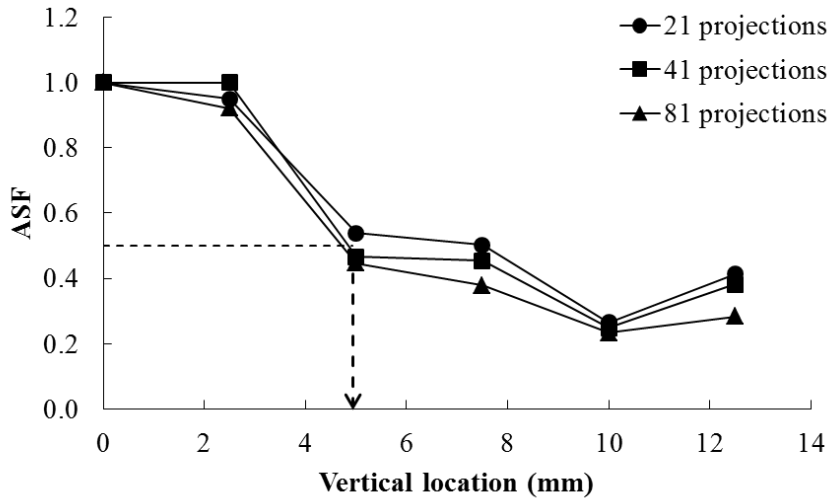


(c) Reconstructed image

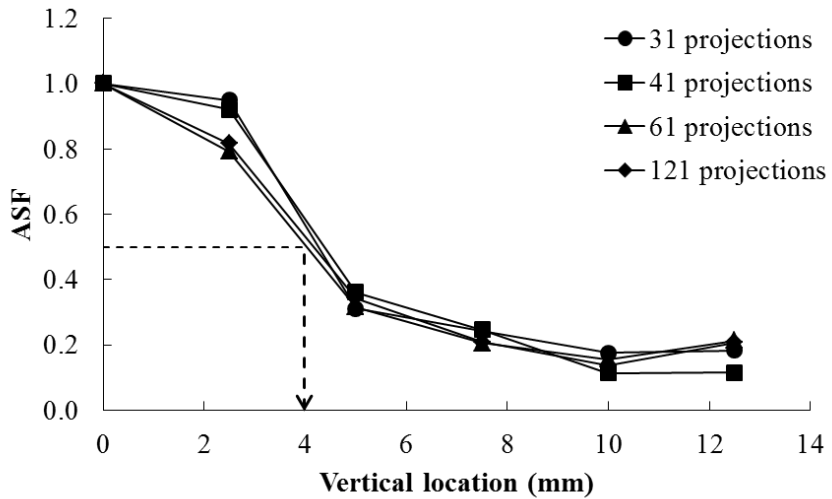
Figure 5-9. Results of single radiograph and reconstructed image

In previous discussion, it was suggested that the numbers of projections for angular range of 40 degrees and 60 degrees regardless of the location of hole. It also confirmed that the numbers of projections and over did not affect the quality of reconstructed image at in-focus plane, significantly. Therefore, tomosynthesis images reconstructed by using 21 projections, 41 projections and 81 projections for 40 angular range or 31 projections, 41 projections, 61 projections and 121 projections were employed to calculate ASF for measuring image blur in the vertical direction and the quality of vertical resolution of the tomosynthesis images. Figure 5-10 shows the results of ASF according to angular range and number of projections, and Table 5-3 shows the width of the y location where the maximum ASF equals to half. The maximum ASF equals to half was influenced by the location of hole, and it was high when the maximum ASF equals to half was calculated at center of specimen. On the other hand, the vertical resolution of reconstructed tomosynthesis image was rarely influenced by the number of projections, while the angular range affected the vertical resolution greatly. As angular range increased, the image blur in the vertical direction decreased rapidly. For angular range of 40 degrees and 60 degrees, the average widths of the y location where the maximum ASF equals to half were 9.37 mm and 6.86 mm, respectively.

It was considered that the angular range effect on the sampled region in the frequency domain of projection. So, the region increased as the angular range increased. The previous study was consistent with this result (Hu et al., 2008; Sechopoulos and Ghetti, 2009). Compared with medical tomosynthesis, the vertical resolution was low. This is because the detector used in this study is not for tomosynthesis but chest radiographs, and it has low spatial resolution.

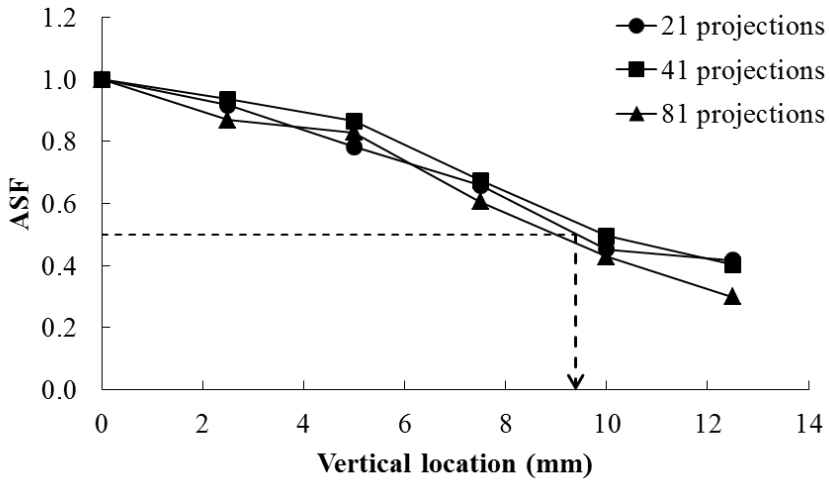


(a) Angular range 40; hole A

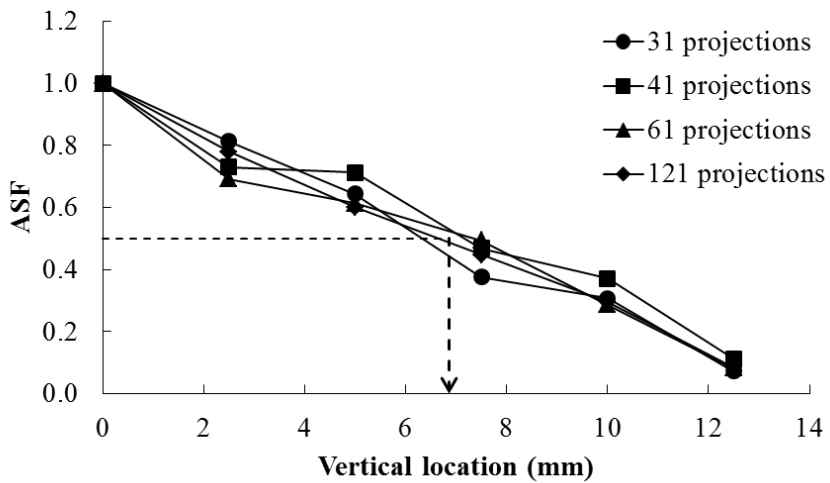


(b) Angular range 60; hole A

Figure 5-10. ASF according to angular range and location of hole
(continue)

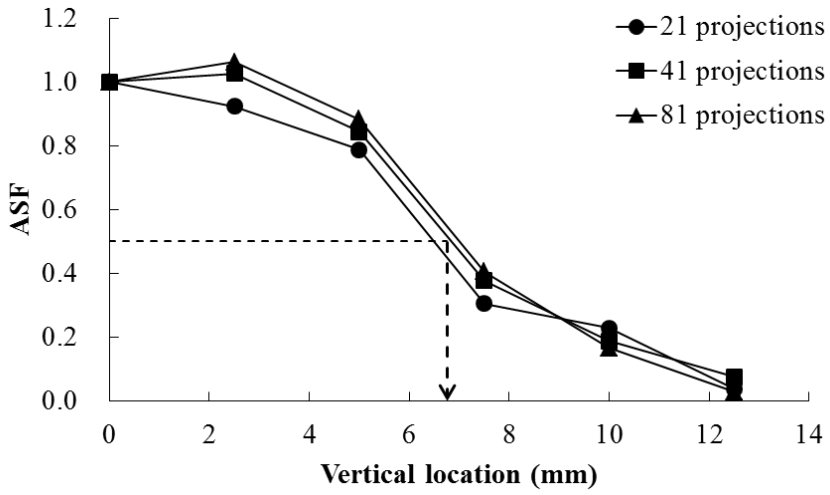


(c) Angular range 40; hole B

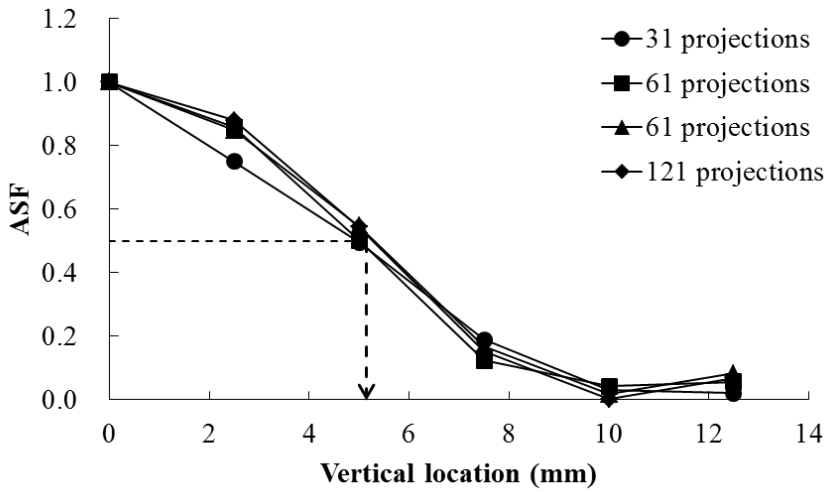


(d) Angular range 60; hole B

Figure 5-10. ASF according to angular range and location of hole
(continue)



(e) Angular range 40; hole C



(f) Angular range 60; hole C

Figure 5-10. ASF according to angular range and location of hole

Table 5-3. *y* location of 0.5 ASF in various angular ranges and locations of hole

Angular Range (°)	Number of projection	<i>y</i> location of 0.5 ASF (mm)				
		Hole A		Hole B		Hole C
40	21	5.62		9.46		6.44
	41	4.67	4.94* (0.60)**	9.91	9.37 (0.60)	6.81 (0.27)
	81	4.52		8.73		6.98
60	31	4.00		6.25		4.97
	41	4.14	3.98	7.15	6.86	5.01
	61	3.80	(0.14)	7.41	(0.52)	5.29
	121	3.96		6.63		5.26

* Average

** Standard deviation

In medical field, many researchers have studied about the optimum radiography condition to obtain high quality of reconstructed image expecting the least radiation exposure for patients (Chawla et al., 2009; Lu et al., 2011; Sechopoulos and Ghetti, 2009). Sechopoulos and Ghetti (2009) reported that the highest quality reconstruction, considering both in-focus plane quality and vertical resolution, consisted of the acquisition of 13 projections with angular range of 60 degrees and over. In the study, there was no correlation between the number of projection and in-focus plane quality. Because of dose limitation, they had to change the exposure time for one projection. However, tomosynthesis for nondestructive evaluation of wood is rather free to dose limitation compared the medical usage. Therefore, the exposure time for one projection can be maintained regardless of number of projections. The in-focus plane quality increased as the number of projections increased, and then the in-focus plane quality was constant in this study. The vertical resolution was correlated with angular range. It was consistent with the results of medical purpose (Oh et al., 2012). From previous results, the angular range of 60 degrees and the least number of projections of 31 was chosen to apply tomosynthesis for investigating wood. Figure 5-11 shows the results of reconstructed tomosynthesis image with those radiography conditions.

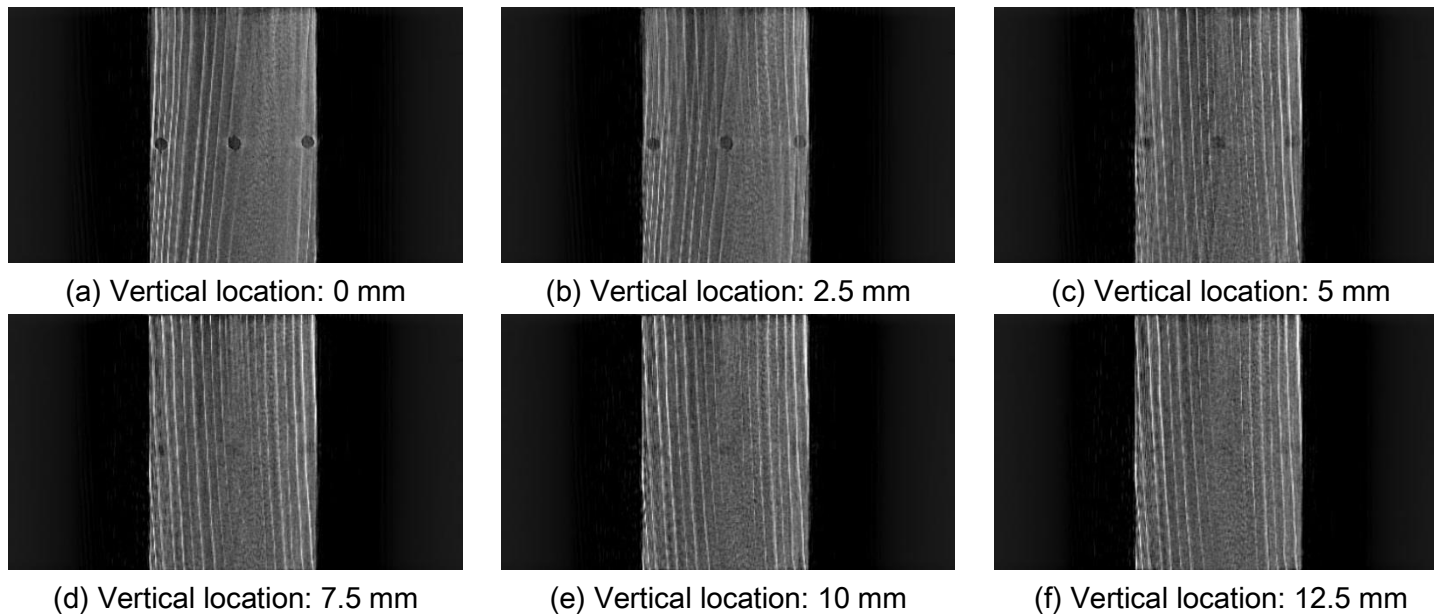


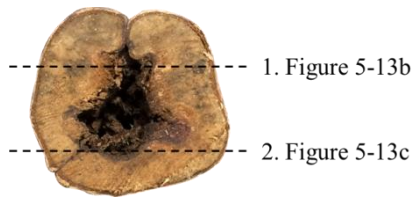
Figure 5-11. Reconstructed tomosynthesis image with angular range 60 degrees and 31 projections

5.4.2. Application of tomosynthesis for detecting inner state of wood

The optimum condition of tomosynthesis, angular range 60 and 31 projections, was applied to stem and wood member. Figure 5-12 shows the picture of the stem and wood member. When the cross section of stem was investigated, heart rot was easily confirmed. The wood member was also expected occurrence of deterioration. Figure 5-12a and 5-12c shows where tomosynthesis image were reconstructed in cross section image of each specimen.

Figure 5-13 and 5-14 presents picture of actual coronal section or single radiograph and reconstructed tomosynthesis image. The locations of reconstructed tomosynthesis image were calculated by using a proportion between actual diameter of specimen and the voxel size of reconstructed tomosynthesis image. The inner states of stem and wood member were hardly detected by using single radiograph, because single radiograph must have superposition of structure due to overlapping results along with X-ray path. On the other hand, tomosynthesis could determine inner state of wood without superposition. Compared the picture of actual coronal section, it was confirmed that the accuracy of reconstructed tomosynthesis image was high. Natural deterioration in stem could be investigated by using the reconstructed tomosynthesis image. Moreover, it was considered that the crack and location of knot could be determined from the results of wood member.

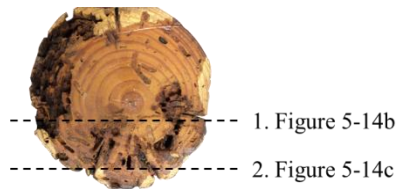
Judging from the fact that tomosynthesis could detect natural deterioration, crack and shape of knot, it can be used to investigate wood member where CT could hardly applied. And it is looking forward to apply the process for grading of timber or quality control of engineering wood.



(a) Cross section of stem



(b) Stem

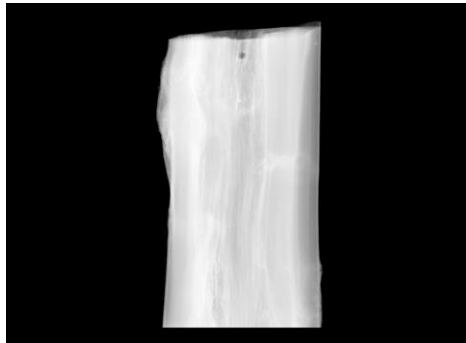


(c) Cross section of wood member

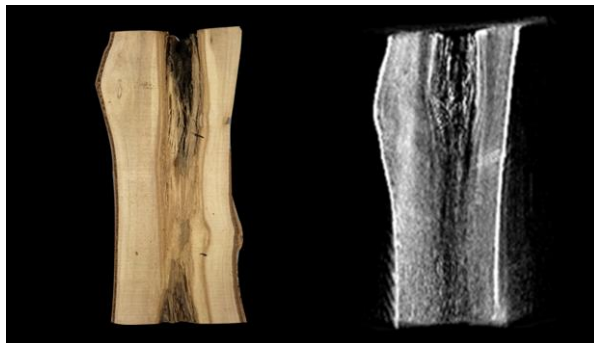


(d) Wood member

Figure 5-12. Specimen applied tomosynthesis



(a) Single radiograph

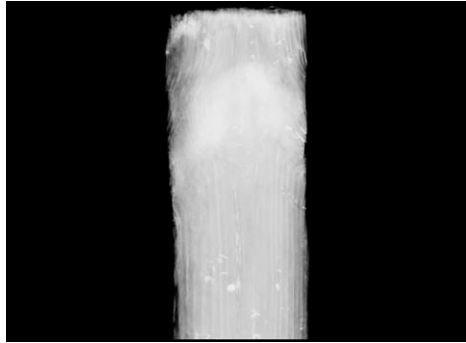


(b) Picture of actual coronal section and result of tomosynthesis 1

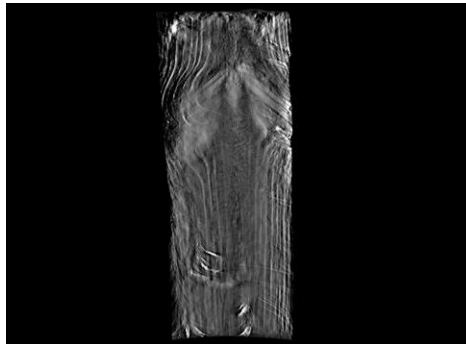


(c) Picture of actual coronal section and result of tomosynthesis 2

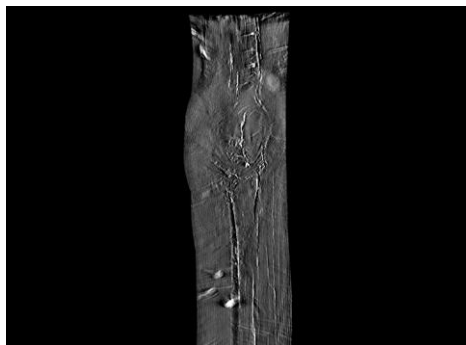
Figure 5-13. Result of reconstructed tomosynthesis image about stem



(a) Single radiograph



(b) Results of tomosynthesis 1



(c) Results of tomosynthesis 2

Figure 5-14. Results of reconstructed tomosynthesis image about wood member

5.5. Conclusion

To improve applicability of nondestructive testing and evaluation using X-ray, feasibility study about tomosynthesis was firstly conducted in field of wood science. It has advantage to reconstruct arbitrary plane by using few numbers of projections from limited rotation angle of X-ray apparatus. The complete isocentric motion was used to obtain projections to reconstructed tomosynthesis image. The reconstruction algorithm was back projection with ram-lak filter considering the geometry of cone beam and flat panel. Considering the imaginary wall, the maximum angular range was chosen and various radiography conditions were used to find optimum condition for reconstructing tomosynthesis image. CNR was applied to evaluate the quality of reconstructed tomosynthesis image of in-focus plane, and ASF was calculated to assess the quality of vertical resolution. At least 31 projections for 60 degrees angular range were needed to make reconstructed image having reasonable quality of in-focus plane. While, the vertical resolution increased as the angular range larger. Therefore, the optimum condition for obtaining projection was suggested with the angular range of 60 degrees and 31 projections. With the proposed conditions, stem and wood member could be investigated successfully by using reconstructed tomosynthesis image, which could provide information about shape of deterioration, location of crack and knot. The information could not be obtained by not only visual inspection but single radiograph. Judging from the results, it was considered that tomosynthesis can be used to investigate wood member where CT could not applied.

Chapter 6

Dual X-ray Absorptiometry Method for
Evaluating Moisture Content of Solid wood

6.1. Introduction

The gravimetric method is commonly used for determining moisture content, which is defined as the ratio of the mass of water to the oven-dry mass of wood. It has high accuracy while it is rarely affected by other factors such as specific gravity and temperature of wood (Jensen et al., 2006). However, it spends a considerable time and labor on gaining oven dry weight of wood, and it reveals only local moisture content in wood. Because manufacturing lumber and wood drying processes can operate continuously and whole moisture content is required for evaluating wood quality, it is necessary to develop an alternative method to determine the moisture.

Basically, radiation including gamma- and X-rays have high energy to penetrate thick wood, and is attenuated as they traverse through materials or chemical compounds regardless of surface condition. Because of that, many researchers have been conducted to apply radiation for estimating air-dry density of wood. Moisture content of wood has been also nondestructively investigated by using radiation (Alkan et al., 2007; Watanabe et al., 2012; Watanabe et al., 2008). They investigated moisture content and distribution of that in wood, successfully with single effective energy. However, the major drawback of single effective energy radiography is that a projection of oven-dry density investigated wood should be needed for calculating moisture content in wood. It means that single effective energy radiography have same problem with the gravimetric method.

Dual X-ray absorptiometry method, therefore, was conducted to assess the moisture content of wood without information of oven-dry density. The Dual X-ray absorptiometry method is referred as the method using two different effective energies. For deriving an equation of dual X-ray absorptiometry method, the apparent mass attenuation coefficients of Korean

pine wood substance, which is amount of wood in oven-dry condition, and of moisture were calculated. Influence factor and the accuracy of estimation for dual X-ray absorptiometry also discussed.

6.2. Derivation of equation for dual X-ray absorptiometry

6.2.1. Apparent mass attenuation coefficient of wood substance and moisture for polychromatic X-ray

When polychromatic X-ray penetrates a homogenous material, the intensity of the transmitted polychromatic X-ray is attenuated exponentially as given Equation 3-4, 3-5 and 3-6 in the chapter 3. Finally, the apparent mass attenuation coefficient of wood could be expressed as Equation 3-7.

Jackson and Hawkes (1981) demonstrated that mass attenuation coefficient of mixture can be calculated by using the weighted sum of the coefficients for constituent elements, if the absorber consists of a chemical compound or a homogeneous mixture. Equation 6-1, therefore, can be written as follows,

$$\mu = \sum_{i=1}^N w_i \mu_i \quad (6-1)$$

where, μ is the mass attenuation coefficient of mixture consisting of N constituent elements (cm^2/g), w_i is the gravimetric proportion of i th constituent element and μ_i is the mass attenuation coefficient of i th constituent element (cm^2/g). If it is assumed that wood is regarded as a mixture of wood substance and moisture, the apparent mass attenuation coefficient of wood at k kV tube voltage can be calculated as shown in Equation 6-2,

$$\mu_{w+m,k} = \frac{100 - MC_m}{100} \mu_{w,k} + \frac{MC_m}{100} \mu_{m,k} \quad (6-2)$$

where, $\mu_{w+m,k}$ is the apparent mass attenuation coefficient of wood at k kV tube voltage (cm^2/g), $\mu_{w,k}$ is the apparent mass attenuation coefficient of wood substance at k kV tube voltage (cm^2/g), $\mu_{m,k}$ is the apparent mass attenuation coefficient of moisture at k kV tube voltage (cm^2/g) and MC_m is moisture content based on original weight (%). Here, the wood substance was referred as amount of oven-dried wood.

6.2.2. Assessment of moisture content in wood with dual X-ray absorptiometry

For the determination of moisture content in wood by using dual X-ray absorptiometry, a ratio of the apparent mass attenuation coefficients of wood at two different X-ray energies were used as shown in Equation 6-3,

$$r = \frac{\ln\left(\left(I_{0,a}/I_{1,a}\right)2\alpha_a\right)}{\ln\left(\left(I_{0,b}/I_{1,b}\right)2\alpha_b\right)} = \frac{\mu_{w+m,a}}{\mu_{w+m,b}} \quad (6-3)$$

where, r is a ratio of the apparent mass attenuation coefficients of wood, $I_{0,k}$ is the initial X-ray intensity at k kV tube voltage (μGy), $I_{1,k}$ is the transmitted X-ray intensity at k kV tube voltage (μGy), α_k is the integral value of probability function of the polychromatic X-ray at k kV tube voltage as shown in chapter 3.

Substituting Equation 6-2 in Equation 6-3, Equation 6-4 is obtained to assess for moisture content based on original weight,

$$r = \frac{(100 - MC_m)\mu_{w,a} + MC_m\mu_{m,a}}{(100 - MC_m)\mu_{w,b} + MC_m\mu_{m,b}} \quad (6-4)$$

Because moisture content based on oven-dry weight is usually applied in field of utilization of solid wood among wood science, Equation 6-4 is revised as Equation 6-5,

$$r = \frac{MC_d\mu_{m,a} + 100\mu_{w,a}}{MC_d\mu_{m,b} + 100\mu_{w,b}} \quad (6-5)$$

where, MC_d is moisture content based on oven-dry weight (%) and $MC_d = 100MC_m/(100-MC_m)$. Finally, moisture content based on oven-dry weight in wood can be estimated by Equation 6-6,

$$MC_d = \frac{100(\mu_{w,a} - r\mu_{w,b})}{r\mu_{m,b} - \mu_{m,a}} \quad (6-6)$$

Therefore, moisture content of wood can be determined by using the ratio of attenuation quantity (r value) and material properties (μ_w and μ_m) gained from two X-ray energies.

6.3. Materials and experimental methods

6.3.1. Materials

Ten clear specimens, Korean pine (*Pinus koraiensis*), were prepared as specimens. They were made from five different lumbers. The size and average oven-dry density of clear specimens were 20 mm (*T*) × 50 mm (*W*) × 200 mm (*L*) and $0.38 \text{ g/cm}^3 \pm 0.01 \text{ cm}^3$, respectively.

6.3.2. Experimental methods

The ten clear specimens were stored in decompression chamber with distilled water to add the water in wood. Figure 6-1 shows the decompression chamber. The atmospheric pressure within the chamber was changed twice from atmospheric pressure to 0.01 MPa, and each atmosphere condition was maintained during 30 minutes. Moisture content of the specimens increased up to fiber saturation point or above by using this method. As a result, the maximum moisture content of the specimens was obtained as 79.70 %.

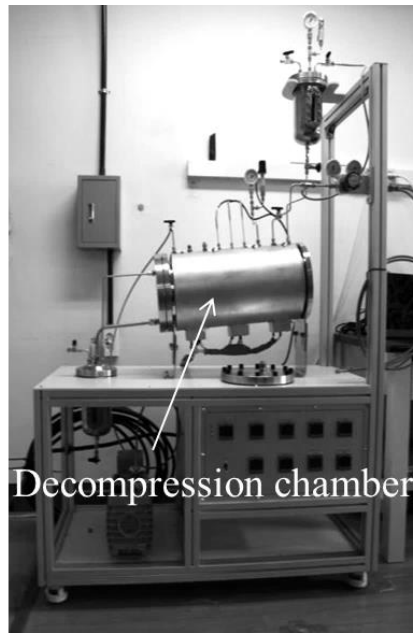


Figure 6-1. Picture of decompression chamber (Park et al., 2014)

X-ray tube, K-4 (Softex, Japan), was used to generate X-ray. For conduct dual X-ray absorptiometry, three tube voltages of 35 kV, 45 kV and 55 kV were chosen to radiate different X-ray energies. The X-ray tube current of 5 mA was constant during experiment. The digital detector named EVS 4343 (DRtech., Korea) was employed to take projections. All of projections were directly saved in laptop, and the format of that was DICOM. Detailed specification of the X-ray tube and digital detector had been written in the chapter 3. According to the tube voltage, different radiation time was used to take high quality projections for all specimens as shown in Table 3-2.

The ten clear specimens soaked in the distilled water were prepared to test as illustrated in the Figure 6-2. The distance between the X-ray tube and detector was set to 1209.2 mm, and the penetration depth of X-ray was 20 mm as same as the thickness (T) of specimens. Figure 6-2 shows the location of image indicator installed at the upper-right of detector according to ASTM E 1742/1742 M-12. The average gray scale value of IQI was used to evaluate projections whether quality of the projections uniformed or not. An outlier, whose average gray scale value of IQI was not belong to 1.5-fold inter-quartile range of the lower quartile or that of upper quartile, was eliminated, and it was not used to analyze results. Three projections per one specimen were taken by exposing the detector to X-ray with 35 kV, 45 kV and 55 kV tube voltages.

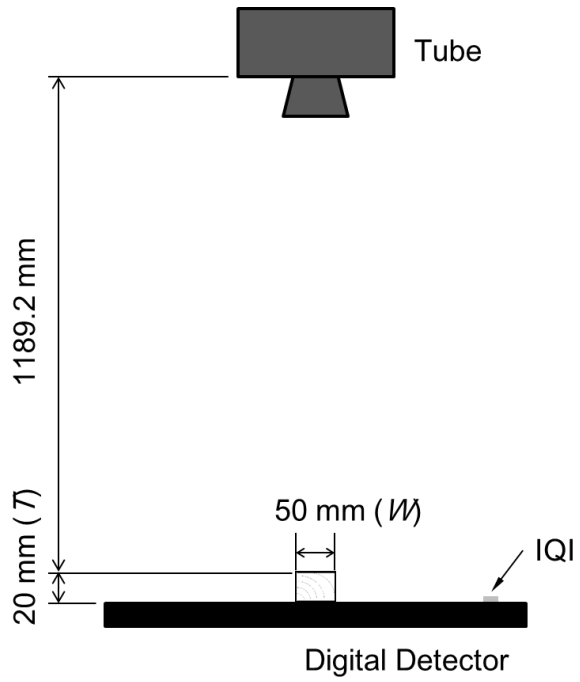


Figure 6-2. Test set-up for dual X-ray absorptiometry

Afterward, all specimens were dried in an oven at 40 °C or 70 °C in order to change moisture content of the specimens. Low temperature (40 °C) was used to dry the specimens having fiber saturation point and over, and then high temperature (70 °C) was applied to remove moisture of the specimen having under fiber saturation point. When it was checked that a weight of specimens was somewhat decreased, all of specimens were taken out from the oven. Then, the same procedure for taking three projections per one specimen was conducted again. That process as mentioned earlier was repeated until all of specimens were totally dried. An oven-dry weight was used to calculate oven-dry based density and moisture content, and an air-dry density of specimen for each testing was also obtained. Cracks and cups were occurred in some specimens during oven drying as shown in Figure 6-3, but it was considered that those drying defects were not influenced on the results of dual X-ray absorptiometry.

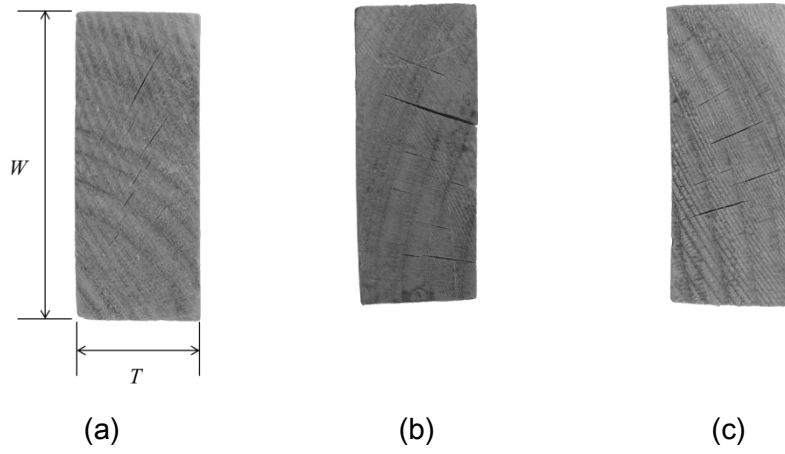


Figure 6-3. Cracks and cups occurred during oven drying

6.3.3. Application of dual X-ray absorptiometry

The ratio of initial X-ray intensity to transmitted X-ray intensity was calculated by using the dosimeter with the SFD chamber of 6 cm³ and the linear relationship between gray scale and exposure rate in the detector as introduced in the chapter 3. The dosimeter was used to measure initial intensity of X-ray while the linear relationship was used to calculate transmitted intensity of X-ray.

All results of projection for ten specimens were evaluated to apply the dual X-ray absorptiometry dividing into two groups as group 1 and group 2 as shown in Table 6-1. Firstly, results in the group 1 were used to apparent mass attenuation coefficient of wood substance and moisture. As shown in the chapter 3, Equation 3-6 was induced to evaluate an integral value of probability function. As it had been concluded that the integral value was related with the penetration depth, it was experimentally found by using Equation 3-6 without considering change of moisture content in wood. Therefore, the results of the integral value of probability function in chapter 3 were used once again. Revised Equation 3-6 with Equation 6-2 was conducted to calculate the apparent mass attenuation coefficient of wood substance and moisture. Because a mass attenuation coefficient of homogeneous material is not influenced by quantities (Hoag and Kraemer, 1991), the coefficients of Equation 6-7 were determined as the apparent mass attenuation coefficient of wood substance and moisture,

$$\ln(I_{0,k}/I_{1,k}) = \left(\mu_{w,k} - \frac{(\mu_{w,k} - \mu_{m,k})}{100} MC_m \right) \rho t - \ln(2\alpha) \quad (6-7)$$

Each regression analysis with least square method was conducted to

decide the coefficients of Equation 6-7 at 35 kV, 45 kV and 55 kV tube voltages. The coefficients were the apparent mass attenuation coefficient of wood substance and moisture. Secondly, validation of accuracy of the dual X-ray absorptiometry was conducted with the results in the group 2. A moisture content of specimens in the group 2 was determined by using three pair of r value as shown in Equation 6-3. The three pair of r value was 35 kV to 45 kV, 35 kV to 55 kV and 45 kV to 55 kV. The moisture content determined by dual X-ray absorptiometry was compared to moisture content measured by the gravimetric method, and the difference between the estimated and the measure moisture content was confirmed by calculating RMSE. To analyze projections, MATLAB R2015b (MathWorks, USA) were used.

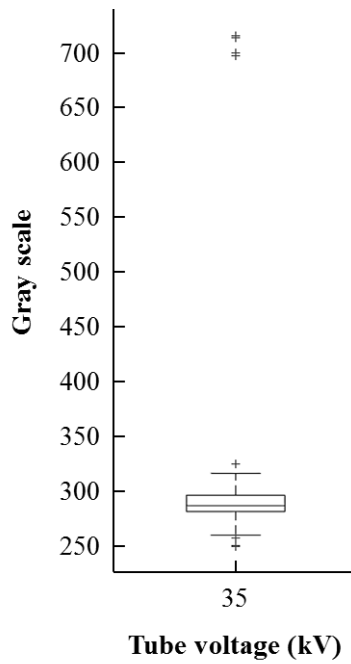
Table 6-1. Two groups for developing dual X-ray absorptiometry

Group	Type		Oven-dry density (g/cm ³)
	Lumber	Specimen	
1	A	A1	0.371
	B	B1	0.374
	C	C1	0.382
	D	D1	0.386
	E	E1	0.392
2	A	A2	0.367
	B	B2	0.373
	C	C2	0.385
	D	D2	0.387
	E	E2	0.394

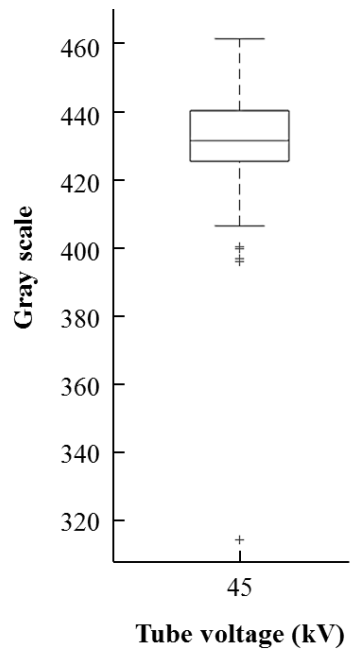
6.4. Results and discussion

6.4.1. Derivation of equations for dual X-ray absorptiometry

Before projections were analyzed, outliers had been found by calculating gray scale value of IQI in the projections. Figure 6-4 shows the results of the gray scale value at three tube voltages, 35 kV, 45 kV and 55 kV. The outliers beyond the 1.5-fold inter-quartile range of the lower quartile or that of upper quartile were expressed by using '+'. The total number of outliers at the three tube voltages was 9, 5 and 11. Those outliers were not analyzed for calculating the apparent mass attenuation coefficient of wood or for deriving equation of dual X-ray absorptiometry. Excluding the outliers, the number of three pair of projections according to three tube voltage was 42 in group 1 while that was 23 in group 2.

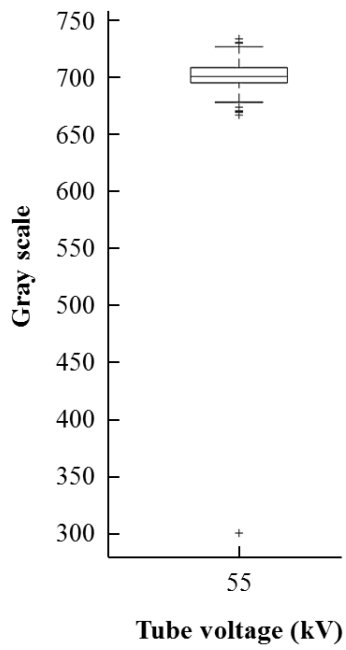


(a) 35 kV



(b) 45 kV

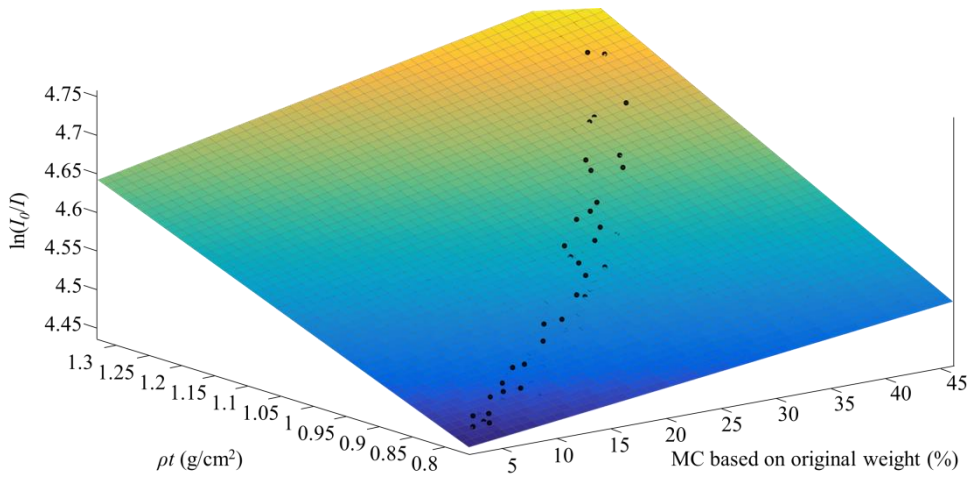
Figure 6-4. Outlier among projections at three tube voltages (continue)



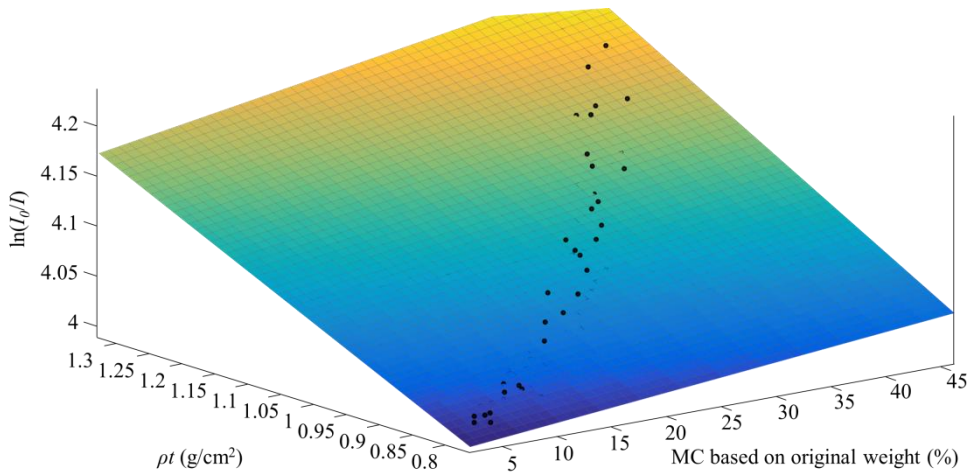
(c) 55 kV

Figure 6-4. Outlier among projections at three tube voltages

The results of 42 projections in group 1 at 35 kV, 45 kV and 55 kV tube voltages were used to calculate the apparent mass attenuation coefficients of wood substance and moisture by using Equation 6-7. The apparent mass attenuation coefficient of wood substance and moisture were gained by obtaining the coefficient of regression with 95% confidence level. Figure 6-5 shows graphs of the regressions equation with the apparent mass attenuation coefficient of wood substance and moisture at 35 kV, 45 kV and 55 kV tube voltages. The integral values of probability function (α), which were 0.0083, 0.0117 and 0.0161 at 35 kV, 45 kV and 55 kV as shown in Table 3-3, were used. The apparent mass attenuation coefficient of wood substance with 35 kV, 45 kV and 55 kV were 0.3474 cm²/g, 0.3179 cm²/g and 0.3148 cm²/g. On the other hand, the apparent mass attenuation coefficient of moisture with 35 kV, 45 kV and 55 kV were 0.5679 cm²/g, 0.4514 cm²/g and 0.3758 cm²/g.

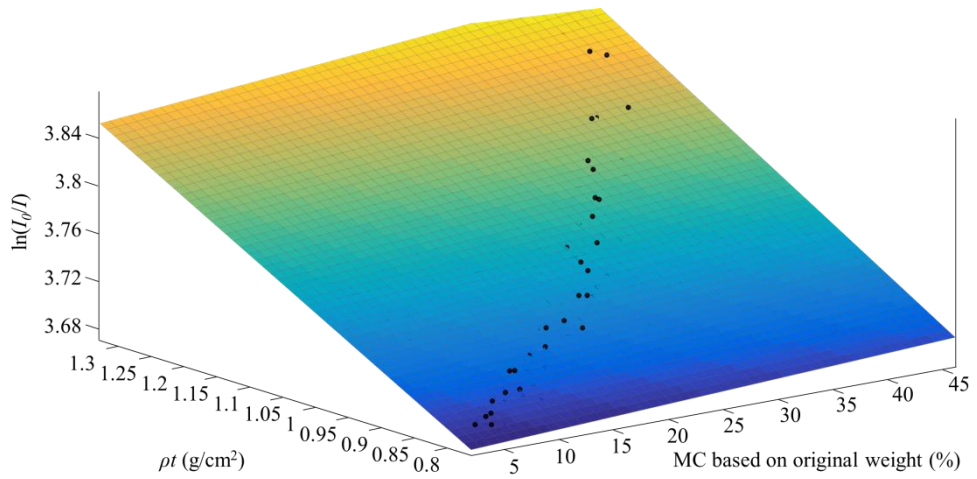


(a) μ_w : 0.3474 and μ_m : 0.5679 at 35 kV tube voltage



(b) μ_w : 0.3179 and μ_m : 0.4514 at 45 kV tube voltage

Figure 6-5. Regression equation with the apparent mass attenuation coefficient of wood substance (μ_w) and moisture (μ_m) at 35 kV, 45 kV and 55 kV tube voltages; $\ln(I_0/I) = (\mu_w - ((\mu_w - \mu_m)/100)MC_w) \rho t - \ln(2\alpha)$
(continue)



(c) μ_w : 0.3148 and μ_m : 0.3758 at 45 kV tube voltage

Figure 6-5. Regression equation with the apparent mass attenuation coefficient of wood substance (μ_w) and moisture (μ_m) at 35 kV, 45 kV and 55 kV tube voltages; $\ln(I_0/I) = (\mu_w - ((\mu_w - \mu_m)/100)MC_w)\rho t - \ln(2\alpha)$

Figure 6-6 shows the apparent mass attenuation coefficient of wood substance and moisture at 35 kV, 45 kV and 55 kV tube voltages. The apparent mass attenuation coefficients of that decreased as the tube voltage increased. Difference between the apparent mass attenuation coefficient of wood substance and that of moisture also decreased as the tube voltage increased. Therefore, the largest ratio between the apparent mass attenuation of moisture and wood was developed at tube voltage of 35 kV. It meant that low X-ray energy has advantage to measure moisture content of wood if single X-ray energy was used. As the difference between mass attenuation coefficient of wood substance and that of moisture was larger, moisture content can more affect mass attenuation coefficient of wood.

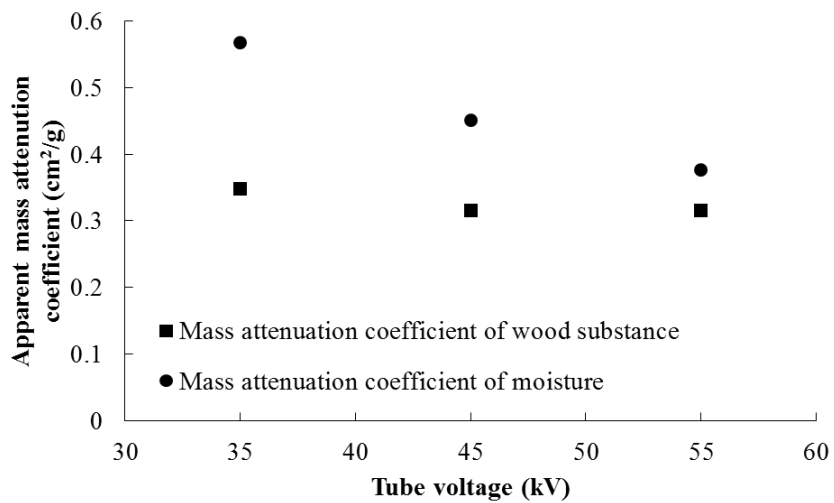


Figure 6-6. Apparent mass attenuation coefficient of wood substance and moisture

Using the three pairs of the mass attenuation coefficient of wood substance and moisture according to tube voltage, three r values in various moisture content were calculated by using Equation 6-5. The r values were the ratio of mass attenuation coefficient of wood between 35 kV and 45 kV, 35 kV and 55 kV, and 45 kV and 55 kV. Because the maximum moisture content of specimens in this study was 79.70%, the r values were calculated under 80% moisture content. Figure 6-7 presents the three r values from 0% to 80% moisture content range. All of the r values rose as moisture content of wood increased. It was considered that the r value could be used to estimate moisture content in wood because a one-to-one correspondence between the r values and moisture content was found.

With large distinction between two tube voltages, variance of r value was greatly in changing of moisture content. The largest difference of the r value between moisture content of 0% and that of 80% was 0.1991 when 35 kV and 55 kV tube voltages were used. From results of the three r values, it was expected that the accuracy of estimation is higher as the difference of the r value is larger. Tanaka and Kawai (2013) also reported that the disparity of two tube voltages affected on the accuracy of dual X-ray absorptiometry for measuring moisture content of wood.

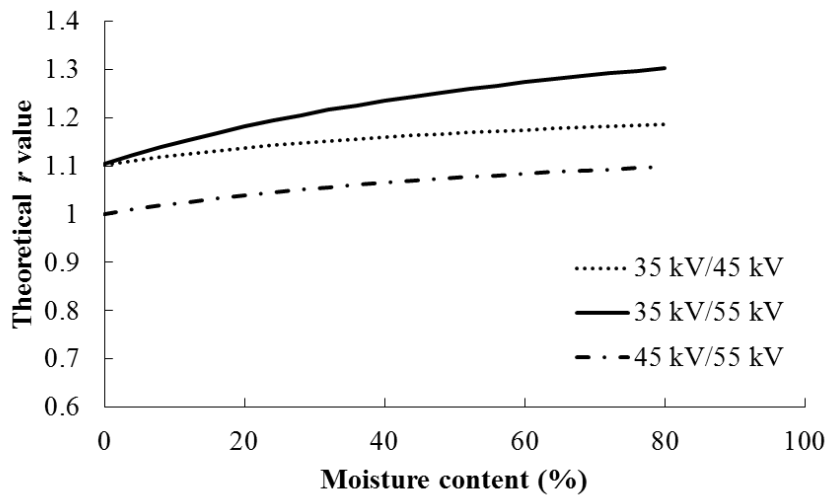
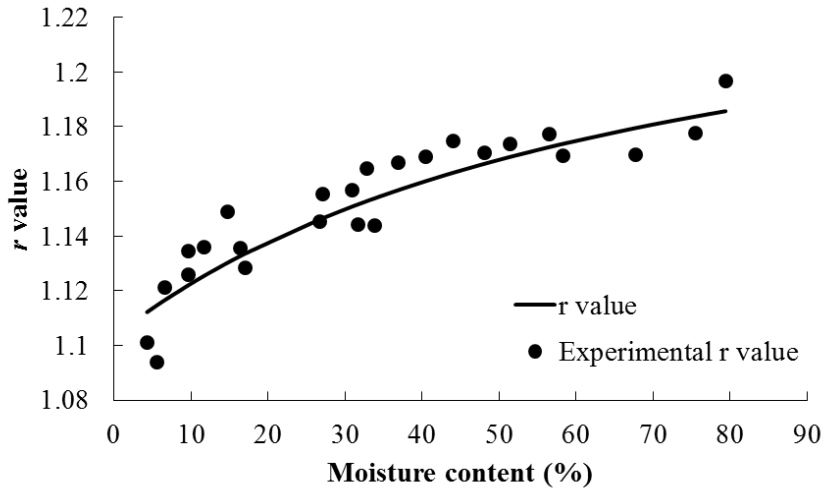


Figure 6-7. Three r values in moisture content

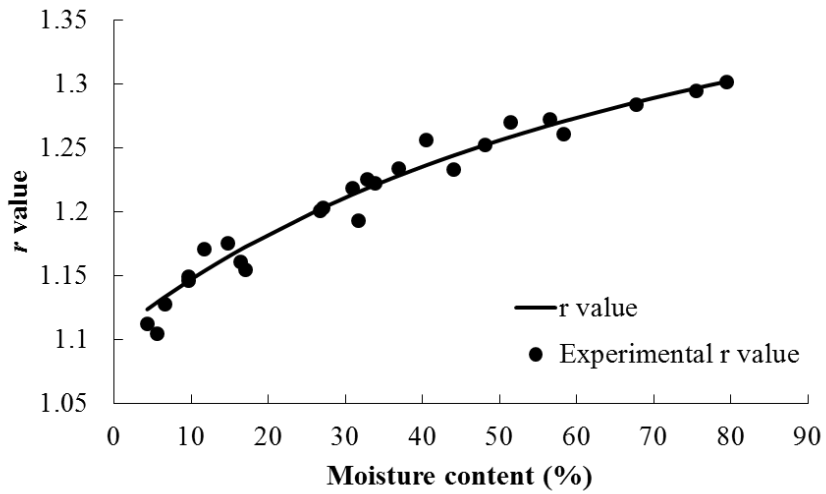
6.4.2. Assessment of moisture content of wood with dual X-ray absorptiometry

The 23 specimens in group 2 were used to validate the accuracy of dual X-ray absorptiometry for predicting moisture content of solid wood. Range of moisture content of those specimens was from 6.20% to 79.40%. From the 69 projections of the specimens, the logarithm ratio of initial X-ray intensity to transmitted X-ray intensity were calculated at 35 kV, 45 kV and 55 kV tube voltages. When the logarithm values were calculated, the integral values of probability function at 35 kV, 45 kV and 55 kV were also considered. The integral values of probability function are shown in Table 3-7. Then, the logarithm value of each tube voltage was used to compute r value as shown in Equation 6-3. As a result, three r values were obtained as 35 kV to 45 kV, 35 kV to 55 kV and 45 kV to 55 kV. The three r values from the 42 specimens in group 2 were referred as experimental r values.

The r values obtained from the apparent mass attenuation coefficient of wood substance and moisture in group 1 at 35 kV, 45 kV and 55 kV tube voltages were compared with the experimental r values to know how they can estimated properly. Figure 6-8 shows the comparison between the r values and the experimental r values. The solid line in Figure 6-8 indicates the r value calculated by using the apparent mass attenuation coefficient of wood substance and moisture while dot was the experimental r values. The experimental r values also increased as moisture content of wood increased like the r values. It was considered that experimental r value could be used to assess moisture content in solid wood.

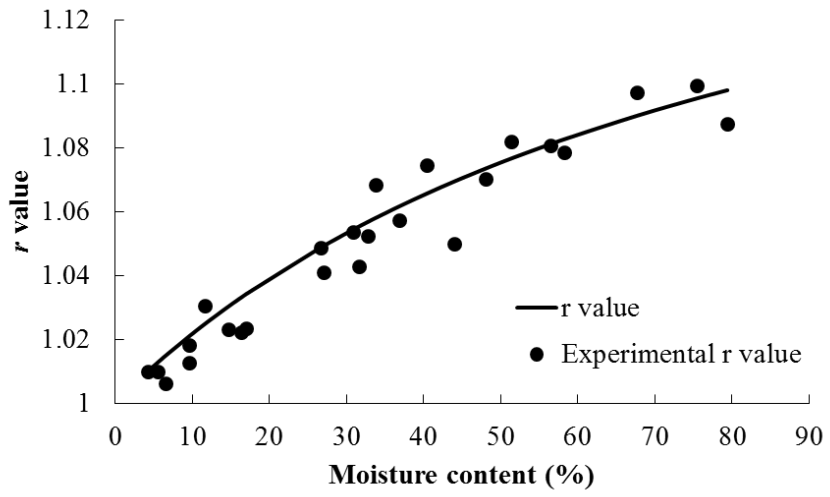


(a) *r* value of 35 kV to 45 kV



(b) *r* value of 35 kV to 55 kV

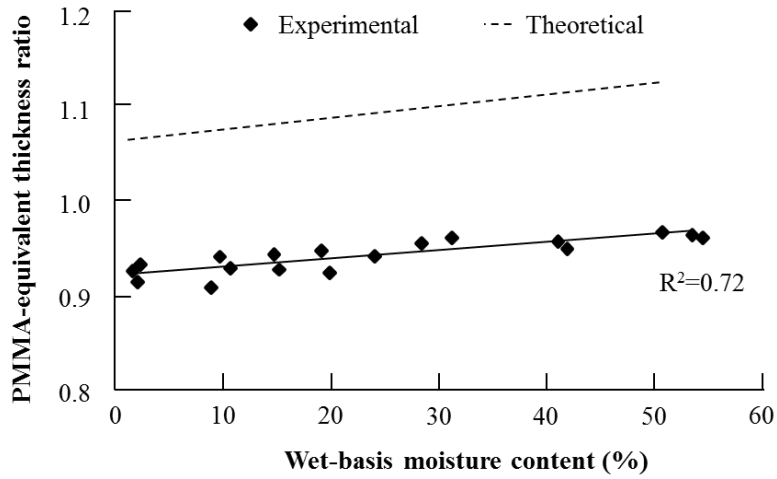
Figure 6-8. *r* value according to moisture content (continue)



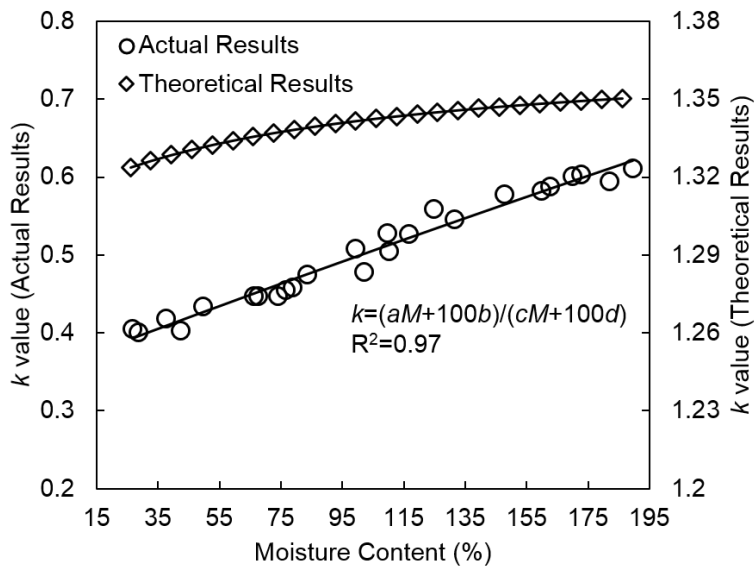
(c) *r* value at 45 kV to 55 kV

Figure 6-8. *r* value according to moisture content

The experimental r values were almost coincided with the r values. It is dissimilar to previous studies about dual X-ray absorptiometry for solid wood (Kim et al., 2015; Tanaka and Kawai, 2013). They reported that the experimentally obtained results with dual X-ray absorptiometry were differed from the theoretically derived results. Figure 6-9 shows those results. In the previous studies, the mass attenuation coefficients of wood according to moisture content were derived by using mass attenuation coefficients of component elements such as carbon, hydrogen, oxygen and so on. Mass attenuation coefficients of the component elements were the referenced values according to monochromatic X-ray energies as same as the effective energies of polychromatic X-ray, because polychromatic X-ray were used in the previous study. So, it was considered that the difference between r values was occurred. Therefore, it is needed to evaluate mass attenuation coefficient of wood experimentally, or to calculate it considering the spectrum of polychromatic X-ray energies and the energy dependent detection efficiency when poly chromatic X-ray were used to determine wood properties.



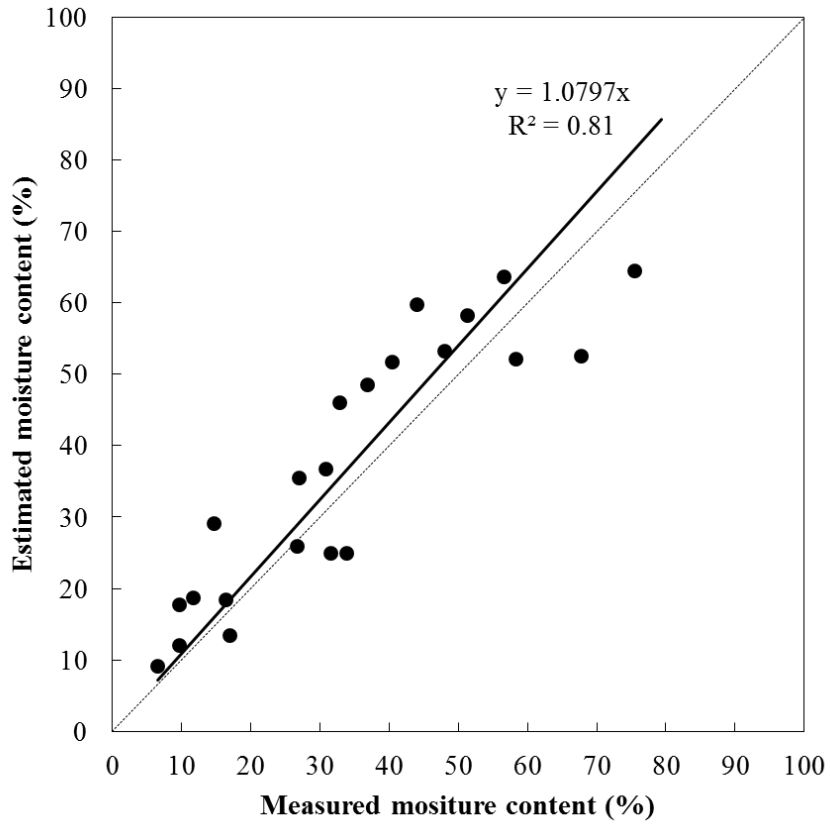
(a) Tanaka and Kawai, 2013



(b) Kim et al., 2015

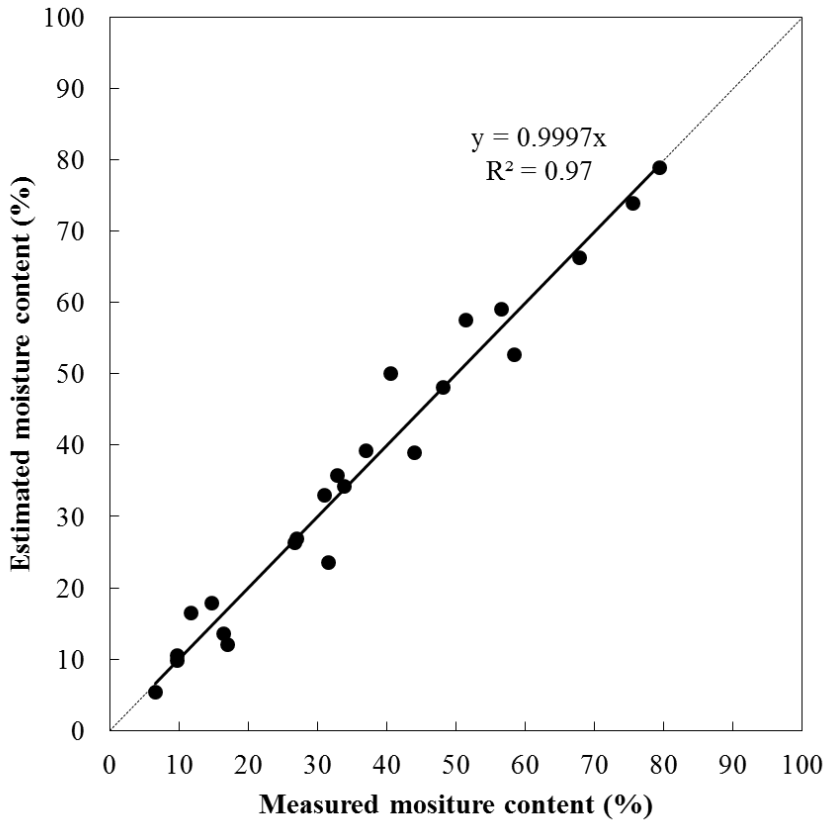
Figure 6-9. Theoretical and experimental result in various moisture content (Kim et al., 2015; Tanaka and Kawai, 2013). Here, PMMA ratio and k values were as same as r values.

Moisture content measured by the oven-dry method of 23 specimens in group 2 was compared with the determined moisture content by using Equation 6-6. In Equation 6-6, experimental r value obtained from the projections of 23 specimens in group 2 at 35 kV to 45 kV, 35 kV to 55 kV and 45 kV to 55 kV were used, while the apparent mass attenuation coefficient of wood substance and moisture calculated from the 42 specimens in group 1 were applied. Figure 6-10 shows comparisons between the measured and the determined moisture content of wood. The range of moisture content of wood was from 6.20% to 79.40%. The coefficients of determination for 35 kV to 45 kV, 35 kV to 55 kV and 45 kV to 55 kV were 0.81, 0.97 and 0.91, respectively. The RMSEs, which was used to measure of the difference between measured and predicted moisture content, at three conditions were respectively 10.42%, 3.91% and 7.13%. Appendix B presents all results of the measured and the determined moisture content for each case. When the 35 kV and 55 kV tube voltages were applied to predict moisture content, the best accuracy of dual X-ray absorptiometry was indicated. It was expected that the accuracy of dual X-ray absorptiometry would be affected by the difference of r value between moisture content of 0% and that of 80%. If the difference of r value was large enough to cover some instrumental errors in dual X-ray absorptiometry, the accuracy of the dual X-ray absorptiometry will be improved. The accuracy of determination of moisture content by using dual X-ray absorptiometry was higher than the result of (Tanaka and Kawai (2013)), and there was no difference between r values. Therefore, the mass attenuation coefficient of wood substance and moisture could be used to determine moisture content by using the method developed in this study. And it was also confirmed that moisture content under fiber saturation point could be determined by using dual X-ray absorptiometry with high accuracy.



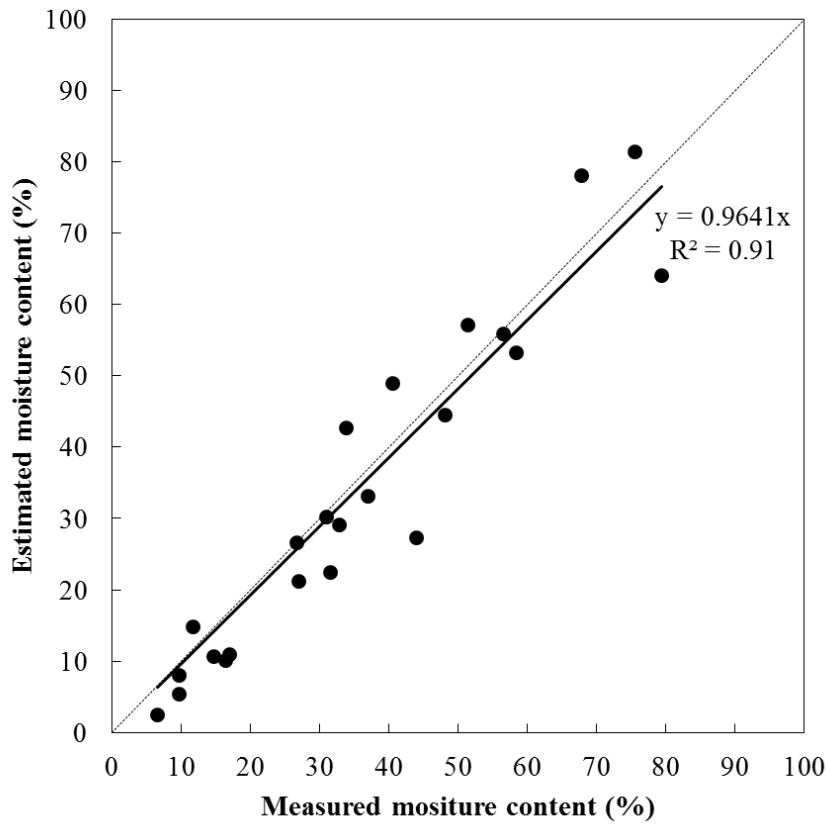
(a) Estimated moisture content by using 35 kV to 45 kV

Figure 6-10. Comparison of moisture content with estimated moisture content (continue)



(b) Estimated moisture content by using 35 kV to 55 kV

Figure 6-10. Comparison of moisture content with estimated moisture content (continue)

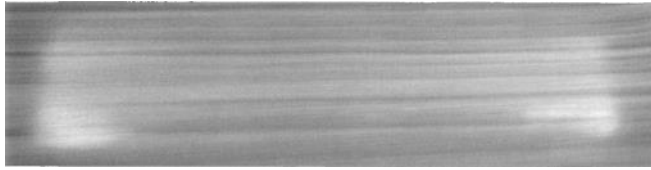


(c) Estimated moisture content by using 35 kV to 55 kV

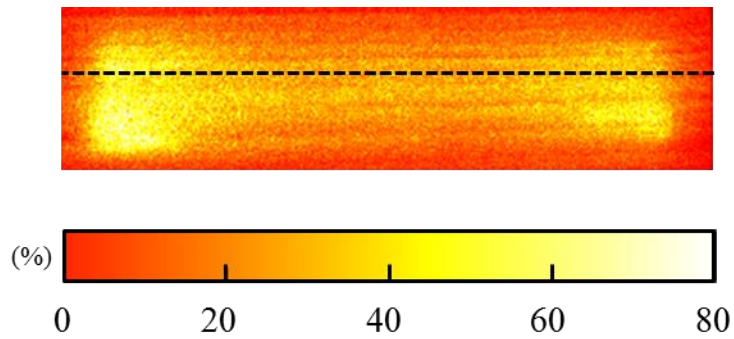
Figure 6-10. Comparison of moisture content with estimated moisture content

A specimen in group 2 was used to confirm whether dual X-ray absorptiometry could examine a distribution of moisture content of wood or not. To choose the specimen, totally clear woods were selected among the specimens in group 2, and then those experimental r values at 35 kV to 55 kV were also checked that the r values were contained within the range of r value according to moisture content. Only pair of tube voltage at 35 kV to 55 kV was used, because the highest accuracy of estimation was shown when dual X-ray absorptiometry was conducted with those pair of tube voltage. Figure 6-11a shows the single projection of the specimen by using tube voltage of 55 kV. In the projection, brighter part was considered as a part having high moisture content. Because it was totally clear wood and was dried by using the oven to make variation of moisture content after being soaked. Its average moisture content was 16.25% when oven-dry method was conducted.

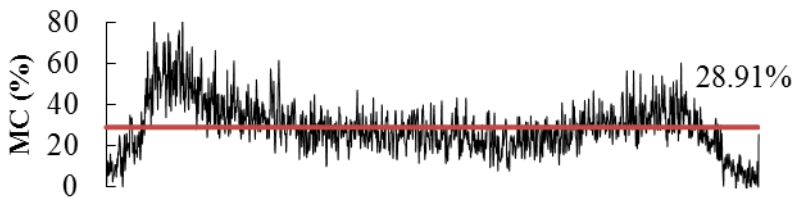
Figure 6-11b shows the distribution of moisture content in the specimen estimated by using dual X-ray absorptiometry at 35 kV to 55 kV. The profile of moisture content along with the dashed line in the distribution of moisture content was also obtained, and the average moisture content within the dashed line was 28.91%. The average moisture content within dashed line was higher than the whole average moisture content in specimen, because undried parts were contained along with the dashed line. It was considered that dual X-ray absorptiometry could examine the distribution of moisture content as well as average moisture content in wood. That information can be used to control drying schedule or to estimate wood properties without oven-dried specimen result. However, the r value should be studied for broad range of moisture content to estimate high moisture content. And other factors such as knot, resin pocket and so on, which could effect on the results of dual X-ray absorptiometry, are needed to be studied.



(a) Single projection



(b) Moisture distribution



(c) Profile of moisture distribution at dashed line shown in Figure 6-11b

Figure 6-11. Projection of specimen and estimated distribution of moisture content

6.5. Conclusion

To find an alternative method to oven-dry method, the dual X-ray absorptiometry was developed. For deriving the equation of dual X-ray absorptiometry, wood was regarded as a mixture of wood substance and moisture. So, the apparent mass attenuation coefficient of wood could be calculated by using the weighted sum of the apparent mass attenuation coefficient of wood substance and moisture. Those apparent mass attenuation coefficients were used to derive the equation of dual X-ray absorptiometry for estimating moisture content of wood. The r value for dual X-ray absorptiometry was induced, and moisture content of from 6.20% to 79.40% in solid wood was measured by analyzing the projections from polychromatic X-ray tube and digital detector with the experimental r value. Unlike previous studies about the dual X-ray absorptiometry of wood, the equation of dual X-ray absorptiometry could be directly employed to evaluate moisture content of wood. The smallest RMSE for evaluating the accuracy of dual X-ray absorptiometry was 3.91%, when tube voltages at 35 kV to 55 kV were used. Not only the average of moisture content of wood but the distribution of moisture content in wood could be obtained by using the dual X-ray absorptiometry. And it was confirmed that moisture content of under fiber saturation point could be determined by using dual X-ray absorptiometry method with high accuracy. To improve the accuracy of dual X-ray absorptiometry, the r value for broad range of moisture content and other factors affected on the dual X-ray absorptiometry are needed to be studied.

Chapter 7

Concluding Remarks

In this study, reconstruction methods using X-ray projection were studied to nondestructively evaluate wood. To improve applicability in field, polychromatic X-ray having low X-ray energy was used to take projections.

The X-ray attenuation characteristic in wood was studied firstly. The apparent mass attenuation coefficient of wood was influenced by penetration depth and X-ray energies. The species did not affect the change of apparent mass attenuation coefficient. From the relationship between the apparent mass attenuation coefficient and penetration depth, projections were converted into density profiles successfully. If polychromatic X-ray were used to quantitatively evaluate wood, the influence of penetration depth should be considered. As penetration depth increased, the attenuation coefficient of wood decreased because of beam hardening. The beam hardening was more serious when lower X-ray energy was used.

The phantom is usually used to quantify CT image, but it is difficult to apply when CT was used in the field. In previous study, it was confirmed that the mass attenuation coefficient was influenced by penetration depth. Based on the results, modified CT reconstructed algorithm was induced with measurement of cross sectional shape of wood. The measurement was conducted by using laser meter, and it can be measure the shape of cross section of wood even though wood had irregular shape. A post processing for CT image was applied to find low density part in wood. The threshold of 70% air-dry density of early wood indicated high accuracy to find low density part in wood.

Tomosynthesis was firstly applied for nondestructive evaluation of wood. It was proposed to improve applicability of X-ray CT. With the optimum condition for obtaining projection, angular range of 60 degrees and 31 projections, wood member could be investigated successfully.

The dual X-ray absorptiometry was developed to estimate moisture content of wood. The method could evaluate average value and distribution of

moisture content in wood without air-dry density information. In this study, wood was regarded as a mixture of wood substance and moisture. From the assumption, the equation of dual X-ray absorptiometry was derived. The accuracy of dual X-ray absorptiometry was influenced by difference of X-ray energies. If the results of dual X-ray absorptiometry were included in the equation of relationship between r value and moisture content, not only average moisture content but also distribution of that could be estimated. That information might be helpful in wood drying science.

From the results, reconstruction method could be applied to evaluate air-dry density and moisture content or to find deterioration. However, there were values evaluated experimentally such as integral value of probability function, apparent mass attenuation coefficient of wood substance and moisture. In further study, it is needed to develop for calculating those values without experiment. The energy distribution of polychromatic X-ray should be studied for that. And nondestructive evaluation system is needed to establish including the research considering the trace and ankertrass of insect. That would be help to analyze the result of reconstructed image.

Appendix

Appendix A

Measured and estimated air-dry density of wood with the equation of apparent mass attenuation coefficient

Species	Penetration depth (mm)	I ₀ /I	Air-dry density (g/cm ³)			
			Measured	Estimated		
				35 kV	45 kV	55 kV
Larch	20.17	105.438	0.598	0.599	0.599	0.592
	20.30	97.369	0.508	0.511	0.503	0.500
	20.16	103.829	0.577	0.583	0.586	0.578
	20.18	103.510	0.575	0.579	0.576	0.572
	20.12	104.319	0.584	0.590	0.587	0.582
	40.26	162.022	0.544	0.542	0.546	0.546
	40.20	163.314	0.548	0.547	0.556	0.549
	40.30	184.587	0.624	0.621	0.629	0.619
	40.50	165.226	0.561	0.550	0.567	0.559
	40.37	175.011	0.592	0.587	0.597	0.586
	40.50	162.940	0.547	0.542	0.551	0.544
	40.36	166.777	0.581	0.558	0.562	0.576
	40.38	171.736	0.580	0.576	0.583	0.578
	40.32	174.105	0.585	0.585	0.588	0.581
	40.40	175.888	0.600	0.590	0.604	0.597
	60.64	281.751	0.614	0.617	0.618	0.614
	60.51	282.265	0.634	0.619	0.628	0.631
	60.64	271.258	0.604	0.599	0.603	0.599
	60.50	281.312	0.627	0.618	0.599	0.620
	60.52	281.033	0.627	0.617	0.635	0.618
	60.46	292.157	0.630	0.636	0.638	0.629
	60.71	270.122	0.592	0.597	0.590	0.594
	60.84	252.517	0.563	0.564	0.560	0.563
	60.70	264.151	0.585	0.586	0.589	0.584
	60.72	260.757	0.585	0.580	0.572	0.588
	80.78	351.231	0.567	0.566	0.577	0.572

	80.80	365.227	0.567	0.582	0.574	0.576
	80.74	371.793	0.569	0.590	0.587	0.581
	80.79	365.242	0.565	0.582	0.570	0.546
	80.65	365.487	0.583	0.583	0.595	0.581
	80.67	373.064	0.582	0.591	0.583	0.584
	80.61	363.690	0.584	0.581	0.600	0.589
	80.78	353.450	0.560	0.568	0.572	0.562
	80.80	357.235	0.560	0.573	0.577	0.560
	80.74	365.744	0.562	0.583	0.561	0.571
	20.02	101.357	0.552	0.562	0.557	0.550
	20.24	97.867	0.512	0.518	0.511	0.508
	20.02	100.658	0.542	0.554	0.549	0.545
	20.07	96.302	0.493	0.506	0.498	0.500
	20.15	97.038	0.508	0.512	0.512	0.506
	40.43	156.792	0.510	0.519	0.523	0.514
	40.51	155.371	0.518	0.513	0.522	0.517
	40.30	162.149	0.537	0.541	0.546	0.538
	39.92	159.641	0.535	0.537	0.543	0.531
	40.05	160.292	0.544	0.538	0.550	0.543
	40.27	157.408	0.524	0.524	0.533	0.524
	40.05	158.199	0.539	0.530	0.550	0.542
Pine	40.10	154.541	0.514	0.514	0.522	0.517
	40.18	154.461	0.521	0.513	0.526	0.519
	40.16	162.626	0.537	0.545	0.549	0.544
	60.43	222.257	0.522	0.506	0.525	0.520
	60.56	235.055	0.528	0.532	0.549	0.525
	60.78	227.022	0.515	0.514	0.530	0.513
	60.56	234.305	0.525	0.530	0.534	0.532
	60.61	230.042	0.508	0.521	0.512	0.517
	60.69	221.302	0.513	0.502	0.524	0.514
	60.18	238.900	0.526	0.543	0.542	0.534
	60.40	235.011	0.513	0.533	0.534	0.511
	60.18	235.891	0.523	0.537	0.543	0.536
	60.23	229.493	0.506	0.523	0.509	0.507

	80.54	341.803	0.524	0.556	0.534	0.535
	80.59	330.065	0.512	0.541	0.532	0.509
	80.67	312.851	0.515	0.519	0.528	0.504
	80.89	331.327	0.521	0.541	0.554	0.528
	80.67	325.226	0.529	0.535	0.535	0.549
	80.72	305.436	0.516	0.509	0.531	0.518
	80.80	306.334	0.520	0.509	0.545	0.511
	80.89	336.035	0.519	0.547	0.546	0.531
	80.94	306.191	0.506	0.508	0.503	0.510
	81.02	306.885	0.510	0.509	0.525	0.515
	19.84	86.111	0.394	0.392	0.383	0.380
	20.12	87.790	0.406	0.406	0.399	0.396
	20.09	88.085	0.402	0.410	0.397	0.394
	20.13	87.643	0.407	0.404	0.394	0.391
	20.23	86.532	0.395	0.388	0.377	0.381
	40.21	127.966	0.398	0.397	0.404	0.395
	40.31	126.918	0.392	0.391	0.398	0.392
	40.27	127.374	0.401	0.393	0.397	0.393
	40.35	129.245	0.405	0.401	0.395	0.403
	39.96	126.487	0.402	0.392	0.401	0.391
	40.24	128.720	0.408	0.400	0.410	0.407
Korean	40.21	129.976	0.406	0.406	0.410	0.407
Pine	40.25	129.782	0.409	0.405	0.405	0.405
	40.35	128.122	0.403	0.396	0.401	0.396
	40.38	127.181	0.395	0.391	0.391	0.393
	60.38	175.882	0.401	0.396	0.410	0.405
	59.99	174.054	0.399	0.393	0.406	0.401
	60.27	177.066	0.403	0.399	0.410	0.409
	60.24	174.470	0.402	0.393	0.409	0.407
	60.28	172.585	0.403	0.387	0.405	0.404
	60.38	174.429	0.399	0.392	0.406	0.401
	60.07	178.066	0.402	0.404	0.412	0.406
	60.35	180.423	0.406	0.408	0.404	0.412
	60.32	177.651	0.405	0.401	0.420	0.412

60.36	177.226	0.406	0.399	0.409	0.407
80.40	244.077	0.401	0.418	0.413	0.410
80.44	229.359	0.402	0.392	0.419	0.415
80.54	239.518	0.399	0.409	0.413	0.414
80.04	231.008	0.400	0.397	0.424	0.404
80.01	239.598	0.399	0.412	0.425	0.415
80.05	233.529	0.400	0.401	0.422	0.400
80.15	233.909	0.397	0.402	0.419	0.412
80.29	243.114	0.402	0.417	0.429	0.424
80.33	233.412	0.403	0.400	0.423	0.419
80.43	238.802	0.400	0.409	0.420	0.417

Appendix B

Measured and determined moisture content of wood with oven-dry method and dual X-ray absorptiometry, respectively

No.	Moisture content (%)			
	Measured	Determined		
		35 kV to 45 kV	35 kV to 55 kV	45 kV to 55 kV
1	6.61	9.14	5.30	2.41
2	9.67	17.67	10.43	5.41
3	9.71	12.03	9.78	8.04
4	11.70	18.69	16.48	14.80
5	14.71	29.06	17.82	10.62
6	16.45	18.44	13.61	10.12
7	17.00	13.47	12.00	10.85
8	26.69	25.88	26.25	26.54
9	27.05	35.53	26.94	21.22
10	30.93	36.69	32.94	30.26
11	31.63	24.96	23.54	22.47
12	32.83	46.09	35.79	29.14
13	33.86	24.86	34.26	42.73
14	36.94	48.47	39.23	33.18
15	40.49	51.74	50.11	48.93
16	44.01	59.71	38.96	27.27
17	48.09	53.30	48.11	44.55
18	51.38	58.28	57.57	57.07
19	56.58	63.66	59.06	55.90
20	58.36	52.10	52.72	53.18
21	67.78	52.60	66.22	78.10
22	75.50	64.54	73.90	81.44
23	79.40	106.27	78.89	64.07

References

- Alkan, S., Zhang, Y., and Lam, F., 2007, Moisture distribution changes and wetwood behavior in subalpine fir wood during drying using high X-ray energy industrial CT scanner: *Drying technology*, v. 25, no. 3, p. 483-488.
- Andersson, I., Ikeda, D. M., Zackrisson, S., Ruschin, M., Svahn, T., Timberg, P., and Tingberg, A., 2008, Breast tomosynthesis and digital mammography: a comparison of breast cancer visibility and BIRADS classification in a population of cancers with subtle mammographic findings: *European radiology*, v. 18, no. 12, p. 2817-2825.
- ASTM, 2012, Standard Practice for Radiographic Examination, Volume ASTM E1742/E1742M: Philadelphia, American Society for Testing and Materials.
- Badea, C., 2000, Volume imaging using a combined cone beam CT-DTS approach.
- Badea, C., Kolitsi, Z., and Pallikarakis, N., A 3D imaging system for dental imaging based on digital tomosynthesis and cone beam CT, *in* Proceedings of conference of the International Federation for Medical and Biological Engineering 2001, Volume 2, Citeseer, p. 739-741.
- Bergsten, U., Lindeberg, J., Rindby, A., and Evans, R., 2001, Batch measurements of wood density on intact or prepared drill cores using x-ray microdensitometry: *Wood Science and Technology*, v. 35, no. 5, p. 435-452.

- Bhandarkar, S. M., Luo, X., Daniels, R., and Tollner, E. W., 2006, A novel feature-based tracking approach to the detection, localization, and 3-D reconstruction of internal defects in hardwood logs using computer tomography: *Pattern analysis and applications*, v. 9, no. 2-3, p. 155-175.
- Blanchette, R. A., A guide to wood deterioration caused by microorganisms and insects, *in* *Proceedings The structural conservation of panel paintings: proceedings of a symposium at the J. Paul Getty Museum, 24-28 April 1995* 1998, Getty Conservation Institute, p. 55-68.
- Bonse, U., and Busch, F., 1996, X-ray computed microtomography (μ CT) using synchrotron radiation (SR): *Progress in biophysics and molecular biology*, v. 65, no. 1, p. 133-169.
- Boris, P., Bundgaard, F., and Olsen, A., 1987, The CT (Hounsfield unit) number of brain tissue in healthy infants: *Child's Nervous System*, v. 3, no. 3, p. 175-177.
- Brooks, R. A., and Di Chiro, G., 1976, Beam hardening in x-ray reconstructive tomography: *Physics in medicine and biology*, v. 21, no. 3, p. 390.
- Bucur, V., 2013, *Nondestructive characterization and imaging of wood*, Springer Science & Business Media.
- Burghardt, A. J., Kazakia, G. J., Laib, A., and Majumdar, S., 2008, Quantitative assessment of bone tissue mineralization with polychromatic micro-computed tomography: *Calcified tissue*

international, v. 83, no. 2, p. 129-138.

Chawla, A. S., Lo, J. Y., Baker, J. A., and Samei, E., 2009, Optimized image acquisition for breast tomosynthesis in projection and reconstruction space: *Medical physics*, v. 36, no. 11, p. 4859-4869.

Ciatto, S., Houssami, N., Bernardi, D., Caumo, F., Pellegrini, M., Brunelli, S., Tuttobene, P., Bricolo, P., Fantò, C., and Valentini, M., 2013, Integration of 3D digital mammography with tomosynthesis for population breast-cancer screening (STORM): a prospective comparison study: *The lancet oncology*, v. 14, no. 7, p. 583-589.

Cown, D. J., and Clement, B., 1983, A wood densitometer using direct scanning with X-rays: *Wood Science and Technology*, v. 17, no. 2, p. 91-99.

Divos, F., and Divos, P., Resolution of stress wave based acoustic tomography, *in Proceedings 14th International Symposium on Nondestructive Testing of Wood*, Hannover, Germany, 2005, p. 309-314.

Dobbins III, J. T., and Godfrey, D. J., 2003, Digital x-ray tomosynthesis: current state of the art and clinical potential: *Physics in medicine and biology*, v. 48, no. 19, p. R65.

Engelhardt, M., Kottler, C., Bunk, O., David, C., Schroer, C., Baumann, J., Schuster, M., and Pfeiffer, F., 2008, The fractional Talbot effect in differential x-ray phase-contrast imaging for extended and polychromatic x-ray sources: *Journal of microscopy*, v. 232, no. 1, p. 145-157.

- Espinoza, G. R., Hernández, R., Condal, A., Verret, D., and Beauregard, R., 2005, Exploration of the physical properties of internal characteristics of sugar maple logs and relationships with CT images: *Wood and Fiber Science*, v. 37, no. 4, p. 591-604.
- Feldkamp, L., Davis, L., and Kress, J., 1984, Practical cone-beam algorithm: *JOSA A*, v. 1, no. 6, p. 612-619.
- Fredriksson, M., 2015, Optimizing sawing of boards for furniture production using CT log scanning: *Journal of Wood Science*, v. 61, no. 5, p. 474-480.
- Funt, B. V., and Bryant, E. C., 1987, Detection of internal log defects by automatic interpretation of computer tomography images: *Forest Products Journal*, v. 37, no. 1, p. 56-62.
- Gunderman, R. B., 2006, *Essential radiology. Clinical presentation, pathophysiology, imaging.*, Germany, Thieme.
- Hendrick, R. E., 2007, *Breast MRI: fundamentals and technical aspects*, Springer Science & Business Media.
- Hoag, M., and Krahmer, R., 1991, Polychromatic X-ray attenuation characteristics and wood densitometry applications: *Wood and fiber science*, v. 23, no. 1, p. 23-31.
- Hoaglin, D. C., Mosteller, F., and Tukey, J. W., 2011, *Exploring data tables, trends, and shapes*, John Wiley & Sons.

- Houllier, F., Leban, J.-M., and Colin, F., 1995, Linking growth modelling to timber quality assessment for Norway spruce: *Forest Ecology and Management*, v. 74, no. 1, p. 91-102.
- Hu, Y.-H., Zhao, B., and Zhao, W., 2008, Image artifacts in digital breast tomosynthesis: Investigation of the effects of system geometry and reconstruction parameters using a linear system approach: *Medical physics*, v. 35, no. 12, p. 5242-5252.
- Hultnäs, M., and Fernandez-Cano, V., 2012, Determination of the moisture content in wood chips of Scots pine and Norway spruce using Mantex Desktop Scanner based on dual energy X-ray absorptiometry: *Journal of wood science*, v. 58, no. 4, p. 309-314.
- Jackson, D. F., and Hawkes, D. J., 1981, X-ray attenuation coefficients of elements and mixtures: *Physics Reports*, v. 70, no. 3, p. 169-233.
- Jensen, P. D., Hartmann, H., Böhm, T., Temmerman, M., Rabier, F., and Morsing, M., 2006, Moisture content determination in solid biofuels by dielectric and NIR reflection methods: *Biomass and bioenergy*, v. 30, no. 11, p. 935-943.
- Judy, P., Balter, S., Bassano, D., McCullough, E. C., Payne, J. T., and Rothenberg, I., 1977, Phantoms for performance evaluation and quality assurance of CT scanners, American Association of Physicists in Medicine Diagnostic Radiology Committee
- Kaelble, E. F., 1967, *Handbook of X-rays*, New York, McGraw-Hill Book

Company.

Kak, A. C., and Slaney, M., 1988, Principles of computerized tomographic imaging, IEEE press.

Kershaw, J. A., Benjamin, J. G., and Weiskittel, A. R., 2009, Approaches for modeling vertical distribution of maximum knot size in black spruce: a comparison of fixed-and mixed-effects nonlinear models: Forest Science, v. 55, no. 3, p. 230-237.

Kim, C.-K., Lee, J.-J., and Oh, J.-K., 2013, X-ray Computed Tomography on Larger Diameter Timber than Digital Detector: J. Korean Wood Sci. & Tech, v. 41, no. 5, p. 385-391.

Kim, C.-K., Oh, J.-K., Hong, J.-P., and Lee, J.-J., 2014, Density calculation of wood by portable X-ray tube with consideration of penetrating depth: Journal of wood science, v. 60, no. 2, p. 105-110.

-, 2015, Dual-energy X-ray absorptiometry with digital radiograph for evaluating moisture content of green wood: Wood Science and Technology, v. 49, no. 4, p. 713-723.

Kim, I., Yi, Y., Song, J., Kim, S., and Park, W., 2012, Conservation of Wooden Objects, Korea, National Research Institute of Cultural Heritage.

Kotwaliwale, N., Weckler, P. R., and Bruswitz, G. H., 2006, X-ray attenuation coefficients using polychromatic X-ray imaging of pecan components: Biosystems engineering, v. 94, no. 2, p. 199-206.

- Krumm, M., Kasperl, S., and Franz, M., 2008, Reducing non-linear artifacts of multi-material objects in industrial 3D computed tomography: *Ndt & E International*, v. 41, no. 4, p. 242-251.
- Laufenberg, T. L., 1986, Using gamma radiation to measure density gradients in reconstituted wood products: *Forest Prod. J*, v. 36, no. 2, p. 59-62.
- Lifton, J. J., Malcolm, A. A., and McBride, J. W., The application of beam hardening correction for industrial x-ray computed tomography, *in Proceedings Proc. 5th Int. Symp. NDT in Aerospace2013*.
- Lindgren, L., 1991, Medical CAT-scanning: X-ray absorption coefficients, CT-numbers and their relation to wood density: *Wood Science and Technology*, v. 25, no. 5, p. 341-349.
- Lindgren, O., Davis, J., Wells, P., and Shadbolt, P., 1992, Non-destructive wood density distribution measurements using computed tomography: *Holz als Roh-und Werkstoff*, v. 50, no. 7-8, p. 295-299.
- Liu, C., Olson, J., Tian, Y., and Shen, Q., 1988, Theoretical Wood Densitometry: I Mass Attenuation Equations and Wood Density Models: *Wood and Fiber Science*, v. 20, no. 1, p. 22-34.
- Longuetaud, F., Leban, J.-M., Mothe, F., Kerrien, E., and Berger, M.-O., 2004, Automatic detection of pith on CT images of spruce logs: *Computers and Electronics in Agriculture*, v. 44, no. 2, p. 107-119.
- Longuetaud, F., Mothe, F., Kerautret, B., Krähenbühl, A., Hory, L., Leban, J. M., and Debled-Rennesson, I., 2012, Automatic knot detection and

measurements from X-ray CT images of wood: a review and validation of an improved algorithm on softwood samples: *Computers and Electronics in Agriculture*, v. 85, p. 77-89.

Lu, Y., Chan, H.-P., Wei, J., Goodsitt, M., Carson, P. L., Hadjiiski, L., Schmitz, A., Eberhard, J. W., and Claus, B. E., 2011, Image quality of microcalcifications in digital breast tomosynthesis: effects of projection-view distributions: *Medical physics*, v. 38, no. 10, p. 5703-5712.

Luu, M. B., Arhatari, B. D., Tran, C. Q., Balaur, E., Pham, B. T., Vo, N. T., Chen, B., Putkunz, C. T., Kirby, N., Mudie, S., and Peele, A. G., 2011, Quantitative phase imaging with polychromatic x-ray sources: *Optics Express*, v. 19, no. 9, p. 8127-8134.

Macedo, A., Vaz, C., Pereira, J., Naime, J., Cruvinel, P., and Crestana, S., 2002, Wood density determination by X-and gamma-ray tomography: *Holzforschung*, v. 56, no. 5, p. 535-540.

Malan, F., and Marais, P., 1992, Some notes on the direct gamma ray densitometry of wood: *Holzforschung-International Journal of the Biology, Chemistry, Physics and Technology of Wood*, v. 46, no. 2, p. 91-97.

Nik, S., Meyer, J., and Watts, R., 2011, Optimal material discrimination using spectral x-ray imaging: *Physics in medicine and biology*, v. 56, no. 18, p. 5969.

Niklason, L. T., Christian, B. T., Niklason, L. E., Kopans, D. B., Castleberry,

- D. E., Opsahl-Ong, B., Landberg, C. E., Slanetz, P. J., Giardino, A. A., and Moore, R., 1997, Digital tomosynthesis in breast imaging: *Radiology*, v. 205, no. 2, p. 399-406.
- Nishihata, T., Ohtake, Y., Suzuki, H., and Moriguchi, M., A Non-Iterative Data-Driven Beam Hardening Correction for Single-Material Objects, *in Proceedings Proc. Conf. Industrial Computed Tomography2012*, p. 135-142.
- Oh, J.-K., Kim, C.-K., Hong, J.-P., and Lee, J.-J., 2015, Improvement of robustness in ultrasonic attenuation spectroscopy for detecting internal insect damage in wood member of cultural heritage: *Journal of Wood Science*, v. 61, no. 2, p. 136-142.
- Oh, J., Cho, H., Kim, D., Choi, S., and Je, U., 2012, Application of digital tomosynthesis (DTS) of optimal deblurring filters for dental X-ray imaging: *Journal of the Korean Physical Society*, v. 60, no. 7, p. 1161-1166.
- Oja, J., 2000, Evaluation of knot parameters measured automatically in CT-images of Norway spruce (*Picea abies* (L.) Karst.): *European Journal of Wood and Wood Products*, v. 58, no. 5, p. 375-379.
- Oja, J., and Temnerud, E., 1999, The appearance of resin pockets in CT-images of Norway spruce (*Picea abies* (L.) Karst.): *Holz als Roh-und Werkstoff*, v. 57, no. 5, p. 400-406.
- Olson, J., Liu, C., Tian, Y., and Shen, Q., 1988a, Theoretical wood densitometry. II. Optimal x-ray energy for wood density measurement:

Wood and fiber science: journal of the Society of Wood Science and Technology (USA).

Olson, J. R., Liu, C., Tian, Y., and Shen, Q., 1988b, Theoretical Wood Densitometry: II. Optimal X-ray Energy For Wood Density Measurement: *Wood and Fiber Science*, v. 20, no. 2, p. 187-196.

Pang, G., Bani-Hashemi, A., Au, P., O'Brien, P., Rowlands, J., Morton, G., Lim, T., Cheung, P., and Loblaw, A., 2008, Megavoltage cone beam digital tomosynthesis (MV-CBDT) for image-guided radiotherapy: a clinical investigational system: *Physics in medicine and biology*, v. 53, no. 4, p. 999.

Park, Y., Eom, C.-D., Han, Y., Park, J.-H., Chang, Y.-S., Yang, S.-Y., Choi, J.-W., and Yeo, H., 2014, Combined treatment of green pitch pine wood by heat and superheated steam and the effects on physical properties of the products: *Holzforschung*, v. 68, no. 3, p. 327-335.

Pease, B. J., Scheffler, G. A., and Janssen, H., 2012, Monitoring moisture movements in building materials using X-ray attenuation: Influence of beam-hardening of polychromatic X-ray photon beams: *Construction and Building Materials*, v. 36, p. 419-429.

Phillips, E., 1960, The beta ray method of determining the density of wood and the proportion of summer wood: *Journal of the Institute of Wood Science*, no. 5, p. 16-28.

Poludniowski, G., Landry, G., DeBlois, F., Evans, P., and Verhaegen, F., 2009, SpekCalc: a program to calculate photon spectra from tungsten anode

x-ray tubes: Physics in medicine and biology, v. 54, no. 19, p. N433.

Rasband, W. S., 2008, ImageJ: <https://imagej.nih.gov/ij/>.

Rojas, G., Beauregard, R., Hernández, R. E., Verret, D., and Condal, A., 2007, Effect of moisture content variation on CT image classification to identify internal defects of sugar maple logs: Forest products journal, v. 57, no. 4, p. 38.

Rosenfeld, A., and Kak, A. C., 2014, Digital picture processing, Elsevier.

Schlomka, J., Roessl, E., Dorscheid, R., Dill, S., Martens, G., Istel, T., Bäumer, C., Herrmann, C., Steadman, R., and Zeitler, G., 2008, Experimental feasibility of multi-energy photon-counting K-edge imaging in pre-clinical computed tomography: Physics in medicine and biology, v. 53, no. 15, p. 4031.

Sechopoulos, I., 2013, A review of breast tomosynthesis. Part I. The image acquisition process: Medical physics, v. 40, no. 1, p. 014301.

Sechopoulos, I., and Ghetti, C., 2009, Optimization of the acquisition geometry in digital tomosynthesis of the breast: Medical physics, v. 36, no. 4, p. 1199-1207.

Sepúlveda, P., Oja, J., and Grönlund, A., 2002, Predicting spiral grain by computed tomography of Norway spruce: Journal of wood science, v. 48, no. 6, p. 479-483.

Sidky, E. Y., Yu, L., Pan, X., Zou, Y., and Vannier, M., 2005, A robust method

of x-ray source spectrum estimation from transmission measurements:
Demonstrated on computer simulated, scatter-free transmission data:
Journal of applied physics, v. 97, no. 12, p. 124701.

Solbrig, K., Frühwald, K., Ressel, J. B., and Fuchs, M., Wood-based composite X-ray densitometry - attenuation effects on measurements, *in* Proceedings 19th International Nondestructive Testing and Evaluation of Wood Symposium, Rio de Janeiro, Brazil, 2015, p. 303-313.

Taguchi, K., Frey, E. C., Wang, X., Iwaczyk, J. S., and Barber, W. C., 2010, An analytical model of the effects of pulse pileup on the energy spectrum recorded by energy resolved photon counting x-ray detectors: Medical physics, v. 37, no. 8, p. 3957-3969.

Tanaka, T., Avramidis, S., and Shida, S., 2009, Evaluation of moisture content distribution in wood by soft X-ray imaging: Journal of wood science, v. 55, no. 1, p. 69-73.

Tanaka, T., and Kawai, Y., 2013, A new method for nondestructive evaluation of solid wood moisture content based on dual-energy X-ray absorptiometry: Wood science and technology, v. 47, no. 6, p. 1213-1229.

Tiitta, M., Olkkonen, H., Lappalainen, T., and Kanko, T., 1993, Automated low energy photon absorption equipment for measuring internal moisture and density distributions of wood samples: Holz als Roh- und Werkstoff, v. 51, no. 6, p. 417-421.

- Tucker, D. M., Barnes, G. T., and Chakraborty, D. P., 1991, Semiempirical model for generating tungsten target x-ray spectra: *Medical physics*, v. 18, no. 2, p. 211-218.
- Tuy, H. K., 1993, A post-processing algorithm to reduce metallic clip artifacts in CT images: *European Radiology*, v. 3, no. 2, p. 129-134.
- Waggener, R. G., Levy, L. B., Rogers, L. F., and Zanca, P., 1972, Measured X-Ray Spectra from 25 to 110 kVp for a Typical Diagnostic Unit 1: *Radiology*, v. 105, no. 1, p. 169-175.
- Watanabe, K., Lazarescu, C., Shida, S., and Avramidis, S., 2012, A novel method of measuring moisture content distribution in timber during drying using CT scanning and image processing techniques: *Drying Technology*, v. 30, no. 3, p. 256-262.
- Watanabe, K., Saito, Y., Avramidis, S., and Shida, S., 2008, Non-destructive measurement of moisture distribution in wood during drying using digital X-ray microscopy: *Drying technology*, v. 26, no. 5, p. 590-595.
- Wei, Q., Chui, Y. H., Leblon, B., and Zhang, S. Y., 2009, Identification of selected internal wood characteristics in computed tomography images of black spruce: a comparison study: *Journal of wood science*, v. 55, no. 3, p. 175-180.
- Woods, F. W., and Lawhon, W. T., 1974, Notes: Gamma Densitometry of Increment Cores: *Forest Science*, v. 20, no. 3, p. 269-271.
- Wu, T., Moore, R. H., Rafferty, E. A., and Kopans, D. B., 2004, A comparison

of reconstruction algorithms for breast tomosynthesis: Medical physics, v. 31, no. 9, p. 2636-2647.

Zhang, Y., Chan, H.-P., Sahiner, B., Wei, J., Goodsitt, M. M., Hadjiiski, L. M., Ge, J., and Zhou, C., 2006, A comparative study of limited-angle cone-beam reconstruction methods for breast tomosynthesis: Medical physics, v. 33, no. 10, p. 3781-3795.

Zhao, C., Kanicki, J., Konstantinidis, A. C., and Patel, T., 2015, Large area CMOS active pixel sensor x-ray imager for digital breast tomosynthesis: Analysis, modeling, and characterization: Medical physics, v. 42, no. 11, p. 6294-6308.

Zou, W., Hunter, N., and Swain, M., 2011, Application of polychromatic μ CT for mineral density determination: Journal of dental research, v. 90, no. 1, p. 18-30.

김광모, 이상준, and 이천제, 2006a, 현장 적용이 가능한 X 선 CT 시스템 개발 1-X 선 촬영법을 이용한 목재의 밀도 측정: 목재공학, v. 34, no. 1, p. 15-22.

-, 2006b, 현장 적용이 가능한 X 선 CT 시스템 개발 2-밀도분포를 이용한 목재의 CT 영상 구성: 목재공학, v. 34, no. 1, p. 23-31.

이천제, 김규혁, 엄영근, and 오정권, 2005, 비파괴 검사법에 의한 국산재의 생물학적 열화 평가기술 개발.

Abstract (Korean)

초 록

본 논문에서는 휴대용 X선 선원에서 발생하는 X선과 디텍터를 통해 얻어진 X선 이미지를 이용하여, 목재의 내부 상태를 평가하는 방법에 대한 연구를 진행하였다. 연구를 진행함에 있어, X선 선원에서 발생하는 넓은 파장을 가지는 X선이 목재를 투과하면서 감쇠되는 특성을 구명하였으며, 이를 통해 재구성된 단일 X선 이미지와 컴퓨터단층촬영 이미지를 이용하여 목재의 기건 밀도를 평가하였다. 한편 최적 촬영 조건을 이용한 단층영상합성법을 제안하여 컴퓨터단층촬영을 적용할 수 없는 곳에 위치한 목재의 내부 상태와 이중에너지 방사선 흡수법을 통하여 전건 밀도에 대한 정보 없이 목재 내 함수율을 평가하였다.

넓은 파장을 가지는 X선의 목재를 투과할 때 감쇠되는 특성을 평가하기 위하여 목재의 질량감쇠계수를 도출하였다. 기존 목재의 질량감쇠계수에 대한 연구와 달리, 목재 내 X선 투과 거리가 길어질수록 목재의 질량감쇠계수가 작아졌다. 이는 넓은 파장을 가지는 X선 내에서 파장의 길이가 긴 X선이 먼저 감쇠되어 나타나는 빔 경화 현상에 의한 것으로 사료되었다. 이에 X선 선원에서 발생하는 X선이 목재를 투과할 때 감쇠되는 정도를 정량화하기 위하여, X선 투과거리에 따른 목재의 질량감쇠계수의 변화에 대한 회귀식을 도출하였다. 도출된 회귀식을 이용하여 재구성된 X선 영상으로 목재의 기건 밀도를 높은 정확도를 평가하였으며, 평균 제곱근 편차는 X선 선원의 관전압이 35 kV일 때 0.0103 g/cm^3 이었다. 이를 통하여, 목재 내 X선 감쇠 특성을 이용하여 높은 정확도로 목재의 기건 밀도를 평가할 수 있음을 확인할 수 있었다.

다양한 방향에서 얻어진 X선 이미지를 이용하면 컴퓨터단층촬영 이미지를 재구성할 수 있다. 일반적으로 재구성된 이미지의 정량적 평가를 위하여, 기준 물질인 팬텀을 사용하나 조사 대상이 있는 현장에서는 적용이 어렵다. 이에 앞서 제안된 단일 X선 이미지를 정량화하는 방법을

이용하여, 밀도 컴퓨터단층촬영 이미지를 재구성할 수 있는 방법이 제안되었다. 레이저 변위 측정기로 시편의 단면 형상을 측정하여 실제 X선이 투과된 거리를 계산하였으며, 계산된 투과 거리와 목재의 질량감쇠계수의 관계를 이용하여 X선 이미지를 정량화 한 후 재구성하여 정량화된 밀도 단층 이미지를 획득하였다. 제안된 방법을 이용하여 목재의 단면 내 기진 밀도를 평가하기 위해서는 적어도 180 개의 방사선 사진이 필요하였다. 또한 열화된 부재를 제안된 방법을 이용하여 조사하였을 때, 직경 2 mm 이하의 작은 충해도 탐지할 수 있었다.

컴퓨터단층촬영법은 적어도 180도 이상 회전하면서 얻어진 X선 이미지를 필요로 하기 때문에, 벽이 있는 목조 건축물의 기둥 부재와 같이 장비의 회전이 제약이 있는 경우에 목재 내부 상태를 조사하기 어렵다. 이를 극복하고자 단층영상합성법에 대한 연구를 진행하였다. 목재의 내부 상태를 조사하기 위한 최적의 촬영 조건을 찾기 위하여 contrast-to-noise ratio (CNR)와 artifact spread function (ASF)를 이용하여 단층영상합성법으로 재구성된 X선 이미지를 평가하였다. 재구성된 X선 이미지의 영상 정확도는 X선 선원과 디텍터의 회전 각도가 클수록 높아졌으나, 재구성을 위해 사용된 X선 이미지 수는 그 수가 많아질수록 영상 정확도가 높아지다 일정 수 이상에서는 정확도의 차이가 크지 않았다. 단층영상합성법에 의해 재구성된 영상의 수직 해상도는 방사선 사진 수에 의해 크게 영향을 받지 않았으며, 회전 각도가 클수록 향상되었다. 본 연구 조건 하에서, 최적의 촬영 조건은 60도의 X선 선원과 디텍터 회전 각도와 31개의 방사선 사진 수 이었다.

하나의 X선 에너지를 이용하여 목재 내 함수율을 평가하는 기존의 방법은 평가하고자 하는 목재의 전건 밀도 정보를 필요로 하기 때문에 그 사용이 제한적이다. 이에 X선 에너지에 따른 목재의 질량감쇠계수 차이를 이용하여 목재의 전건 밀도 정보 없이 목재 내 함수율을 평가할 수 있는 이중에너지 방사선 흡수법에 대한 연구를 진행하였다. 본 연구에서는 목재는 전건 목질부와 밀로 이루어져있다고 가정하여, 함수율을 측정할 수

있는 이중에너지 방사선 흡수법 식을 제안하였다. 두 개의 X선 에너지 차가 클 때, 목재 내 함수율 측정정확도가 높았으며, 이 때 평균 제곱근 편차는 3.91%로 나타났다. X선이 목재 내에서 감쇠되는 특성을 고려함으로써, 이전 연구결과와 달리 이중에너지 방사선 흡수법을 이용하여 섬유포화점 아래에서도 측정 정확도가 높았으며, 목재 내 평균 함수율 분포 또한 획득할 수 있었다.

주요어: Polychromatic X선; 목재; 질량감쇠계수; 컴퓨터단층영상촬영 이미지; 단층영상합성법; 이중에너지 방사선 흡수법

학 번: 2008-23057